MEASUREMENT OF THE RADIATIVE DECAY WIDTH OF THE RHO MESON

by

Terrence C. Jensen

Submitted in Partial Fulfillment

of the

Requirements for the Degree

DOCTOR OF PHILOSOPHY

Department of Physics and Astronomy

The University of Rochester

Rochester, New York.

1980

FERMILAB
LIBRARY

VITAE

The author was born March 23, 1952 in Ringsted, Iowa. He commenced undergraduate studies at Iowa State University in September 1970. In May 1974 the author graduated with distinction from Iowa State University with Bachelor of Science Degrees in Mathematics and Physics. He was awarded a Rush Rhees Fellowship upon entering the University of Rochester in September 1974. During graduate studies at the University of Rochester, the author has received additional support from a teaching assistantship and from research assistantships. The work presented in this thesis was carried out under the supervision of Professors Thomas Ferbel and Paul Slattery.

ACKNOWLEDGMENTS

The execution of the experiment described in this thesis has been a combined effort of many individuals from several institutions. The principal collaborators on this experiment were: Joe Biel, Tom Droege, Alan Jonckheere and Peter Koehler, from Fermilab, Steve Heppelmann, Terry Joyce, Yousef Makdisi, Marvin Marshak, Earl Peterson, Keith Ruddick and Tom Walsh from the University of Minnesota, David Berg, Clark Chandlee, Selcuk Cihangir, Tom Ferbel, Fred Lobkowicz, Charles Nelson, Takayoshi Ohshima, Paul Slattery and Pat Thompson from the University of Rochester. This research was supported in part by the Department of Energy and the National Science Foundation.

I wish to thank all of the people at Fermilab who have worked hard to provide and maintain the equipment needed to perform this experiment. I am grateful to Kevin Einsweiler, Tom Chyba, Bruce Campbell, and to Tom Haelen and the staff at the University of Rochester Cyclotron Lab for their help in constructing the drift chambers. I thank Richard Burke for building the target box, and Jackie Gallet and Paul Ganci for assisting during data taking. With great zeal, Mike McLaughlin undertook the task of visually analyzing a

sample of kaon decays, and Joe Huston performed fits to the data.

I extend a special thank you to Dr. Takayoshi Ohshima for the incessant concerned attention he has given to all aspects of this experiment.

It has been a great pleasure to work closely with Professors Tom Ferbel and Paul Slattery throughout my graduate career.

My stay at Fermilab has been made more pleasant by my friendship with Joe Biel.

I thank Mrs. Betty Cook for her advice and guidance on administrative matters during my studies at the University of Rochester.

Mr. John Sheedy has done an excellent job of inking the figures for this thesis.

I am most grateful to Mrs Edna Hughes and Mrs. Shirley Brignall for typing portions of this thesis.

Finally I express my sincere thanks to my parents, Nina and Harald Jensen, for their constant support and encouragement throughout my studies.

ABSTRACT

We have investigated the coherent reaction $\pi^- A \rightarrow A\pi^-\pi^0$ using nuclear targets of C, Al, Cu and Pb, at beam momenta of 156 GeV/c and 260 GeV/c. We found that, at these momenta, the ρ^- meson dominates the $\pi^-\pi^0$ mass spectrum. The data were analyzed allowing a small amount of hadronic background to interfere with the dominant electromagnetic production of the ρ^-. The results were used to extract a new value, $\Gamma(\rho^- \rightarrow \pi^-\gamma) = 67 \pm 7$ KeV, for the radiative decay width of the ρ^- meson. This value for $\Gamma(\rho^- \rightarrow \pi^-\gamma)$, a factor of two larger than an earlier measurement, alleviates previous inconsistencies in the interpretation of vector-meson radiative decays in terms of models based on SU(3) symmetry.

TABLE OF CONTENTS

	Page
VITAE	ii
ACKNOWLEDGMENTS	iii
ABSTRACT	v
LIST OF TABLES	viii
LIST OF FIGURES	ix
CHAPTER	
I. INTRODUCTION	1
A. A Quark-Model Calculation of Meson Radiative Decays	5
B. Coherent Nuclear Processes	8
C. Coulomb Production	13
D. Hadronic Contribution to Coherent ρ Production	15
II. EXPERIMENTAL TECHNIQUE	19
A. General Considerations Regarding the Spectrometer	19
B. Properties of the Beam	22
C. Drift Chamber System	29
D. Liquid Argon Calorimeter	36
E. The Trigger	42
F. Targets	53
G. On-Line Data Acquisition and Monitoring	55
III. CALIBRATION AND RESOLUTION	58
A. Introduction	58

Page

B. Calibration and Alignment of Drift Chambers 58

C. Calibration of the Liquid Argon Calorimeter 64

D. Resolution as Indicated by K-Decays 72

IV. DATA REDUCTION 80

A. Introduction 80

B. Charged-Track Reconstruction 81

C. Photon Reconstruction 84

D. Checks for Run to Run Consistency 87

V. NORMALIZATION 90

A. Introduction 90

B. Corrections Independent of Kinematics 91

C. Kaon Decays 97

D. $\Delta^+(1232)$ Production 114

VI. THE RHO DATA 123

A. Introduction 123

B. Comparison of ρ Data to the Monte Carlo Model 127

C. Calculation of Cross Sections 135

D. The $\pi^-\pi^0$ Mass Spectrum 137

E. Fits to the t-Distributions 143

F. Conclusions 153

REFERENCES 155

APPENDIX A 165

LIST OF TABLES

Table		Page
I	Properties of the targets	54
II	Correction factors for beam flux	93
III	Target-dependent correction factors	93
IV	Results from an event-by-event examination of K-decays occurring in the decay pipe	110
V	Correction factors to be applied in determining the cross section for the process $\pi^- A \rightarrow A\pi^-\pi^0$	136
VI	Results of parameterization of data	151
VII	Integrated cross sections for coherent ρ production on nuclei	152

LIST OF FIGURES

1. a) Diagram for the photoproduction of a vector meson from a nuclear target.

b) Diagram for Primakoff production of a vector meson in the Coulomb field of a nucleus of charge Z. (Page 3).

2. a) Diagram illustrating the kinematics for the coherent reaction $a + A \rightarrow A + a^*$.

b) Diagram for the Coulomb production reaction $\pi^- A \rightarrow A\rho^-$ in the rest frame of the ρ^- (Gottfried-Jackson frame).

c) Gottfried-Jackson reference frame for the coherent process $\pi^- A \rightarrow A\ \pi^-\pi^0$.

d) Helicity reference frame for the coherent process $\pi^- A \rightarrow A\ \pi^-\pi^0$. (Page 10).

3. Theoretically predicted Coulomb and hadronic ρ production cross sections on carbon and lead at 150 GeV/c. The parameters $\Gamma(\rho^- \rightarrow \pi^-\gamma)$ and C_s were scaled from the previously measured values (see Refs. 3,4). (Page 18).

4. Schematic diagram of the spectrometer. (Page 21).

5. Schematic diagram of the beam-transport system for the M-1 beamline at Fermilab. The elements Qi are quadrapole magnets, Bi are bending magnets, Ci are collimators, and Vi are vernier magnets. The nominal

half width of the beam envelope transported by this system is shown at the bottom. (Page 23).

6. Detection efficiency for the Cerenkov counter K1 as a function of helium pressure at beam momenta of 156 GeV/c and 260 GeV/c. K1 is the signal from the Cerenkov counter, and B0·B1 and B are signals defining the beam (see Chapter II.E). The arrows indicate the operating points used during the experiment. (Page 26).

7. Detection efficiency for Cerenkov counter K2. The terms are as defined in Fig. 6. The open circles at 156 GeV/c were obtained by requiring an additional coincidence between the K2·B signal and the K1 signal for the operating conditions indicated in Fig. 6a. (Page 27).

8. Detection efficiency for Cerenkov counter K3. The terms are as defined in Fig. 6. The efficiency for detecting kaons is indicated by the points requiring the additional coincidence with counter K1 operated at the pressure indicated in Fig. 6. (Page 28).

9. Drift-chamber read-out and calibration system. (Page 31).

10. Schematic diagram for the assembly of the liquid argon calorimeter. (Page 37).

11. a) Block diagram of the electronics for one channel of the LAC.

b) Signal at point ⓐ of the above diagram.

c) Read-out system for the configuration of LAC amplifiers used in the experiment. (Page 40).

12. Schematic of the arrangement of scintillation counters used in the experiment. (Page 43).

13. Diagram of the Logic used to define the RHO trigger. (Page 44).

14. Diagram of the logic associated with the LAC, defining the signal γ-logic. (Page 51).

15. Schematic diagram of the on-line data acquisition system. (Page 56).

16. Distribution of the sum of the squares of deviations from straight line resulting from calibration of the LRS 2770A TDC units. (Page 60).

17. Plots of the calibration constants for two LRS 2770A TDC channels as a function of time. (Page 61).

18. Plots of TDC time versus projected beam position for two drift planes. (Page 63).

19. Energy calibration coefficients for all strips in the front half of the LAC. (Page 68).

20. a) Energy measured by the LAC versus momentum measured by the drift chambers and analyzing magnet for electrons from the Ke3 decay process.

b) Energy resolution of the LAC (standard deviation squared) as a function of electron momentum. The dashed line corresponds to a resolution function of the form $\sigma_E/E \sim 17\% /\sqrt{E}$. (Page 70).

21. Plot of the difference between the X-position of the electron measured by the drift chambers and the X-position measured by the LAC for electrons from Ke3 decays. (Page 71).

22. Distributions of two-photon masses for K-decay events at 156 GeV/c and 260 GeV/c. The arrows indicate the limits used to define $K^- \rightarrow \pi^-\pi^0$ decays. The smooth curves are predictions of the Monte Carlo model normalized to the number of events contained between the arrows. (Page 74).

23. Distributions of the total energy of $\pi^-\pi^0$ systems resulting from K-decays. Our standard restrictions on decay vertex, single photon energy, and two-photon mass define the total sample. When our additional restrictions are imposed on the $\pi^-\pi^0$ mass and on t, the events in the shaded region are removed from the data. The arrows indicate the additional limits imposed on the energy used for defining $K^- \rightarrow \pi^-\pi^0$ events. The smooth curves are Monte Carlo predictions normalized to the number of events in the unshaded region. (Page 76).

24. t-distributions for $K^- \to \pi^-\pi^0$ events accumulated with a lead target at 156 GeV/c and 260 GeV/c, and no target in place (MT) at 156 GeV GeV/c. The smooth curves are the predictions of the Monte Carlo model. (Page 77).

25. Distributions of the $\pi^-\pi^0$ mass for $K^- \to \pi^-\pi^0$ decays at 156 GeV/c and 260 GeV/c. The smooth curves are the predictions of the Monte Carlo normalized to the total number of events in the distributions. The arrows indicate the limits imposed to define the $K^- \to \pi^-\pi^0$ signal. (Page 79).

26. a) Yield of reconstructed $K^- \to \pi^-\pi^0$ events as a function of time.

    b) Average value of the reconstructed $\gamma\gamma$ mass of π^0's from $K^- \to \pi^-\pi^0$ decays as a function of time. (Page 89).

27. Decay-vertex distributions for $K^- \to \pi^-\pi^0$ events at 156 GeV/c and 260 GeV/c. The arrows indicate the data sample chosen for studies of resolution and normalization. The smooth curves are predictions of the Monte Carlo normalized to the number of events contained between the arrows. (Page 100).

28. Distributions in the square of the transverse distance of the π^- from beam center for $K^- \to \pi^-\pi^0$ decays at 156 GeV/c and 260 GeV/c. The plotted

events have been restricted to the indicated regions of π^o energies. The smooth curves are predictions of the Monte Carlo. (Page 102).

29. Distributions of the separation between the π^- and the nearest photon, calculated at the position of the LAC for $K^- \rightarrow \pi^-\pi^o$ decays at 156 GeV/c and 260 GeV/c. The smooth curves are predictions of the Monte Carlo. (Page 103).

30. Decay-angle distributions in the helicity frame for the process $K^- \rightarrow \pi^-\pi^o$ at 156 GeV/c and 260 GeV/c. The smooth curves are predictions of the Monte Carlo, assuming an isotropic decay of the K^-. (Page 105).

31. Distributions in the energy asymmetry for the two photons from π^o decays resulting from $K^- \rightarrow \pi^-\pi^o$ decays at 156 GeV/c and 260 GeV/c. In a) and b) the standard cuts used for defining $K^- \rightarrow \pi^-\pi^o$ events have been applied. In c) and d) additional restrictions have been imposed on the π^o energy. The smooth curves are predictions of the Monte Carlo. (Page 106).

32. a) Electron momentum spectrum for the decay process $K^- \rightarrow e^-\bar{\nu}\pi^o$ at 156 GeV/c. The smooth curve is the prediction of the Monte Carlo. b) Decay-vertex distribution for these events. The arrows indicate

the limits used to select $K^- \to e^-\bar{\nu}\pi^o$ events for other studies. The smooth curve is the prediction of the Monte Carlo normalized to the number of events between the arrows. (Page 108).

33. Plots of the effective reconstruction efficiencies for the decay processes $K^- \to \pi^-\pi^o$, $K^- \to e^-\bar{\nu}\pi^o$ and $K^- \to \pi^-\pi^o\pi^o$ versus target material. (Page 112).

34. t-distributions for the coherent process $p + Pb \to Pb + (p\pi^o)$ at 156 GeV/c. For the upper curve there is no restriction on the mass of the $(p\pi^o)$ system, whereas, for the lower curve it is required that $1.14 \text{ GeV} < M_{p\pi^o} < 1.28 \text{ GeV}$. (Page 116).

35. Distribution of the interaction vertex for production of $(p\pi^o)$ systems at $t < 0.001 \text{ GeV}^2$ and with $1.14 \text{ GeV} < M_{p\pi^o} < 1.28 \text{ GeV}$. The data have been corrected for target-empty background. The smooth curve is the prediction of the Monte Carlo. The arrows indicate the limits imposed to define interactions occurring in the target. (Page 118).

36. a) Mass acceptance of the spectrometer for the process $\Delta^+ \to p\pi^o$.

    b) Cross section for the process $p\ Pb \to Pbp\pi^o$ at small t as a function of $M_{p\pi^o}$. The solid curve is the prediction for Coulomb production of $\Delta^+(1232)$ based on measurements for the process $\gamma p \to p\pi^o$.

(Page 119).

37. Decay-angle distribution in the Gottfried-Jackson frame for ($p\pi^o$) production on lead at $t < 0.001$ GeV^2 and 1.14 GeV $< M_{p\pi^o} <$ 1.28 GeV. The smooth curve is the prediction of the Monte Carlo assuming a $1 + 3 \sin^2 \theta \sin^2\phi$ distribution for $\Delta(1232)$ decay. (Page 121).

38. $\pi^-\pi^o$ mass distributions for the coherent processes $\pi^- A \rightarrow A\pi^-\pi^o$ at 156 GeV/c, for lead, copper, and carbon targets. The arrows indicate the limits used to define the ρ^- signal. (Page 124).

39. Same as Fig. 38 but for lead copper and aluminum targets. (Page 125).

40. Same as Fig. 38 but for lead and copper targets at 260 GeV/c, and for the process $\pi^+ Pb \rightarrow Pb\pi^+\pi^o$ at 156 GeV/c. (Page 126).

41. Interaction-vertex distributions for the process $\pi^- Pb \rightarrow Pb\ \pi^-\pi^o$ at 156 GeV/c and 260 GeV/c. The smooth curves are the predictions of the Monte Carlo normalized to the total number of events in the distributions. The limits indicated by the arrows were used to define the ρ^- signal. (Page 129).

42. a),b) Distributions in the energy asymmetry for the two photons from π^o decays resulting from $\rho^- \rightarrow \pi^-\pi^o$

decays at 156 GeV/c and 260 GeV/c. The smooth curves are predictions of the Monte Carlo.
c), d) The acceptance-corrected ratio of the data from a) and b) to the corresponding $K^- \to \pi^-\pi^0$ data. The dashed lines are least squares fits to the data points. (Page 130).

43. a),b) Acceptance-corrected distributions of the decay angle in the Gottfried-Jackson frame for the process π^- Pb $\to$ Pb $\pi^-\pi^0$ at 156 GeV/c and 260 GeV/c. The dashed lines indicate the $\sin^2\theta$ shape expected for decays of coherently produced ρ^- mesons.
c),d) Same as c) and d) in Fig. 42. (Page 132).

44. Total energy for the process $\pi^- A \to A\pi^-\pi^0$ on a) carbon, and b) lead at 156 GeV/c. The shaded regions correspond to events at $t < 0.002$ GeV^2. The arrows indicate the cuts applied to this variable to define the coherent $\rho^- \to \pi^-\pi^0$ signal. (Page 134).

45. Acceptance-corrected $\pi^-\pi^0$ mass spectrum for the process π^- Pb$\to$ Pb$\pi^-\pi^0$ at small t at 156 GeV/c. The smooth curve above the distribution gives the mass acceptance of the apparatus for a $\sin^2\theta \sin^2\phi$ decay of the ρ^-. The solid and dashed curves are fits of the data in the region between the arrows to the Breit-Wigner shapes described in the text.

(Page 138).

46. Same as Fig. 45 for data at 260 GeV/c. (Page 139).

47. t-distributions for the process $\pi^- A \rightarrow A\, \pi^- \pi^0$ at 156 GeV/c for lead, copper and carbon targets. The dashed lines are fits of the data to the model, including Coulomb and strong production of the ρ^-, as described in the text. (Page 144).

48. Same as Fig. 47 but for lead, copper and aluminum targets. (Page 145).

49. Same as Fig. 47 but for lead and copper targets at 260 GeV/c, and for the process $\pi^+ Pb \rightarrow Pb\pi^+\pi^0$ at 156 GeV/c. (Page 146).

50. a) Schematic diagram illustrating the assembly of a drift-chamber doublet from the D1 or D2 units. Spacers used to maintain uniform gaps between the planes, and bolts used to hold the assembly rigid are not shown. Also, for clarity, only a few of the wires are shown, and only one of several signal feedthroughs is shown.

b) Cross section of a single drift cell, with typical operating voltages indicated next to the field-shaping wires.

c) Voltage divider circuit used for supplying the voltages to the field-shaping wires.

d) Efficiency for detecting beam particles as a function of voltage gradient for one drift chamber. The arrow indicates the point at which these chambers were operated during the experiment. (Page 166).

CHAPTER I

INTRODUCTION

Because the photon is one of the best understood objects in the domain of particle physics, it is a very useful probe for studying other systems. For example, our understanding of atomic and nuclear structure has developed to a large extent from measurements of processes that involve radiative transitions. When one probes further into the structure of matter, one finds that studies of photon-hadron interactions also yield valuable information about the structure and properties of elementary strongly interacting particles.[1]

One of the simplest radiative processes accessible to experimental probing and to theoretical interpretation is the transition of a vector meson to a pseudoscalar meson through the emission of a photon ($V \rightarrow P+\gamma$). Although, prior to our work, several attempts had been made to develop a theory which could explain data for these transitions, the results were not terribly compelling.[2] Particularly frustrating to theoretical calculations was the old value of the radiative decay width of the ρ^- meson: $\Gamma(\rho^- \rightarrow \pi^-\gamma) = 35 \pm 10$ KeV.[3,4] This measurement was about three standard

deviations below predictions based on simple constituent quark models for hadrons, thus providing one of the main motivations for our experiment to remeasure $\Gamma(\rho^- \to \pi^- \gamma)$.

Radiative transitions have been measured using three different techniques. Direct measurements of the decays $V \to P+\gamma$ are usually not feasible because of the small partial rates for these processes. The inverse reaction, as depicted in Fig 1.a, can be studied by photoproducing the vector meson through the exchange of a virtual pseudoscalar meson between a nuclear target and an incident photon. However, several different hadronic exchanges can contribute to the same production process; thus calculations needed to extract radiative widths tend to depend on ambiguous models of hadronic production. Reversing the role of beam and target is more advantageous. An incident pseudoscalar meson can then absorb a virtual photon from the Coulomb field of the nucleus (Primakoff process) to form a vector meson, as shown in Fig 1.b. There will be hadronic-exchange processes (ω, A_2) also contributing, but, as will be demonstrated below, Coulomb production, which is well understood, will tend to dominate other mechanisms at high incident beam energies, allowing a less ambigous extraction of radiative widths.

a) PHOTOPRODUCTION

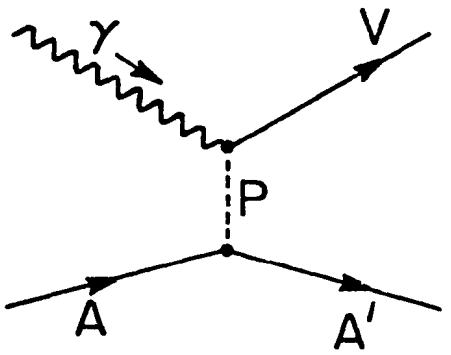

b) PRIMAKOFF EFFECT

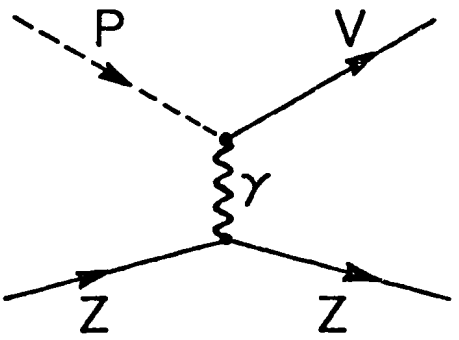

Figure 1

We report in this thesis our remeasurement of the radiative width, $\Gamma(\rho^- \to \pi^-\gamma)$, which was carried out through a study of the same coherent reaction as in the previous experiment,[3,4] namely:

$$\pi^- A \longrightarrow A\rho^- \quad \hookrightarrow \pi^-\pi^0 , \qquad (1)$$

where A represents targets of different nuclear mass number. The theoretical framework needed to describe this reaction is discussed in this chapter. The experimental apparatus is described in Chapter II, and studies of the calibration and resolution of the different components of the spectrometer are presented in Chapter III. The method used to process the data is outlined in Chapter IV, and in Chapter V we discuss the normalization of the production cross section. In Chapter VI we present our analysis of the data for Reaction (1), and extract the value of $\Gamma(\rho^- \to \pi^-\gamma)$.

We continue this chapter with an illustration of a calculation of radiative widths, based on a simple quark model. The characteristics of coherent production on nuclear targets are outlined in Section B. The Primakoff process and the nature of the background from strong-exchange mechanisms are discussed in Sections C and D, respectively.

A. A Quark-Model Calculation of Meson Radiative Decays

There is now overwhelming evidence suggesting that hadrons are composed of more fundamental entities called quarks.[5] The scheme most commonly referred to is the one introduced by Gell-Mann[6] and Zweig,[7] wherein a baryon is made up of three quarks, an antibaryon of three antiquarks, and a meson of a quark and an antiquark. Prior to the discovery of the J/ψ particle in 1974,[8] all known states could be formed from the basis of three quarks (u,d,s) and three antiquarks ($\bar{u},\bar{d},\bar{s}$). The quarks all have spin 1/2, baryon number 1/3, and charges 2/3, -1/3, and -1/3 times the electron charge for u, d, and s, respectively. The antiquarks have baryon number -1/3 and charge opposite that of the corresponding quark. The states which are of concern in this thesis can all be described in terms of these quarks.

The radiative decay of a vector meson to a pseudoscaler meson can be viewed as an M1 transition from a $^3S_1$ to a $^1S_0$ state of the quark-antiquark system. This idea was first proposed in 1965,[9] and initial calculations were in reasonable agreement with the measured rate for $\omega^0 \to \pi^0\gamma$ decay.

The magnetic moment operator for the $V \to P+\gamma$ transition can be written in the nonrelativistic approximation as:[10]

$$\mathcal{M} = \sum_j \left[\frac{e\hbar}{2M_j c} \vec{L}_j \cdot (\vec{k} \times \vec{\varepsilon}_a) + \mu_p q_j \vec{\sigma}_j \cdot (\vec{k} \times \vec{\varepsilon}_a) \right] \exp(i\vec{k}\cdot\vec{r}_j) .$$

The sum is taken over the quarks in the system, with M_j being the mass, $\vec{L}_j$ the orbital angular momentum, q_j the charge, and $\vec{\sigma}_j$ the spin operator for the jth quark. The emitted photon has momentum $\vec{k}$ and polarization $\vec{\varepsilon}_a$ in the rest frame of the initial state, and $\mu_p = 2.79e\hbar/2M_p c$ is the magnetic moment of the proton. The intrinsic quark moment is assumed to be proportional to the proton magnetic moment, varying as the quark charge. (This assumption produces excellent agreement with the observed ratio of the proton to neutron magnetic moments.) We can neglect the orbital term since the quarks are in a relative S-state for the transitions of interest. Furthermore, the long wavelength approximation ($\exp(i\vec{k}\cdot\vec{r}) \approx 1$) is assumed to be valid for these transitions.[11] Thus the transition operator reduces to

$$\mathcal{M} \approx \sum_j \mu_p q_j \vec{\sigma}_j \cdot (\vec{k} \times \vec{\varepsilon}_a) .$$

The radiative width for the process $a \to b + \gamma$ can be calculated from[12]

$$\Gamma(a \to b\gamma) = \frac{4}{3} k_\gamma \sum_{\langle i \rangle, f} |\langle b_f | \mathcal{M} | a_i \rangle|^2$$

$$= \frac{\alpha}{3} k_\gamma^3 \frac{(2.79)^2}{M_p^2} \sum_{\langle i \rangle, f} \left| \sum_{j,\nu} \langle b_f | \sigma_j^{(\nu)} | a_i \rangle \right|^2 , \qquad (2)$$

where $k_\gamma = (M_a^2 - M_b^2)/2M_a$ is the decay momentum in the rest

frame of particle a, and the matrix elements are summed over the final states and averaged over the initial states. $\sigma_j^{(\nu)}$ is the νth component of the spin operator for the jth quark, and α is the fine structure constant ($e^2/\hbar c \approx 1/137$). The factor $(4/3)k_\gamma$ in front of the matrix element accounts for the phase space available to the decay products.[11]

We shall calculate the rates for the transitions $\omega^0 \to \pi^0\gamma$ and $\rho^- \to \pi^-\gamma$. The states of interest can be written as follows:

$$
\begin{aligned}
|\pi^0\rangle &= (1/2)(u\uparrow\bar{u}\downarrow - u\downarrow\bar{u}\uparrow + d\downarrow\bar{d}\uparrow - d\uparrow\bar{d}\downarrow) \\
|\pi^-\rangle &= \sqrt{1/2}\,(d\uparrow\bar{u}\downarrow - d\downarrow\bar{u}\uparrow) \\
|\rho^-_+\rangle &= d\uparrow\bar{u}\uparrow \\
|\rho^-_0\rangle &= \sqrt{1/2}\,(d\uparrow\bar{u}\downarrow + d\downarrow\bar{u}\uparrow) \\
|\rho^-_-\rangle &= d\downarrow\bar{u}\downarrow \\
|\omega^0_+\rangle &= \sqrt{1/2}\,(u\uparrow\bar{u}\uparrow + d\uparrow\bar{d}\uparrow) \\
|\omega^0_0\rangle &= (1/2)(u\uparrow\bar{u}\downarrow + u\downarrow\bar{u}\uparrow + d\uparrow\bar{d}\downarrow + d\downarrow\bar{d}\uparrow) \\
|\omega^0_-\rangle &= \sqrt{1/2}\,(u\downarrow\bar{u}\downarrow + d\downarrow\bar{d}\downarrow)
\end{aligned}
$$

The spin part of the wave function is indicated by the direction of the arrows, and the z-component of the spin state of the vector meson is indicated by the subscript +, -, or 0. Ideal mixing is assumed in the definition of the ω states; that is, the octet and singlet SU(3)-states are mixed in such a way that the physical ω contains no $s\bar{s}$ component.[13]

Substituting these states into Equation (2) yields

$$\Gamma(\omega^0 \to \pi^0\gamma) = \frac{\alpha}{3}\left(\frac{M_\omega^2 - M_{\pi^0}^2}{2M_\omega}\right)^3 \frac{(2.79)^2}{M_p^2}\left[\frac{1}{3}\left(\frac{1}{2}+\frac{1}{2}+1\right)\right] = 783 \text{ KeV}$$

$$\Gamma(\rho^- \to \pi^-\gamma) = \frac{\alpha}{3}\left(\frac{M_\rho^2 - M_{\pi^-}^2}{2M_\rho}\right)^3 \frac{(2.79)^2}{M_p^2}\left[\frac{1}{3}\left(\frac{1}{18}+\frac{1}{18}+\frac{1}{9}\right)\right] = 84 \text{ KeV}$$

The ratio of these two widths, $\Gamma(\omega^0 \to \pi^0\gamma)/\Gamma(\rho^- \to \pi^-\gamma)$, is 9.32, as compared to the previously determined experimental ratio (880±61 KeV)/(35±10 KeV) =25±7. The terms shown in square brackets correspond to just the SU(3) Clebsch-Gordan coefficients for the matrix elements. Thus, if SU(3) symmetry were exact, these terms would yield an expected ratio of 9. The fact that the ω and ρ masses are nearly the same makes it quite difficult to introduce a scheme for symmetry breaking which could account for the previous experimental ratio for these transitions. Because the rate for $\omega^0 \to \pi^0\gamma$ is large enough to be measured directly with little ambiguity,[14] it was important to check the value of $\Gamma(\rho^- \to \pi^-\gamma)$.

B. Coherent Nuclear Processes

The reaction a + A → A + a*, where a is the incident projectile and a* a produced system, will be referred to as being coherent if the recoiling nucleus remains in the ground state, or, less rigorously, in some low-lying excited state.[15]

The kinematics for this reaction are illustrated in Fig. 2.a. The invariant square of the four-momentum transfer will be defined as $t = q^2 = |(p_{a^*} - p_a)^2|$ (the terms used here are the four momenta of the particles). The minimum possible momentum transfer required to produce the state a^* is

$$t_{min} \equiv -(E_{a^*} - E_a)^2 + (|\vec{p}_{a^*}| - |\vec{p}_a|)^2 \approx \frac{(M_{a^*}^2 - M_a^2)^2}{4|\vec{p}_a|^2},$$

where $\vec{p}_a$, E_a, and M_a are the momentum, energy, and mass of the incident projectile, and $\vec{p}_{a^*}$, E_{a^*}, and M_{a^*} the momentum, energy, and mass of the produced system; these quantities are defined in the laboratory frame.

If we set $|\vec{q}|^2 = q_\ell^2 + q_T^2$, where q_ℓ and q_T are the longitudinal and transverse components of the three-momentum transfer, then $t_{min} \approx q_\ell$. Requiring coherence over nuclear dimensions (radius $\sim 1.12A^{1/3}$ fermi) implies, from the uncertainty principle, that q_T must be restricted to $\lesssim \hbar/(1.12A^{1/3})$. Thus, coherent production is expected to be dominated by small momentum transfers. For a lead target, for example, $q_T \lesssim 35$ MeV/c.

The requirement that the nucleus remain in its ground state greatly restricts the allowed coherent final states, a^*, that can be produced. For incident mesons, for example, when only momentum can be transferred between the projectile and target, orbital excitation is possible, with a

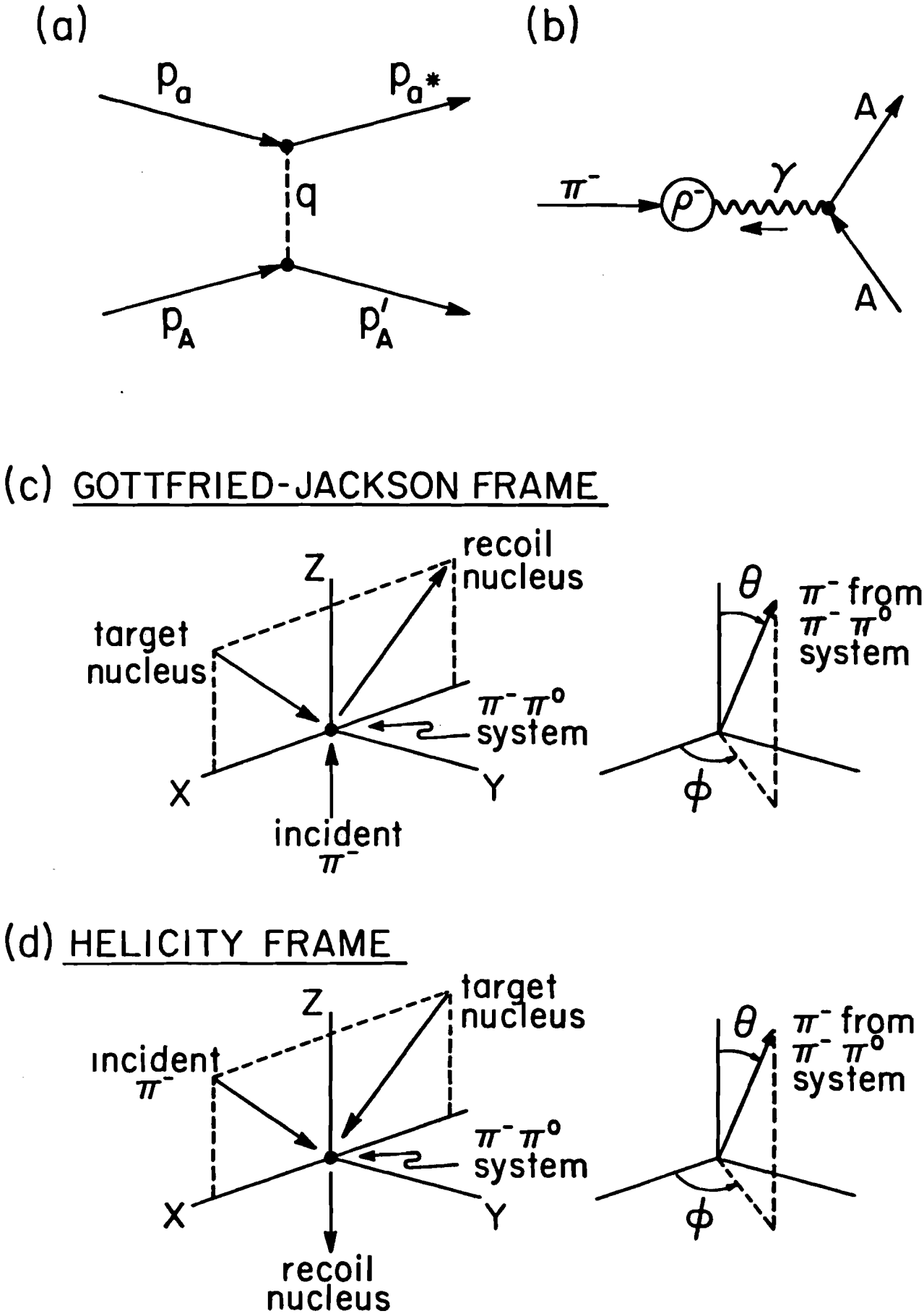
(a)
p_a
p_{a*}
q
p_A
p'_A
(b)
π^-
ρ^-
γ
A
A
(c) GOTTFRIED-JACKSON FRAME
Z
recoil nucleus
target nucleus
$\pi^-\pi^0$ system
X
Y
incident π^-
θ
π^- from $\pi^-\pi^0$ system
ϕ
(d) HELICITY FRAME
Z
target nucleus
incident π^-
$\pi^-\pi^0$ system
X
Y
recoil nucleus
θ
π^- from $\pi^-\pi^0$ system
ϕ

Figure 2

corresponding parity change between a and a^* of $(-1)^{\ell}$ (these processes involve production of "unnatural parity" states of spin-parity $J^P = 0^-, 1^+, 2^-, \ldots$). Away from the forward direction, parity changes of $(-1)^{\ell+1}$, that are ruled out by conservation of angular momentum at $t=t_{min}$, may also occur. In this instance helicity flip is involved and the exchanged objects have effective spin-parity values of $J^P = 1^-, 2^+, 3^-, 4^+ \ldots$ The coherent production of ρ mesons involves these types of exchanges.

Additional selection rules apply to processes with incident pions. Isospin and G-parity must be conserved at the $p_a - p_{a^*} - q$ vertex. The photon has both I=0 and I=1 components. G-parity conservation allows only the isoscalar part of the photon to couple to the $\rho\pi$ vertex. Strong processes with I=1 exchange are greatly suppressed because roughly half of the nucleons (protons) have isospin up and the other half (neutrons) have isospin down, tending to cancel each other in a coherent sum. Thus, ω-exchange ($J^P = 1^-$, $I^G = 0^-$) is expected to dominate, for example, over A_2-exchange ($J^P = 2^+$, $I^G = 1^-$) in hadronic production of ρ mesons.

Figure 2.b depicts Reaction (1) in the rest frame of the produced ρ^-. The incident pseudoscalar meson can be regarded as a plane wave, which can be expanded in terms of the spherical harmonic wave functions, Y_ℓ^0. The photon has

spin one and only two helicity states, hence the spin of the ρ^- must match that of the photon, and point either along or opposite the direction of the incident beam (in the Gottfried-Jackson frame). Although for the case of an exchanged ω, three helicity states are possible, the state with zero projection cannot couple to a plane wave (proportional to Y_1^0 as required by parity conservation) to form a ρ^-. This fact should be evidenced in the angular distribution of the decay products of the ρ^-.

The directions defining the Gottfried-Jackson reference frame for describing coherent processes are shown in Fig. 2.c. The trajectory of the π^- from the decay $\rho^- \rightarrow \pi^- \pi^0$ should exhibit an angular distribution characterized by the form $|Y_1^1(\theta,\phi) + Y_1^{-1}(\theta,\phi)|^2$, namely, $\sin^2\theta \sin^2\phi$. Another reference frame frequently used for describing particle decay is the s-channel helicity frame depicted in Fig. 2.d. Here the axis of quantization is the line of flight of the produced object. In the case of Coulomb production at high energies, the two reference frames are nearly the same.

C. Coulomb Production

In 1951 Primakoff suggested that π^0 mesons could be photoproduced in the electromagnetic field of a nucleus, and that the characteristics of this process could be used to determine the lifetime of the π^0.[16] The suggested experiment has proved to be technically more demanding than initially anticipated, and many years passed prior to an accurate determination of the pion lifetime through this technique.[17] Meanwhile, several other applications of the Primakoff effect were proposed.[18] We discuss below the features of this electromagnetic production mechanism as it relates to Reaction (1).

The cross section for Coulomb production of a system of mass M_{a^*} in the reaction $a+A \rightarrow A+a^*$ is determined by the amplitude $\mathcal{T}_C$:[19]

$$\frac{d\sigma_C}{dt\,dM^2_{a^*}} = \left|\mathcal{T}_C\right|^2 = \frac{Z^2\alpha}{\pi}\,\frac{\sigma_\gamma(M^2_{a^*})}{(M^2_{a^*}-M^2_a)}\,\frac{t-t_{min}}{t^2}\left|F_{EM}(t)\right|^2, \qquad (3)$$

where Z is the nuclear charge, and $F_{EM}(t)$ is the effective nuclear form factor, containing absorption of incoming and outgoing states in nuclear matter (details concerning this factor will be presented in Chapter VI). $\sigma_\gamma(M^2_{a^*})$ represents the cross section for the reaction $\gamma a \rightarrow a^*$ at a center of mass (C. M.) energy M_{a^*}, and is given by:

$$\sigma_\gamma(M^2_{a^*}) = \frac{2\pi^2}{q^{*2}}\,\frac{(2J_{a^*}+1)}{(2J_a+1)}\left|T(\gamma a \rightarrow a^*)\right|^2 \qquad (4)$$

J_a is the spin of the incident particle, J_{a^*} is the spin of the produced system, and q^* is the momentum of the photon in the C. M. system of a^*:

$$q^* = \frac{M_{a^*}^2 - M_a^2}{2 M_{a^*}}$$

The form of the $\gamma\pi^- \to \pi^-\pi^0$ transition matrix applicable to ρ production will be discussed in Chapter VI. In the narrow-resonance approximation Equation (4) becomes[19]

$$\sigma_\gamma(M_{a^*}^2) = \frac{2\pi^2}{q^{*2}} \frac{(2J_{a^*}+1)}{(2J_a+1)} M_{a^*} \Gamma(a^* \to a\gamma) ,$$

where $\Gamma(a^* \to a\gamma)$ is the radiative decay width of a^*. Substituting this expression into Equation (3), we obtain the cross section for production of a well defined resonance in the nuclear Coulomb field:

$$\frac{d\sigma_C}{dt} = 8\pi\alpha Z^2 \frac{(2J_{a^*}+1)}{(2J_a+1)} \Gamma(a^* \to a\gamma) \left(\frac{M_{a^*}}{M_{a^*}^2 - M_a^2}\right)^3 \frac{t - t_{min}}{t^2} \left| F_{EM}(t) \right|^2 \tag{5}$$

From this equation we note the following unique features of Coulomb production.

1) As pointed out in Section B, the cross section vanishes in the forward direction ($t=t_{min}$). However, the photon propagator ($1/t^2$) greatly enhances production near the forward region; in fact, the maximum in the cross section occurs at $t=2t_{min}$. The value of the cross section at this maximum increases as $|\vec{p}_a|^2$.

2) Due to the decrease of t_{min} with increasing $|\vec{p}_a|$, the integrated cross section for Coulomb production increases asymptotically as $\log(|\vec{p}_a|)$. Thus, because exclusive cross sections involving hadron exchanges fall with increasing energies,[20] Coulomb production eventually comes to dominate coherent processes, particularly at small t.

3) The electromagnetic form factor, $F_{EM}(t)$, has a shape characteristic of the size of the nucleus. For high incident energies, this factor is not very sensitive to absorption of incident and outgoing states, and has a weak t-dependence over the range dominated by the Coulomb process. Hence, theoretical predictions are not expected to be complicated by factors which depend on parameters used to describe the nucleus.

4) The cross section changes as Z^2 for different target materials. Thus, Coulomb production off heavy nuclei is greatly enhanced relative to strong production, which increases approximately as $A^{2/3}$ (see the following section).

D. Hadronic Contribution to Coherent ρ Production

As pointed out in section B of this chapter, coherent strong production of ρ mesons is expected to be dominated by ω-exchange. This contribution can be parameterized as:[21]

$$\frac{d\sigma_S}{dt} = |F_S|^2 = A^2 C_S (t - t_{min}) |F_H(t)|^2, \qquad (6)$$

where C_S is the normalization for production on a single nucleon, and $F_H(t)$ is the hadronic form factor of the nucleus, which like $F_{EM}(t)$ contains absorption corrections. Unlike the case of Coulomb production, where the effect of $F_{EM}(t)$ is rather small, absorption severely modifies the A dependence in Equation (6), yielding an effective dependence of $A^{2/3}$.

The $F_H(t)$ factor is computed using an optical model (see Chapter VI) in which the distribution of hadronic matter is taken to be the same as the charge distribution in the nucleus. But, due to strong absorption, only an outer ring (~1 fermi thick) will contribute appreciably to the amplitude F_S. In the forward direction the square of the form factor behaves like exp(-bt), where $b \sim R^2/4$, with R being the nuclear radius. Thus, using Equation (6), the cross section would be expected to peak at $t \sim (4/R^2)$. This value is almost independent of the incident energy, thus it is easier to separate the Coulomb contribution from ω-exchange as the incident energy increases. In addition, as mentioned previously, the integrated cross section for hadronic exchanges falls with energy as $|\vec{p}_a|^{-1}$, thus providing further advantage for studying electromagnetic production at high energies.

Figure 3 shows the Coulomb and hadronic cross sections expected for production on lead and on carbon nuclei at an incident energy of 150 GeV. For historical reasons, we used the previously obtained value of $\Gamma(\rho^- \to \pi^- \gamma)$=35 KeV, and the extrapolated value of C_S=0.6 mb/(GeV/c) , appropriate to 150 GeV/c.[3,4] The fall of the Coulomb cross section to zero at $t=t_{min}$ is not visible on the scale of this plot ($t_{min} \sim 4 \times 10^{-6}$ Gev^2 at 150 GeV/c). Also, experimental resolution has not been accounted for in these plots.

The hadronic and electromagnetic processes can interfere, and we can write the total cross section for coherent production on nuclei in the form

$$\frac{d\sigma}{dt} = \left| F_C + e^{i\phi} F_S \right|^2 , \qquad (7)$$

where ϕ is the relative phase of the Coulomb and strong amplitudes, and F_C is $\mathcal{F}_C$ integrated over the mass range of interest (e. g., the ρ interval). The data were fit to this expression by varying the parameters $\Gamma(\rho^- \to \pi^- \gamma)$, C_S, and ϕ . Details of this procedure and our extraction of a new value for $\Gamma(\rho^- \to \pi^- \gamma)$ will be presented in Chapter VI.

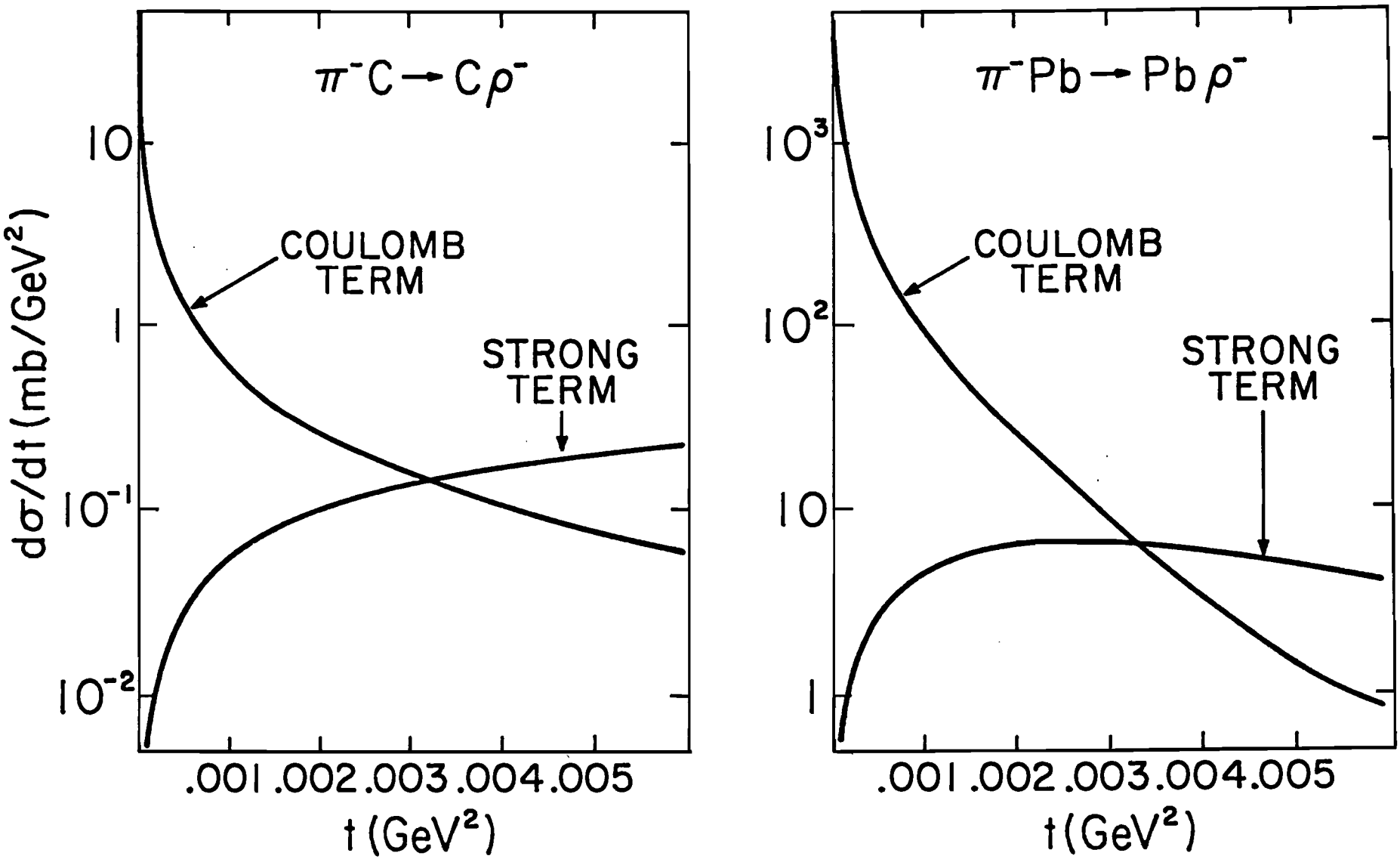
$\pi^- C \rightarrow C \rho^-$
$\pi^- Pb \rightarrow Pb \rho^-$
COULOMB TERM
STRONG TERM
COULOMB TERM
STRONG TERM
$d\sigma/dt$ (mb/GeV^2)
10
1
10^{-1}
10^{-2}
10^3
10^2
10
1
.001 .002 .003 .004 .005
t (GeV^2)
.001 .002 .003 .004 .005
t (GeV^2)

Figure 3

CHAPTER II

EXPERIMENTAL TECHNIQUE

A. General Considerations Regarding the Spectrometer

We describe in this chapter the experimental apparatus used for measuring the radiative width $\Gamma(\rho^- \to \pi^- \gamma)$. Some of the points which we considered in the design of the spectrometer are discussed below.

Integrating Equation (5) for a lead target, and using the previously measured value for $\Gamma(\rho^- \to \pi^- \gamma)$, one obtains a total Coulomb production cross section of 500 μb. This is less than 0.1% of the total π^-Pb cross section. Thus, to accumulate sufficient statistics for ρ^- events requires a trigger which suppresses a substantial amount of the remaining 99.9% of the cross section.

Another important concern is the resolution of the spectrometer. The very sharp intrinsic Coulomb peak is smeared out to larger t values by the finite resolution of the apparatus. This effect must be taken into account when making fits of the theoretical cross section to the data,

and, the poorer the resolution, the more difficult is it to separate Coulomb production from hadronic production. From the theoretical curves for ρ production on carbon and lead (Fig. 3), it was estimated that a resolution curve of the form exp(-2500t) should suffice for the measurement of $\Gamma(\rho^- \to \pi^- \gamma)$ to an accuracy of about 10%.

If we examine more closely the demands of this experiment, we find that it is necessary to balance requirements of resolution against statistics. The characteristics of the Primakoff process are such that the reaction products will be produced quite close to the beam trajectory. The beam intensity, therefore, cannot be so high as to seriously affect the resolution or efficiency of the detectors in the region of the beam. Also, although a thick target would provide more interactions, a thinner target would minimize the effect of multiple Coulomb scattering of the charged particles, and reduce the absorption of the reaction products, especialy photons.

After considering the above factors (and others, such as acceptance, triggering capability, cost and availability of material), we decided to use a system of drift chambers for measuring the charged particle trajectories and momenta, and a lead-liquid argon calorimeter for determining photon energies and positions. A schematic diagram of the spectrometer is shown in Fig. 4. The target box, the decay

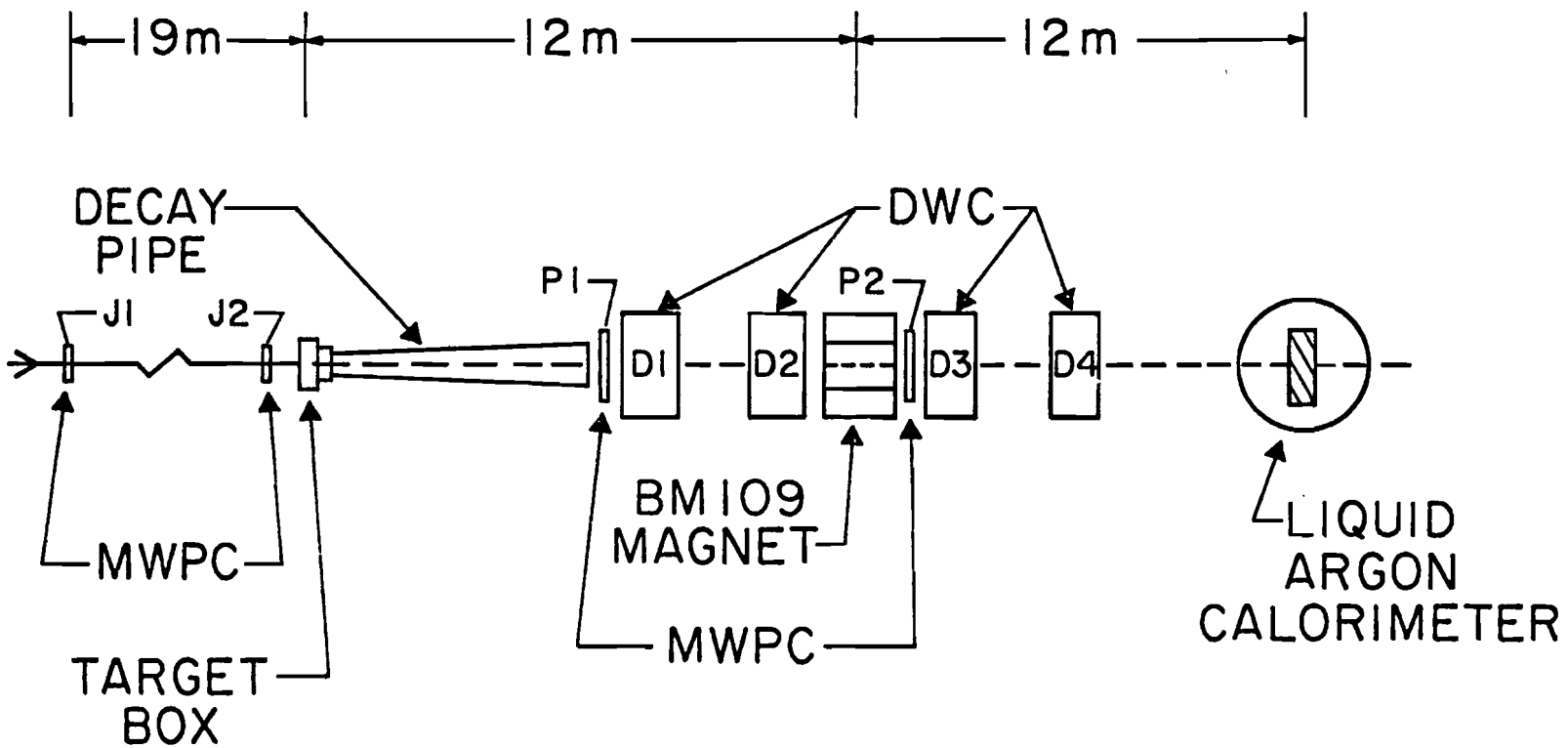
19m
12m
12m
DECAY PIPE
J1
J2
P1
P2
DWC
D1
D2
D3
D4
MWPC
TARGET BOX
BM109 MAGNET
MWPC
LIQUID ARGON CALORIMETER

Figure 4

pipe, and the region between the beam proportional chambers were evacuated to reduce multiple Coulomb scattering and background interactions. For the same reasons, all other spaces between chambers were filled with polyethylene bags containing helium gas.

Section B describes the parameters of the beam, Section C the drift chamber system, and Section D the lead-liquid argon calorimeter. The electronic triggering setup is detailed in Section E, the parameters of the targets used in this experiment are described in Section F, and Section G explains the on-line monitoring and data acquisition system.

B. Properties of the Beam

The spectrometer was set up in the East branch of the M-1 beamline at the Meson Laboratory of Fermilab.[22] Figure 5 shows a schematic of the transport system, and the nominal beam envelope as determined using the program TRANSPORT.[23]

The 400 GeV/c primary proton beam from the main ring was incident on a 1/16 in. x 1/16 in. x 8 in. long beryllium target used to generate secondary particles for the six beamlines in the Meson Laboratory. The M-1 beamline transmitted particles produced at ≈ 3.9 mr relative to the incident proton beam. The momentum spread of the beam was $\Delta p/p \lesssim \pm 2\%$, and the maximum acceptance for the tune which we

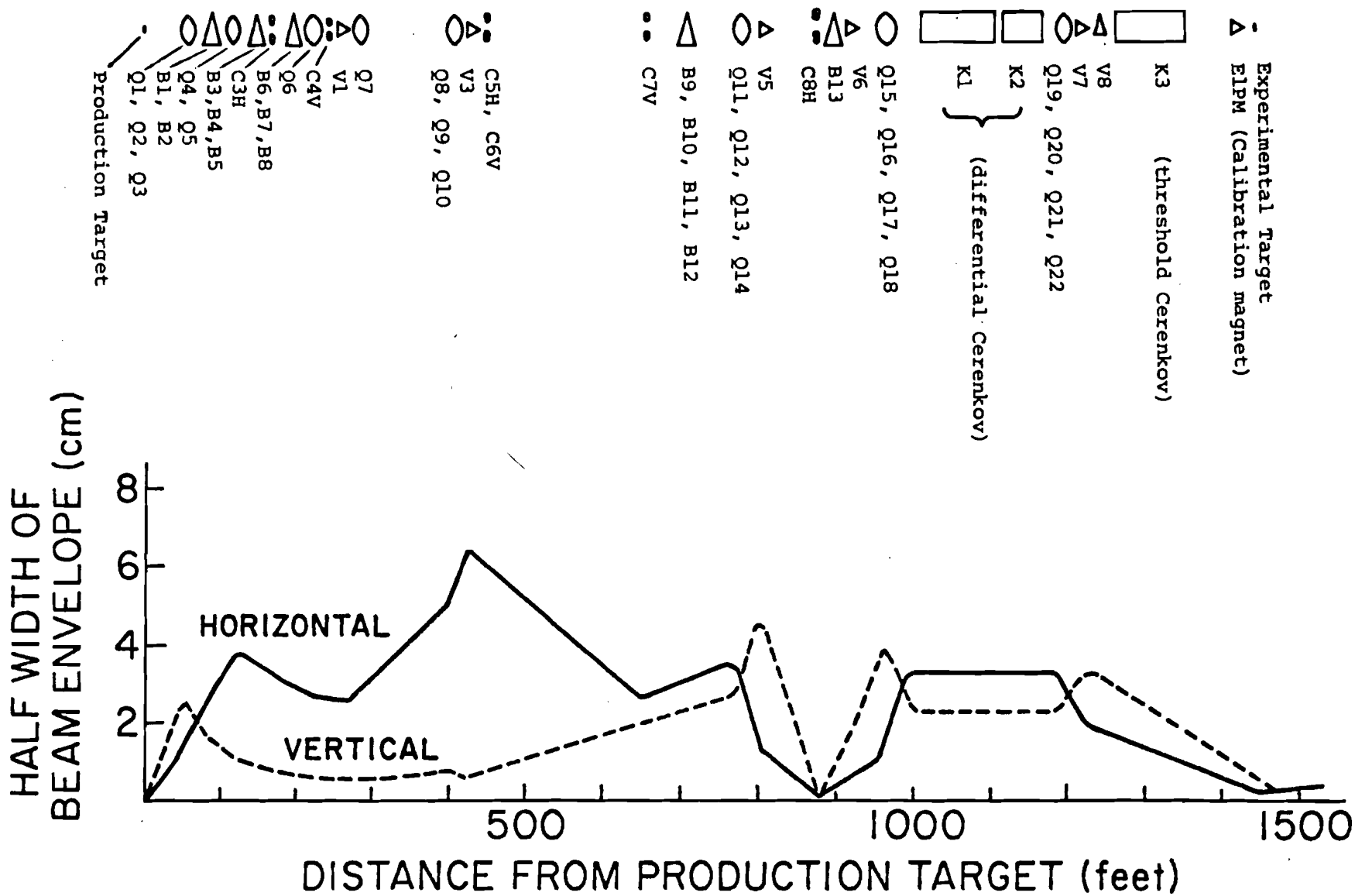
Experimental Target
ElPM (Calibration magnet)
K3 (threshold Cerenkov)
V8
V7
Q19, Q20, Q21, Q22
K2
K1
(differential Cerenkov)
Q15, Q16, Q17, Q18
V6
B13
C8H
V5
Q11, Q12, Q13, Q14
B9, B10, B11, B12
C7V
C5H, C6V
V3
Q8, Q9, Q10
Q7
V1
C4V
Q6
B6,B7,B8
C3H
B3,B4,B5
Q4, Q5
B1, B2
Q1, Q2, Q3
Production Target
HALF WIDTH OF BEAM ENVELOPE (cm)
8
6
4
2
HORIZONTAL
VERTICAL
500
1000
1500
DISTANCE FROM PRODUCTION TARGET (feet)

Figure 5

used was ≈ 2 μster%.

In the first stage of the beam, particles were focused at a momentum dispersed image located ~450 feet from the production target. A collimator (C5H) positioned at this focus was used to define the range of momenta that would be transmitted to the experimental area. In the second stage, the different momenta were recombined and refocused at ~880 feet.

The beam region between 1000 and 1175 feet consisted of a "parallel" section of small angular divergence which contained two differential Cerenkov counters. Counter K1 was 106 feet long and accepted light radiated at a 7.5 mr angle. K2 was 53 feet long and had a Cerenkov angle of 15 mr.[24] Light from these counters was focused onto a ring of six phototubes (RCA-C31000 M) located near the upstream ends of the tanks. Signals from adjacent phototubes were added together, and a triple coincidence was required to indicate the presence of the desired type of particle. An outer ring of phototubes on these counters, available for vetoing purposes, was not used in this experiment.

In addition, the region between 1240 and 1340 feet contained a 100 foot long threshold Cerenkov counter, K3.[25] This counter had two phototubes (RCA-31000 M), one that accepted light radiated at an angle less than 5 mr to the counter axis, and the other, light at angles greater than 5

mr. This counter was used in a pseudodifferential mode by requiring a signal from the inner phototube while vetoing on signals from the outer one.

All three counters were filled with helium, and the pressure in each was adjusted such that K1 would identify kaons, K2 would identify protons, and K3 would identify pions. Plots of detection efficiency versus pressure are shown in Figs. 6-8 for the three counters at both energies. (The definitions of the beam counts (B and B0•B1) will be given in Section E.) As can be seen, particle separation was very good at 156 GeV/c, but suffered somewhat at 260 GeV/c. Corrections due to background in the Cerenkov signals were small and will be detailed in Chapter V.

Through a laboratory-supported beamline computer system, with a terminal located in our electronics trailer, we had direct control over the elements in the M-1 beamline. Integrating wire chambers located at several positions along the beamline provided a monitor of the beam spot size. The beam intensity was controlled mainly by adjustments of collimator C4V, and was typically set to a rate of $2\text{-}5\times10^5$ particles/spill incident on our experimental target. Main accelerator control provided a series of reference times which indicated, for instance, the beginning and end of the main-ring "flat-top" (i. e. the time during which the beam was extracted from the main ring). These reference times

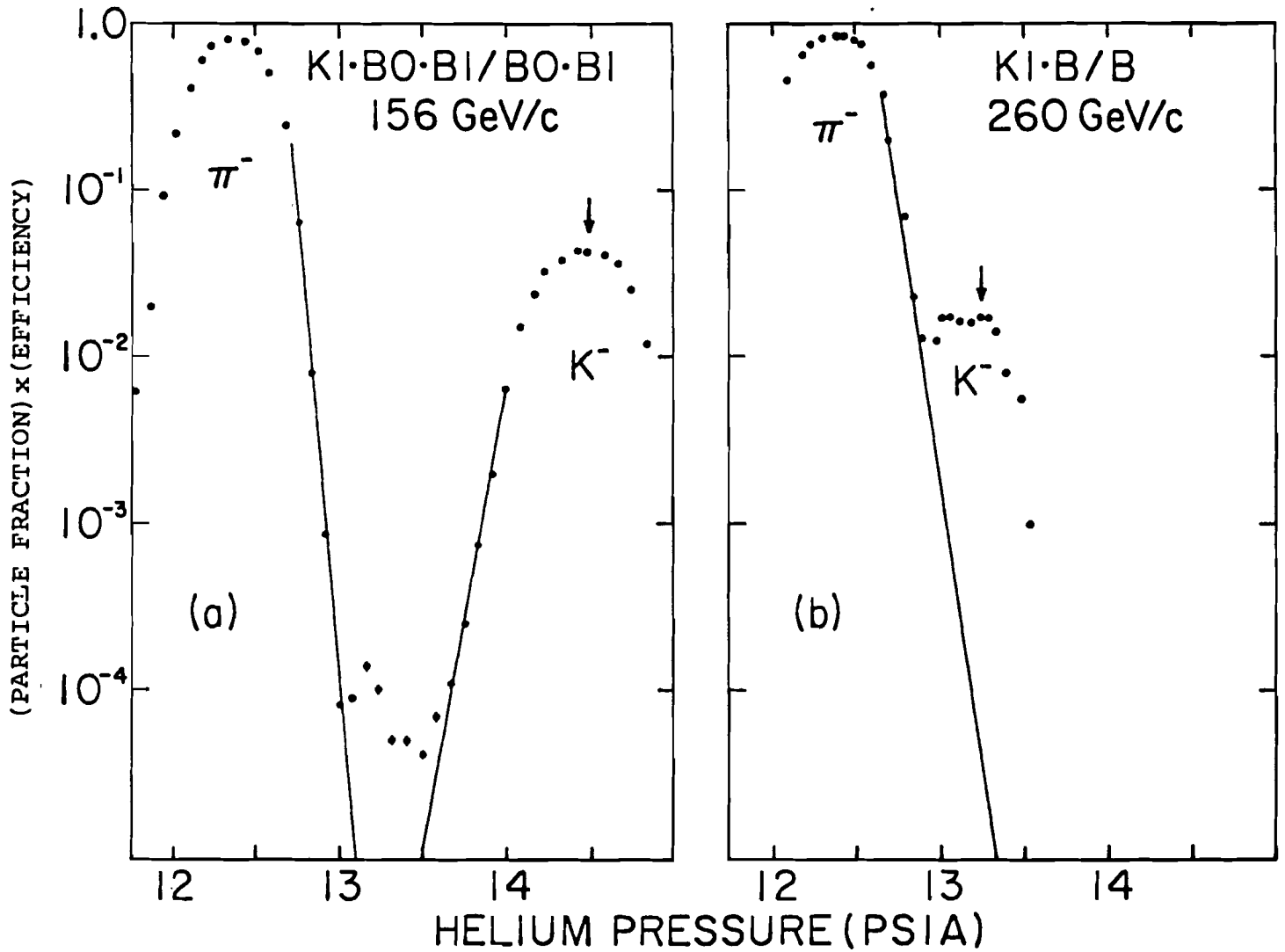
K1·B0·B1/B0·B1
156 GeV/c
K1·B/B
260 GeV/c
π⁻
K⁻
(a)
(b)
1.0
10⁻¹
10⁻²
10⁻³
10⁻⁴
(PARTICLE FRACTION) × (EFFICIENCY)
12
13
14
HELIUM PRESSURE (PSIA)

Figure 6

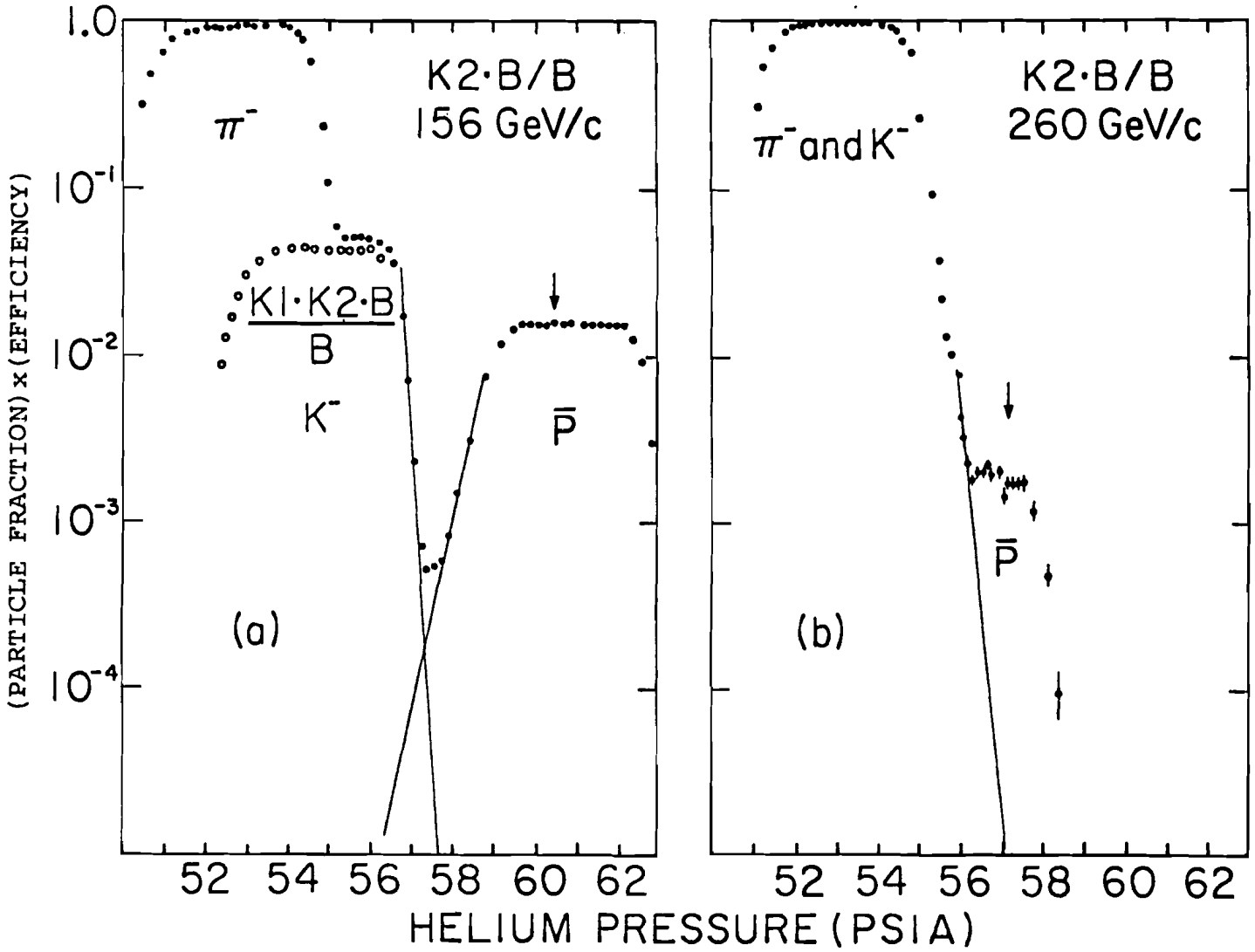
1.0
10^{-1}
10^{-2}
10^{-3}
10^{-4}
(PARTICLE FRACTION) x (EFFICIENCY)
K2·B/B
156 GeV/c
π^-
K1·K2·B / B
K^-
$\bar{P}$
(a)
K2·B/B
260 GeV/c
π^- and K^-
$\bar{P}$
(b)
52 54 56 58 60 62
52 54 56 58 60 62
HELIUM PRESSURE (PSIA)

Figure 7

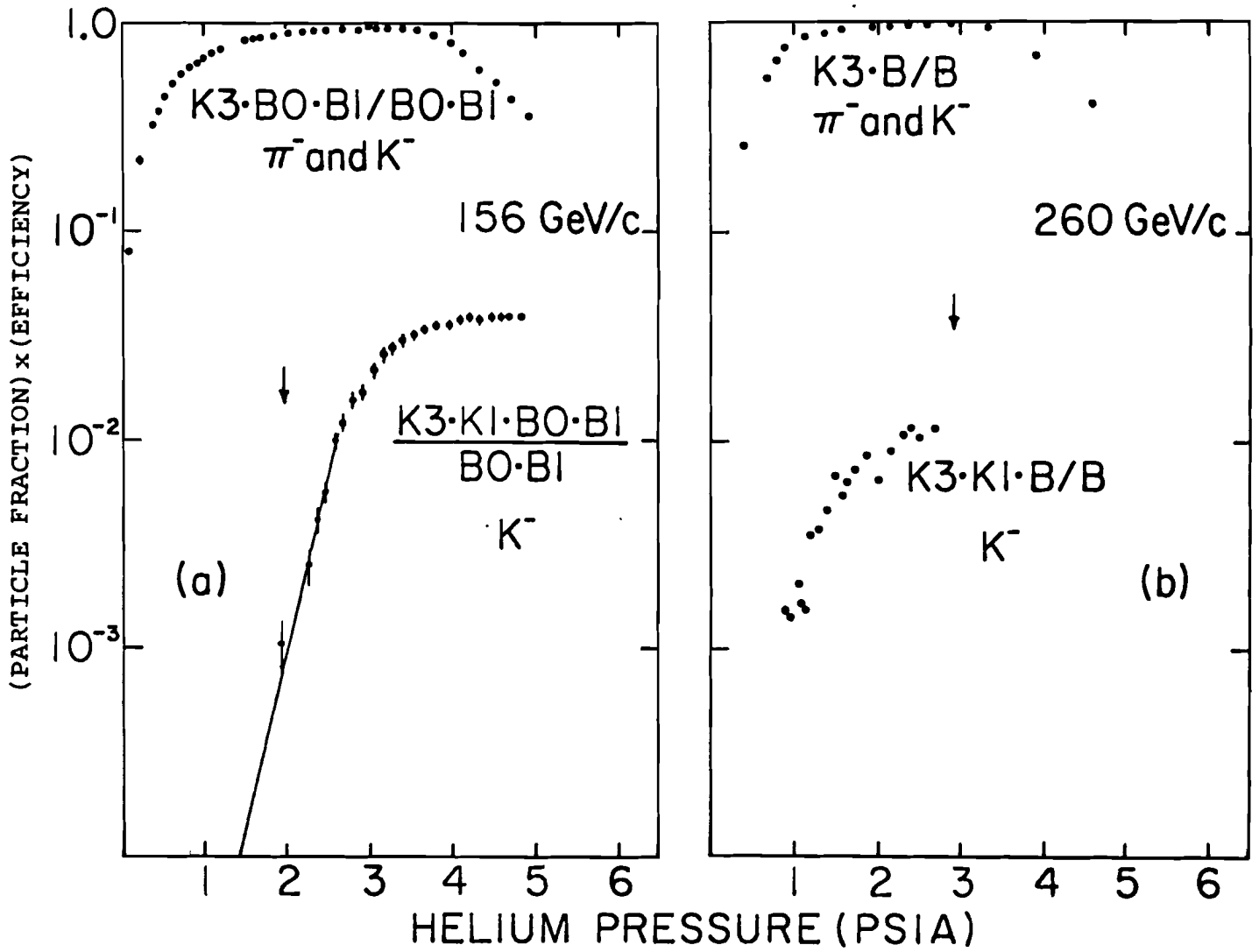
1.0
10^{-1}
10^{-2}
10^{-3}
(PARTICLE FRACTION) x (EFFICIENCY)
K3·BO·BI/BO·BI
π^- and K^-
156 GeV/c
K3·KI·BO·BI / BO·BI
K^-
(a)
K3·B/B
π^- and K^-
260 GeV/c
K3·KI·B/B
K^-
(b)
1 2 3 4 5 6
1 2 3 4 5 6
HELIUM PRESSURE (PSIA)

Figure 8

were used for gating the electronics during the beam spill (see Section E for more detail).

The beam trajectory just upstream of the experimental target was defined by two sets of proportional chambers (J1 and J2 in Fig. 4). Each chamber had two staggered X-planes and two staggered Y-planes, with a wire spacing of 1 mm on each plane, for an effective spacing of 0.5 mm. The angular resolution for the beam track trajectory was ±0.015 mr. Signals from these J chambers were also used in the on-line trigger (see Section E).

C. Drift Chamber System

Trajectories of charged tracks were measured using a system of 24 planes of drift chambers supplemented by four planes of proportional chambers. The drift chambers were arranged in four groups designated D1-D4 as shown previously in Fig. 4.

System D1 contained two X-planes, two Y-planes, and two U-planes in a common gas volume. Looking downstream, the wires in the U-planes were oriented at an angle of +30° to the vertical. The D2 system was identical except that the U-planes were replaced by V-planes, which had wires oriented at -30° to the vertical. To match the aperture of the analyzing magnet, the D1 and D2 systems had active areas of

8 inches vertically by 24 inches horizontally.

Each chamber in the D3 and D4 systems had its own gas volume, and could be moved independently of the other chambers. The D3 chambers had active areas of 18 inches by 44 inches. All planes were identical, with wires running the short distance. Two planes were tilted by +18.5° to the vertical (U-coordinate) and two planes were tilted by -18.5° (V-coordinate). The arrangement of the D4 chambers was identical to that of D3, except that the active areas were 24 inches by 60 inches.

The maximum drift distance in these chambers was 0.4 inches, which, under typical operating conditions, corresponded to a drift time of about 200 nsec. All chambers had the same cell dimensions and were arranged in pairs, with one plane offset by one half of a cell with respect to the other. This was done to help resolve the "left-right" ambiguity; that is, to determine on which side of the sense wire a particular trajectory belonged. Further details concerning the construction and operation of these chambers may be found in Appendix A.

Figure 9 shows a block diagram of the electronics used to record information from the drift chambers. Signals from the sense wires were amplified and shaped by circuits mounted on the drift chambers.[26] ECL-level outputs from these circuits were transmitted via 64-element cables

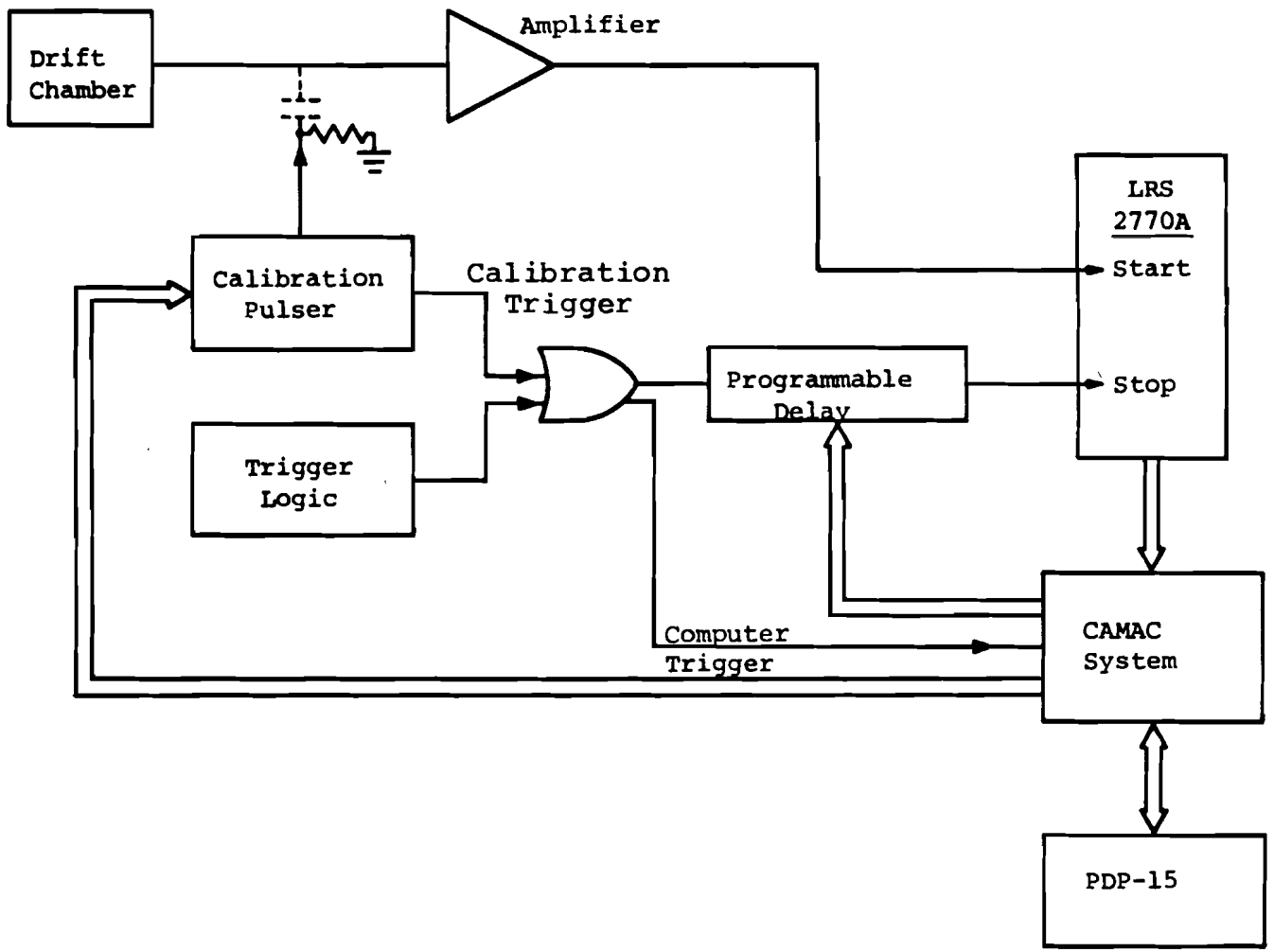
Drift Chamber
Amplifier
LRS 2770A
Start
Stop
Calibration Pulser
Calibration Trigger
Programmable Delay
Trigger Logic
Computer Trigger
CAMAC System
PDP-15

Figure 9

(Ansley C1622-130) to the electronics trailer where they were converted to digital signals via Lecroy Research Systems (LRS) model 2770A Drift Chamber Digitizers. This was one of the first experiments to successfully use a large system of these modules; we will consequently detail our experience with their operation.

Each digitizer contains 96 8-bit time-to-digital converters (TDC) in a triple width CAMAC module.[27] Several time-scale ranges are available. We chose the 500 nsec range to match the 200 nsec drift time of our chambers. This corresponds to about 2 nsec per count or a spatial resolution of about 0.1 mm.

Conversion of the input signals starts at their leading edges and ends at the leading edge of the common stop signal. If a second input start pulse is received before the stop pulse arrives, the clock will be reset; hence, for multiple start pulses, it is the last input signal that gets recorded. Care must be taken to assure that only one stop pulse is received each time after the unit has been cleared. In our system, the common stop pulse was the same as the trigger used to start the computer read-out. The computer cleared the digitizers after reading them out, and then opened a gate to allow the next trigger to be received.

The manufacturer recommended that, due to possible nonlinearities, regions near the ends of the digitizing range not be used for data taking. We therefore set time distributions for real data to fall in the center of the allowed range. This was accomplished, as illustrated in Fig. 9, by using a programmable delay unit which could be adjusted from the console of our on-line computer. This delay could also be varied relative to a standard calibration start pulse, and the resulting data used to calculate an offset and a gain for each channel; using these parameters, digital counts of the TDC's could be converted to times relative to the trigger pulse. During the time between beam spills, the on-line program cycled the delay through four standard values, and then reset the delay to that used for taking data. The calibration events were transmitted to the CDC computer at the central laboratory (see Section G), where a program calculated the offsets and gains by performing a least squares fit to the data. The results of this calibration are presented in Chapter III.

Because the on-line program was not designed to read out all 1000 TDC channels for a single trigger, it was necessary to pulse only a selected subset of amplifier channels for each calibration trigger. Six pulser modules, that could be addressed from the computer, were designed for pulsing the drift-chamber amplifiers.[28] In Fig. 9, one of 16 output lines from a pulser module is shown coupled to an

amplifier channel. Actually, each pulse was coupled to eight amplifier channels via a piece of insulated no. 18 wire placed across the drift-chamber signal lines and terminated through a 50 resistor to the ground plane of the amplifier. A calibration trigger was generated by any pulser addressed from the computer. We ensured that the delays between this trigger signal and each of the 16 output pulses were stable and did not vary by more than one nsec from one channel to another. Trigger signals from all six modules were fanned together to generate a common stop for the TDC's, and a trigger signal for the computer.

The calibration system proved to be extremely valuable for monitoring the performance of the drift chamber electronics. In particular, because the model 2770A digitizers at first had a high failure rate, the calibration scheme enabled us to quickly find and replace faulty channels.

The following additional steps were taken to maintain the digitizers in stable operating condition. Because each unit requires six amps from the +6 volt line, and the standard CAMAC supply can deliver only 25 amps at +6 volts, we decided to place no more than three digitizers in any single CAMAC crate. Even so, we found that the distribution of power through the standard CAMAC pins was inadequate, and we consequently supplied the +6 volt line by means of a

no. 12 wire attached directly to the digitizer unit. The large amount of power consumed within the crates required the installation of additional fans for cooling. Once the above measures had been taken, the system slowly stabilized to the point where the failure rate was less than 1% of all channels per week. The performance of the system throughout the execution of the experiment is described in Chapter III.

The multi-wire-proportional chambers (MWPC's), P1 and P2, were constructed in a manner similar to that used for constructing the drift chambers. Each of the units was composed of two staggered planes, each having 0.1 inch wire spacing, for an effective spacing of 0.05 inch. These chambers were used to measure X-coordinates, which were particularly valuable in providing starting points for track reconstruction. The signals from these chambers were also used to form logic signals for the trigger, to be described in Section E.

Charged-particle momenta were measured with the aid of a BM109 magnet, which has an aperture of 8 inches vertically by 24 inches horizontally, and an effective length of 73.5 inches. We ran this magnet with the current set at 3000 amps, which corresponded to an integrated field length ($\int B d\ell$) of 36.57 kGm or a transverse impulse of 1.098 GeV/c.

D. Liquid Argon Calorimeter

A popular method for measuring energies and positions of photons employs liquid argon ionization calorimeters.[29,30] For coverage of large areas, this type of detector has clear advantages over lead-glass or lead-scintillator systems. It is relatively cheap to build, its response can be made very uniform over large areas, and it is superior in stability to phototube-based systems. Segmentation is also easily implemented using a liquid argon calorimeter (LAC), and the energy and position resolution is comparable to that available using lead-scintillator systems. Our detector was one of the first devices of this kind to be used successfully in an experiment designed to detect high energy photons.

The layout of the basic detector is depicted in Fig. 10. It was composed of alternating layers of 0.080 inch thick lead sheets and 0.063 inch thick copper-clad ($\approx$.001 inch thick Cu) G-10 boards separated by 0.080 inches of liquid argon. The liquid argon served as the ionization medium, and the lead sheets were held at a negative potential ($\approx$1.5 kV) to cause the electrons to drift to the copper-clad boards which were at ground potential. These boards had 1/2 inch wide strips etched on both sides and oriented horizontally or vertically on alternate boards. The vertical strips extended the full lengths of the boards,

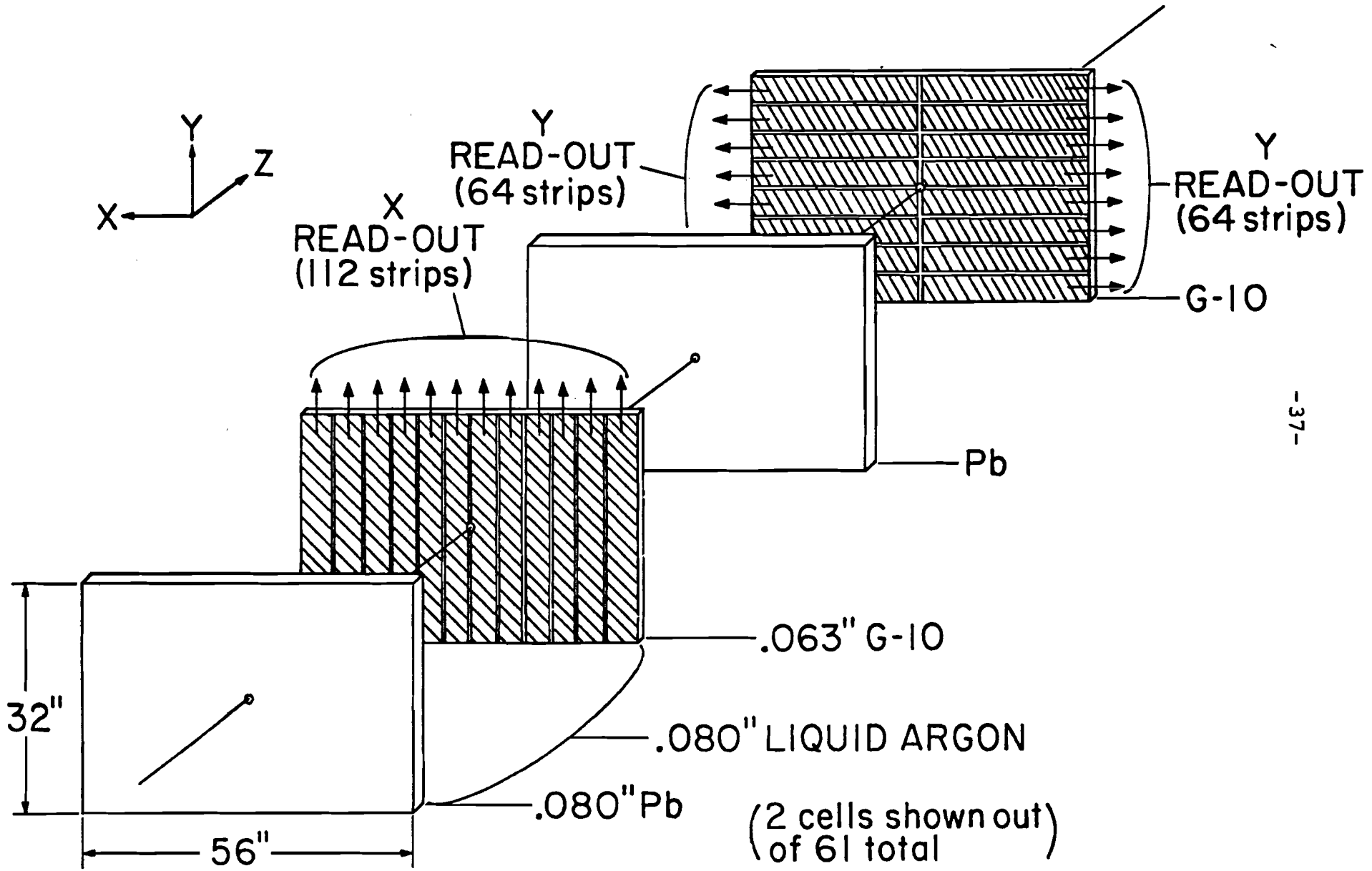
Y
Z
X
Y
READ-OUT
(64 strips)
X
READ-OUT
(112 strips)
Y
READ-OUT
(64 strips)
G-10
Pb
.063" G-10
.080" LIQUID ARGON
.080" Pb
32"
56"
(2 cells shown out
of 61 total)

Figure 10

while the horizontal strips were separated into right and left halves. A total of 61 cells were stacked up to provide a thickness of 24.5 radiation lengths and 1.6 proton-interaction lengths. All strips with the same X or Y position along the Z-axis were connected to a single amplifier, but, with the entire detector divided into front/back and left/right sections. A total of 480 amplifier channels (224 X and 256 Y) were required for this arrangement.

Each element of the detector had a 0.75 inch diameter hole centered on the beam region. This volume was filled with an evacuated quartz tube in order to minimize interactions of beam particles within the detector. The entire detector was suspended from a steel cover and housed in a steel cryostat. The walls of the cryostat and a layer of about one inch of liquid argon in front of the active volume of the LAC contributed about 0.8 radiation lengths of material along the beam direction.

About 3000 liters of liquid argon were required to submerge the detector. Tests showed that the welding-grade argon received from the local vendor had a purity of 1-4 ppm O_2. We employed a paladium catalyst to further purify the argon to a level of $\lesssim 0.1$ ppm O_2. Other studies[30,31] have shown that the presence of oxygen at 10 ppm reduces the collected charge, and therefore the pulse height, by about a factor of two.

Figure 11.a shows a block diagram of the electronics for a single channel in the LAC. A novel method of pulse height analysis,[32] indicated in Fig. 11.b, was applied to the signals from this detector.

The charge sensitive amplifiers, matched to the capacitance of the detector ($\approx$4 nf), are used as integrators with relatively long RC-decay times. The shorter intrinsic risetimes of the input pulses are determined by the drift velocity of electrons in the liquid argon, and correspond to about 250 nsec for our detector. Thus the output from the amplifiers (point ⓐ) appears as the series of steps shown in Fig. 11.b, each step corresponding to an interaction. For the event of interest we sample the level just before the arrival of the pulse, and again just after it has reached its maximum. The difference between these two levels is proportional to the energy deposited in the detector. In principle, the deadtime for this scheme is determined only by the risetime of the incoming pulse. A decay-time constant of about 400 μsec was chosen for most of the amplifiers. However, for strips within two inches of the beam-hole, a shorter time constant of 20 μsec was used to prevent amplifier saturation caused by high interaction rates.

a) Electronics for one channel of LAC

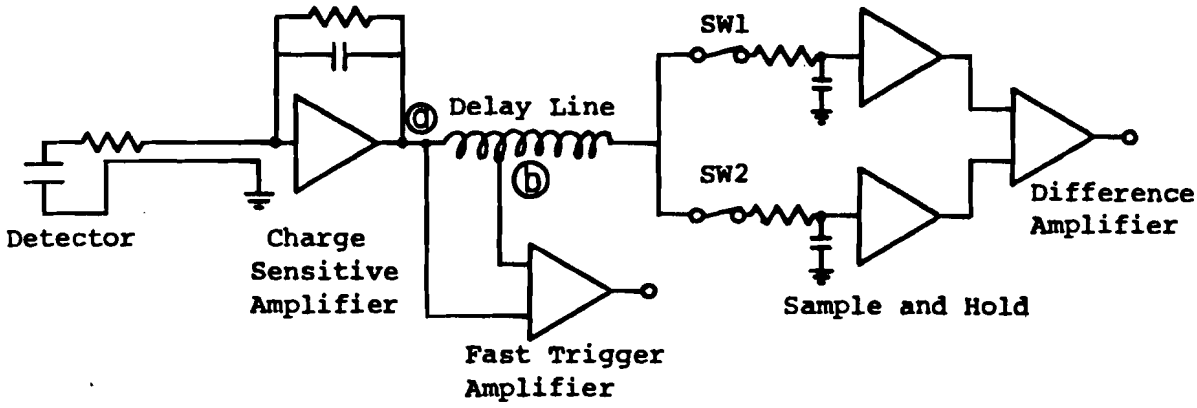

b) Signal at point a

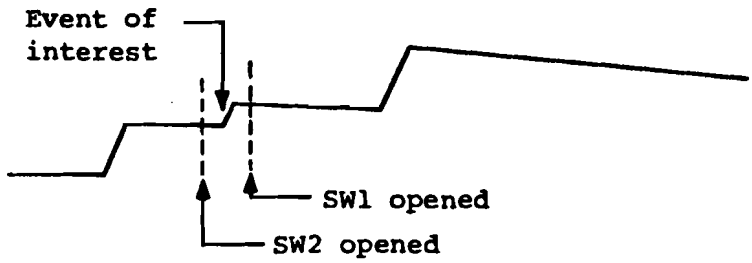

c) Read-out system

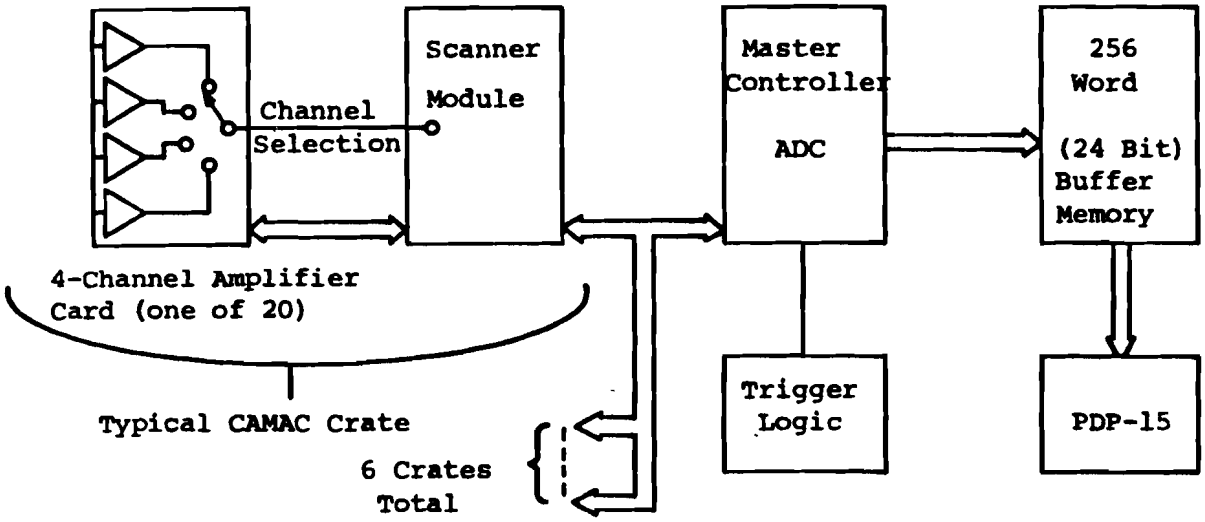

Figure 11

The difference between the signal at point ⓐ and point ⓑ, the latter delayed by about 200 nsec, was used to generate a fast-trigger signal, whose amplitude provided a crude measure of the energy deposited in that strip of the detector. The fast-trigger outputs from all of the Y-strips in the front half of the detector were added together to form a signal proportional to the total energy deposited in the LAC. The use of this signal in defining the event trigger will be discussed in Section E.

As indicated in Fig. 11.c, four amplifiers were placed on a single card, and twenty cards were mounted in a crate along with a scanner module. Six scanners were connected to a master controller which contained a 12-bit ADC. After the trigger was set, the controller cycled through the crates looking for channels that had levels above a preset threshold. When such a channel was found, its level was digitized, and the result transmitted, along with the appropriate channel address, to a CAMAC buffer memory, where this information could be accessed through the on-line computer. The read-out threshold was set typically to correspond to an energy deposition of $\approx$300 MeV per channel.

In parallel with the previously mentioned calibration system for the drift chambers, we implemented a system which continuously tested and calibrated the LAC amplifiers. Two parameters, a pedestal and a gain, must be determined for

each channel of the detector. Between beam spills, the stability of the gains was tested by applying to the inputs of the amplifiers, pulses of known amplitude. In addition, the on-line program automatically set the read-out threshold to zero at selected times between spills, and thereby obtained a measurement of the pedestal level for each amplifier. The results of these tests are presented in Chapter III.

E. The Trigger

The trigger for the experiment was designed to enhance the presence of coherent interactions that had one charged track and more than one photon in the final state. Figure 12 shows a schematic diagram of the counters used in the trigger, and Fig. 13 provides a generalized diagram of the trigger logic used to select these types of events.

The beam count in the vicinity of the target was defined by a coincidence between B2 and B3, where B2 is a 2 in. x 2 in. x 1/16 in. scintillation counter, and B3 is a 1.5 in. x 1.5 in. x 1/16 in. counter (refer to Fig. 12 for the z-coordinates of these counters). The signal from B3 established the reference time, and all coincidences were set such that their timing was determined by the leading edge of the B3 signal. It was particularly important to

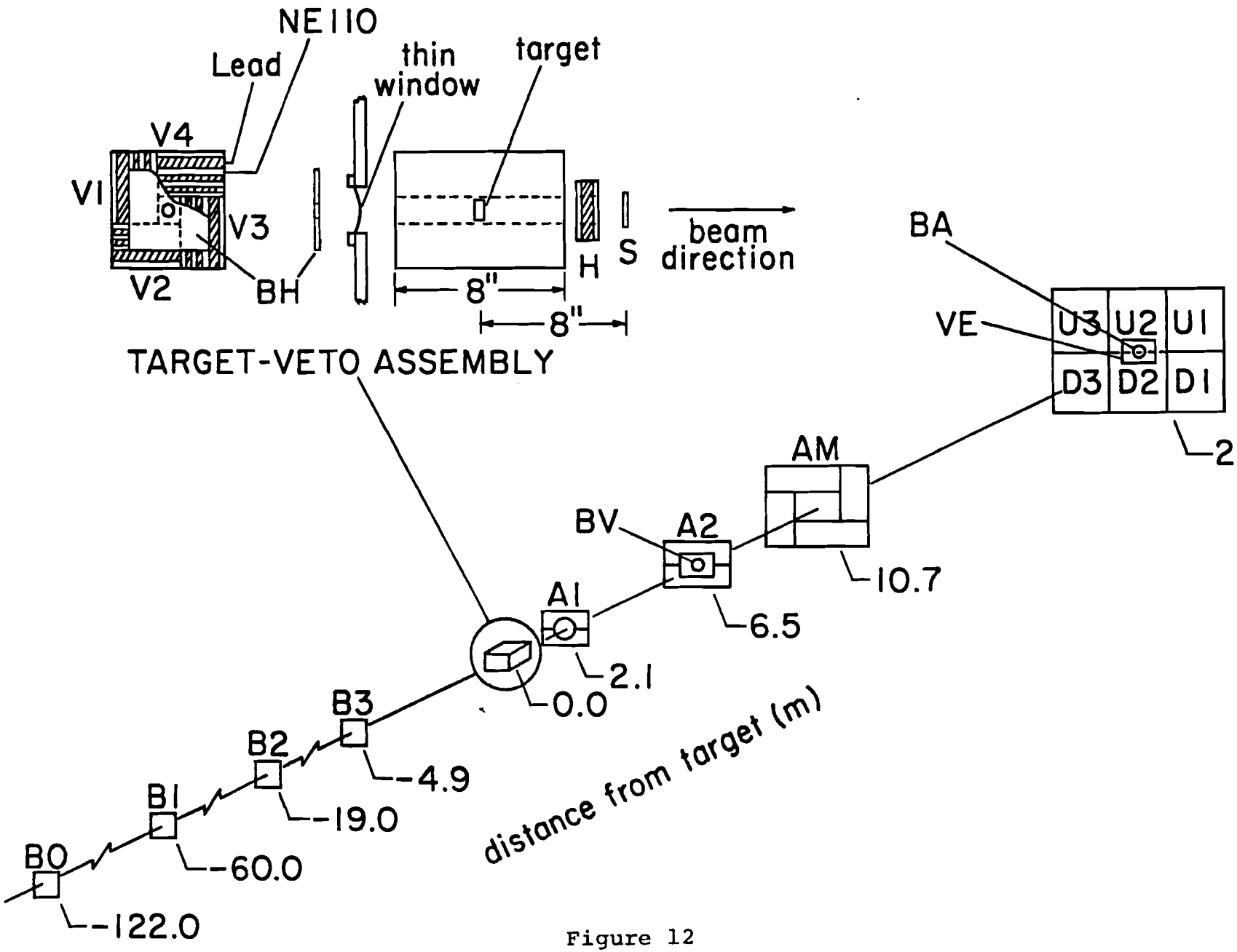
NE110
Lead
thin window
target
V4
V1
V3
V2
BH
H
S
beam direction
8"
8"
TARGET-VETO ASSEMBLY
BA
VE
U3
U2
U1
D3
D2
D1
21.9
AM
10.7
BV
A2
6.5
A1
2.1
0.0
B3
-4.9
B2
-19.0
B1
-60.0
B0
-122.0
distance from target (m)

Figure 12

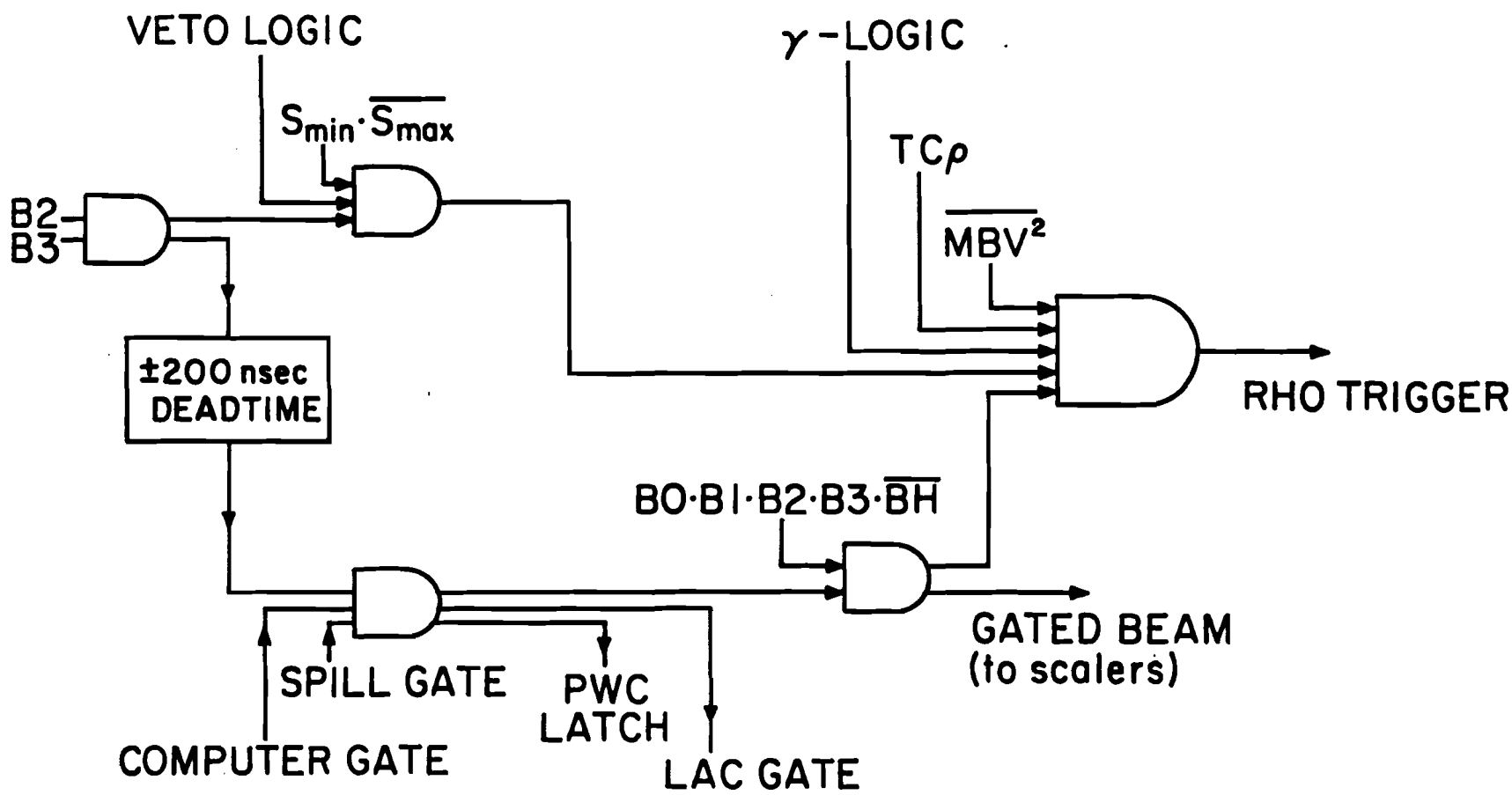
VETO LOGIC
$S_{min} \cdot \overline{S_{max}}$
B2
B3
±200 nsec
DEADTIME
γ-LOGIC
TCρ
$\overline{MBV^2}$
RHO TRIGGER
BO·B1·B2·B3·$\overline{BH}$
GATED BEAM
(to scalers)
SPILL GATE
PWC
LATCH
COMPUTER GATE
LAC GATE

Figure 13

have a stable reference time in the experiment for use as the stop signal for the LRS 2770A units, to determine positions of charged particles passing through the drift chambers.

Our system was capable of handling only one hit per drift wire per trigger, which meant that a second particle that appeared within the 200 nsec drift-time interval could produce hits not associated with the event of interest. To minimize difficulties in reconstruction, beam particles were required to be separated in time by at least 200 nsec. The B2 B3 coincidence was used to form a ±200 nsec deadtime gate centered on the trigger pulse. This requirement contributed about 10% deadtime in the trigger for B2·B3 intensities of $\sim 3 \times 10^5$.

To complete the definition of the incident beam signal, counters B0 and B1, located at either end of the parallel section of the beam, were required to register in coincidence with B2·B3; and, finally, the beam was required to pass through a 5/8 inch diameter hole in the BH counter, located 15 inches upstream of the target. Thus, an acceptable beam particle was defined by the coincidence $B \equiv B0 \cdot B1 \cdot B2 \cdot B3 \cdot \overline{BH}$.

The logic was gated on only during the beam spill and only when the on-line computer was not busy reading out data. Fast logic signals were used to latch proportional-chamber signals and to strobe the logic units of the LAC. The ungated beam signal, B, was put into coincidence with the gated B2•B3 signal to provide a measure of total gated beam, which was used in calculating cross sections.

The inset of Fig. 12 shows the arrangement of counters surrounding the target. For coherent interactions, entire nuclei recoil with typical momenta of less than 100 MeV/c; such momenta are not high enough for the nuclei to leave the target. To enhance triggers from reactions of this type, we used the four V-counters in veto to suppress the majority of the interactions that involve multiparticle production and nuclear excitation. The V-counters consisted of sheets of NE110 scintillator interleaved with lead plates for a total thickness of 5.2 radiation lengths. The H-counter was a sandwich of lead and scintillator with a 1.25 inch diameter hole in the center. The signals from each V-stack and from the H-counter were transmitted via plastic light guides to separate Amperex 56-AVP phototubes. Four nsec shorting clips were used to shape the signals and to provide good two-pulse resolution. Because charged particles passing through the target can generate δ-rays which may veto good triggers, the inner walls of the veto arrangement were lined

with 0.01 inch of copper to absorb low energy δ-rays.

The veto counters, A1, A2, and AM, shown in Fig. 12 defined the geometrical acceptance of the spectrometer, which was basically limited by the aperture of the analyzing magnet. These counters were composed of lead and scintillator layers and viewed by RCA 8575 phototubes, also with 4 nsec shorting clips attached at the outputs. Each counter had a thickness of about six radiation lengths.

Because the targets used in this experiment were typically $\sim$0.03 collision-lengths thick, most of the beam passed through them without interacting. The BA counter, a 1.125 inch diameter and 1/16 inch thick scintillator, placed just in front of the photon detector, was used to veto triggers that had charged particles in the region of the unscattered beam. All of the veto counter signals were combined to form the strobed signal

$$\text{VETO LOGIC}=B2\cdot B3\cdot\overline{BH}\cdot\overline{BA}\cdot\overline{(V1+V2+V3+V4+H)}\cdot\overline{A1}\cdot\overline{A2}\cdot\overline{AM}.$$

The S-counter (1.5 in. x 1.5 in. x 1/16 in.), located eight inches downstream of the target, was used to determine the number of charged particles leaving the target. A minimum discriminator level, S_{min}, and a maximum level, S_{max}, were set to select events that had one charged particle emerging from the target. The pulse height from

the S-counter was digitized for off-line studies of these discriminator settings.

Material downstream of the target (chambers, scintillation counters, etc.) had a total thickness of ≈ 0.04 collision lengths, which is comparable to the thicknesses of the targets we used. Triggers due to interactions in this material could not be easily suppressed by the BA-counter. To eliminate such unwanted events, we formed a matrix between the signals from the beam chambers, J1 and J2, and the proportional chamber, P1, located just downstream of the decay pipe.

Signals from one of the X-planes in each of the J1 and J2 systems, and from the central 1.2 inch region of both planes in the P1 chamber, were brought via RG-58 coaxial cables to the Matrix Beam Veto (MBV). This fast logic unit was used to establish whether the three wires in the three chambers determined a straight line (i.e., an unscattered beam track). As set up, the matrix would be satisfied for outgoing tracks (in P1) that deviated by less than 0.3 mr from the beam track (defined by the J chambers). To prevent vetoing of particles that were scattered at large angles in the vertical plane, a one inch diameter and 1/16 inch thick counter, BV, was placed just downstream of the P1 chamber and put in coincidence with the MBV signal. Thus, the

signal used as part of the event trigger was $\overline{MBV^2} \equiv \overline{MBV \cdot BV}$. The MBV efficiency was found to be about 90%, being limited mainly by the efficiencies of the proportional chambers.

An additional logic signal was formed by using the P1 and P2 chambers to count the number of charged tracks passing through the apparatus. Signals from the two offset planes in each chamber were interleaved to reduce the effective wire spacing by a factor of two. A track was defined by the presence of signals on a continuous group of "adjacent" wires, separated from other groups by at least one blank wire at each end of the group. The signals were analyzed by a multilevel fast preprocesser designed and built at Fermilab;[33] this unit provided logic levels proportional to the number of groups found in the MWPC's, for up to five tracks. The five signals from each of the track counters used in the event trigger, were latched for off-line comparison with the MWPC information; agreement between the two was found at better than the 90% level. The logic signal TC_ρ (see Fig. 13) required one or two tracks from the P1 track counter and one, two, or three tracks from the P2 system. These conservative requirements were implemented because of background due to noise pulses, δ-rays, and, in P2, ambiguities due to large-angle tracks caused by bending of the charged-particle trajectory in the magnet.

A schematic of the logic associated with the photon detector (γ-logic) is shown in Fig. 14. Because charged hadrons that strike the detector can frequently deposit significant amounts of energy, it is not restrictive enough to simply trigger on energy deposition in the LAC. The large cross section for elastic scattering of beam particles and their subsequent interaction in the LAC, posed the most serious problem in triggering.

One way to suppress background due to elastic scattering is to use momentum conservation for decays of the type $\rho^- \rightarrow \pi^- \pi^0$. As discussed in Chapter I, Coulomb production of the ρ^- is essentially along the direction of the beam, so if the π^- travels above the centerline of the apparatus, the π^0 must travel below the centerline, and vice versa. A wall of counters (U1,U2,U3;D1,D2,D3) was set up to cover the active area of the LAC to determine whether a charged particle was above or below the centerline. As mentioned in Section D, fast differential outputs from the LAC amplifiers were fanned together for the upper and lower Y-strips in the front half of the detector and discriminated to form the E_{up} and E_{dn} signals. To provide an acceptable trigger, a signal from E_{up} was required not to be accompanied by charged particle signals in any of the U-counters, and similarly for E_{dn} and the D-counters. In addition, the analog signals, E_{up} and E_{dn} were added to obtain a total energy requirement in the final trigger.

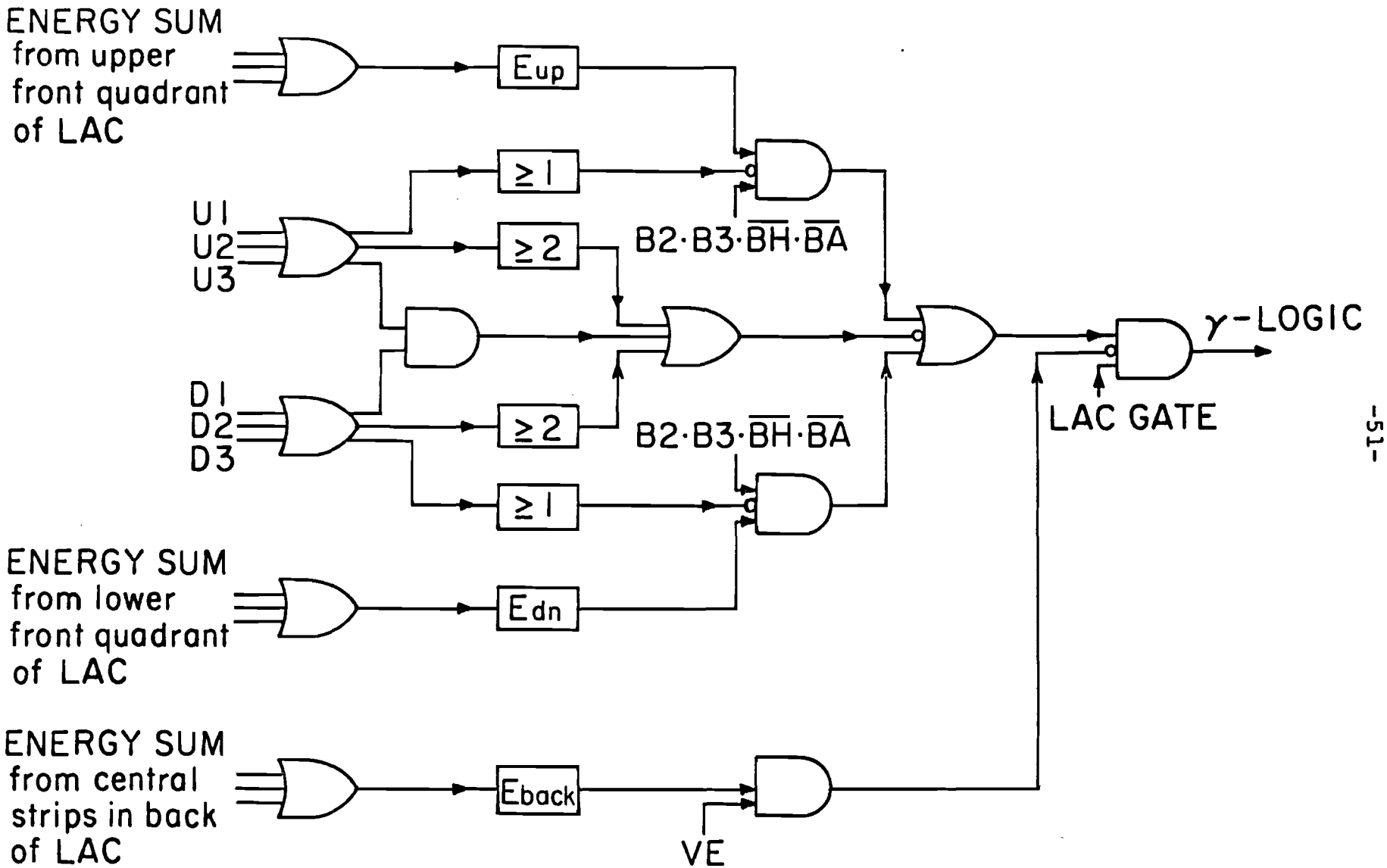
ENERGY SUM
from upper
front quadrant
of LAC
Eup
≥1
U1
U2
U3
≥2
B2·B3·$\overline{BH}$·$\overline{BA}$
D1
D2
D3
≥2
B2·B3·$\overline{BH}$·$\overline{BA}$
≥1
ENERGY SUM
from lower
front quadrant
of LAC
Edn
ENERGY SUM
from central
strips in back
of LAC
Eback
VE
γ-LOGIC
LAC GATE

Figure 14

This correlation between the photon energy and the U/D counters eliminated a large fraction of the background due to elastic scattering. But there remained events for which the charged-particle trajectory was too close to the centerline for this requirement to be effective. To eliminate these triggers, we used the fact that hadronic showers tend to deposit more energy than electromagnetic showers in the back half of the photon detector. Consequently, fast signals from the central X- and Y-strips in the back half of the LAC were added together to give the signal E_{back}. A 1/16 inch thick counter, VE, two inches in the vertical and four inches in the horizontal dimension, was centered on the beam in front of the LAC, and the coincidence $VE \cdot E_{back}$ was used to veto the trigger. This refinement reduced the trigger rate by about a factor of two and caused little loss in good signal.

In summary, the "RHO" trigger was defined as:

$$RHO = B \cdot (\text{VETO LOGIC}) \cdot S_{min} \cdot \overline{S_{max}} \cdot \overline{MBV^2} \cdot TC_{\rho} \cdot (\gamma\text{-LOGIC}).$$

F. Targets

Several kinds of nuclear targets were selected to study the scaling properties of electromagnetic and hadronic production processes. Two different thicknesses of lead and copper were used to check that we were making proper corrections for target-dependent effects such as photon conversion and pion absorption. The thicknesses of the targets used in this experiment are presented in Table I. The target material was machined to dimensions of 2.1 cm x 2.1 cm and glued to a thin lucite holder which was then inserted inside the target-veto assembly (see Fig. 12). The thickness of each target was measured to an accuracy of ± 0.002 cm, and the mass to ± 0.1 g. The thicknesses, in units of g/cm^2, varied in accuracy from 0.33% for target C-1, to 3.7% for the worst case, Pb-4. The thicknesses were chosen mainly to reduce the effect of multiple Coulomb scattering on the resolution. In the worst case, for the Pb-1 target, multiple scattering contributed about 7 MeV/c to the resolution in transverse momentum; this was comparable to the angular resolution of the drift chamber system.

TABLE I. Properties of the Targets

Element	Atomic Number	Atomic Weight	Thickness[a] (cm)	Thickness[a] (gm/cm^2)	Number of radiation lengths	Number of collision lengths[b]	$A/N_o\rho t$ (Barns)
Carbon (C-1)	6	12.01	2.54	4.52 ±0.01	0.106	0.0770	4.41± 0.01
Aluminum (AL-1)	13	26.98	0.952	2.66 ±0.01	0.111	0.0385	16.84± 0.08
Copper (Cu-1)	29	63.54	0.159	1.41 ±0.03	0.110	0.0170	74.83± 1.42
Copper (Cu-2)	29	63.54	0.320	2.84 ±0.04	0.221	0.0342	37.15± .52
Lead (Pb-1)	82	207.19	0.159	1.78 ±0.05	0.280	0.0159	193.3 ± 5.0
Lead (Pb-4)	82	207.19	0.080	.896±0.033	0.141	0.0082	384.0 ±14.2

(a) Area: 2.10 cm × 2.10 cm

Accuracy: thickness - ± 0.002 cm, mass - ± 0.1g.

(b) For nucleons.

G. On-Line Data Acquisition and Monitoring

Whenever the trigger was satisfied, the logic was gated off and appropriate readout signals and gates were set to digitize data for that event. The on-line computer read out information from the CAMAC system, performed some rudimentary analysis, and was used to write data onto magnetic tape for permanent record.

A schematic diagram of the data flow is shown in Fig. 15. Signals from the various detectors entered standard CAMAC modules where they were stored for readout. The system had a total of six CAMAC crates controlled by one branch driver and interfaced to the PDP-15 computer. The PDP-15 then transferred data from these modules to magnetic tape. A PDP-11 computer controlled the transfer of data to the BISON-NET system.

The BISON-NET system[34] was a rather unique feature of this experiment. It allowed us to transmit a portion of our data to the central CDC 6600 computing system where our off-line programs could be used to provide rapid analysis and to monitor details of the equipment.

Monitoring and calibration of the drift chambers and of the LAC system was controlled by the on-line program. As indicated earlier, all drift chamber amplifiers and LAC amplifiers were pulsed between spills and read out for tests

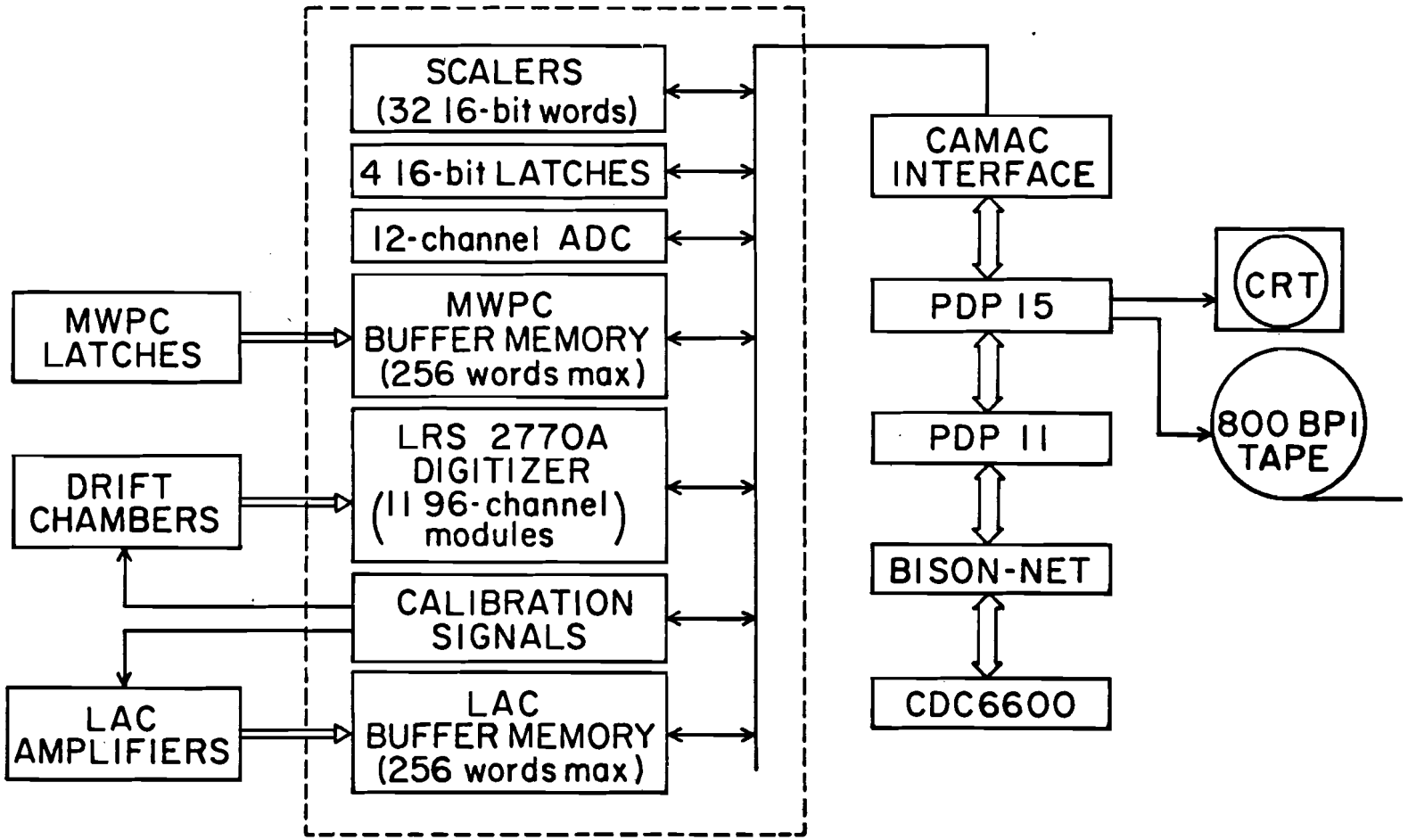
SCALERS
(32 16-bit words)
4 16-bit LATCHES
12-channel ADC
MWPC
BUFFER MEMORY
(256 words max)
LRS 2770A
DIGITIZER
(11 96-channel
modules)
CALIBRATION
SIGNALS
LAC
BUFFER MEMORY
(256 words max)
MWPC
LATCHES
DRIFT
CHAMBERS
LAC
AMPLIFIERS
CAMAC
INTERFACE
PDP 15
PDP 11
BISON-NET
CDC6600
CRT
800 BPI
TAPE

Figure 15

and for calibration purposes. Additional monitoring of equipment performance was provided by the on-line program through displays of such quantities as time distributions from the LRS 2770A units, pulse heights from the LAC amplifiers, and the like.

The data were written onto tape at 800 BPI with a fixed record format of 320 16-bit words. Under stable running conditions, a tape containing ≈30000 triggers could be written in about two hours. The data analyzed in this thesis, consisting of ≈100 tapes, were obtained during June and July of 1978.

Data were recorded concurrently for three different triggers; each trigger was latched and sorted out at the analysis stage. In addition to the "RHO" trigger, which was described in detail above, we took data with an "A1" trigger (requiring three charged tracks out of the target), and with a "V" trigger (requiring one charged track out of the target and a neutral decay to two charged tracks in the vacuum pipe). Data were taken with several nuclear targets (detailed in Section F), and with no target present (for a background subtraction). Several sets of straight-through beam data (with the BM109 magnet off) were taken to aid in aligning the chambers. A special set of data, using 50 GeV/c electrons, was recorded for use in calibrating the LAC. Results of the alignment and calibration are presented in Chapter III.

CHAPTER III

CALIBRATION AND RESOLUTION

A. Introduction

In this chapter we describe the procedures used to calibrate the individual components of our spectrometer, and the resultant resolution achieved for the system. Calibration and alignment of the drift chambers and of the LAC are described in Section B and Section C, respectively. In Section D we present a study of the resolution of the spectrometer based on the two-body decay process $K^- \rightarrow \pi^- \pi^0$.

B. Calibration and Alignment of Drift Chambers

In order to utilize the data recorded by the drift chamber system, we had to determine two different types of calibration constants: (1) parameters describing the electronics, and (2) parameters, such as electron drift velocities and sense wire positions, that depend on the construction of the chambers.[35]

The setup used for calibrating the electronics was described in Chapter II.C. A gain and an offset for each of the 1034 LRS 2770A digitizer channels was calculated from calibration events accumulated just prior to each data run. Figure 16 shows, for one calibration run, a distribution of the sum of the squares of the deviations from a fit of the calibration points to a straight line. The mean deviation is less than one nsec, and because a drift time of one nsec corresponds to about 0.05 mm in space, contributions to the chamber resolution due to errors in calibration of the electronics were deemed negligible.

Although the calibration constants for any run were well determined, variations from run to run were large enough to warrant the use of a separate set of constants for each data run. Figure 17 shows variations of the gain and offset with time for two typical channels in the system.

The next step in the calibration process was the conversion of the drift-time intervals to coordinates in space. This required the determination of the zero point for our time scale, the position of each sense wire relative to a standard coordinate system, and the drift velocity for electrons in the gas.

"Straight-through" tracks, obtained without a target in position and with the BM109 analyzing magnet turned off, were used to align the chambers in the spectrometer. First,

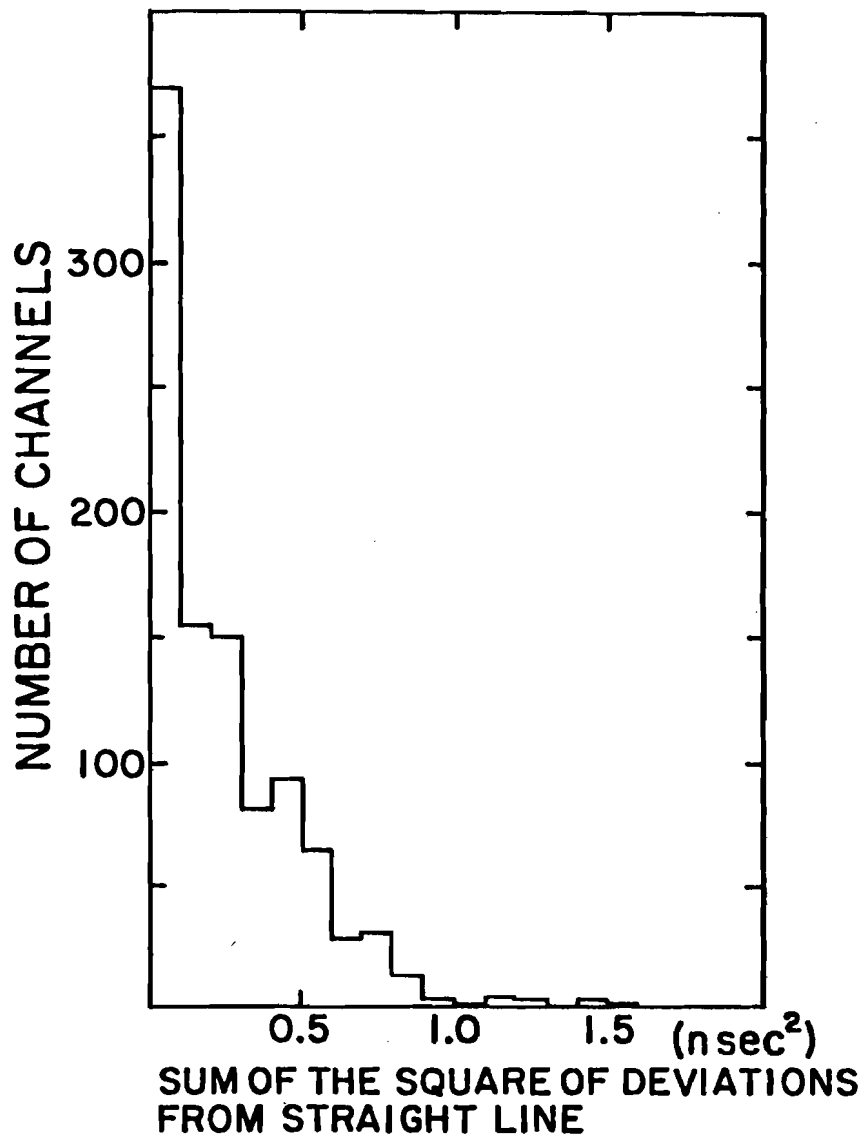
NUMBER OF CHANNELS
300
200
100
0.5
1.0
1.5
(n sec²)
SUM OF THE SQUARE OF DEVIATIONS
FROM STRAIGHT LINE

Figure 16

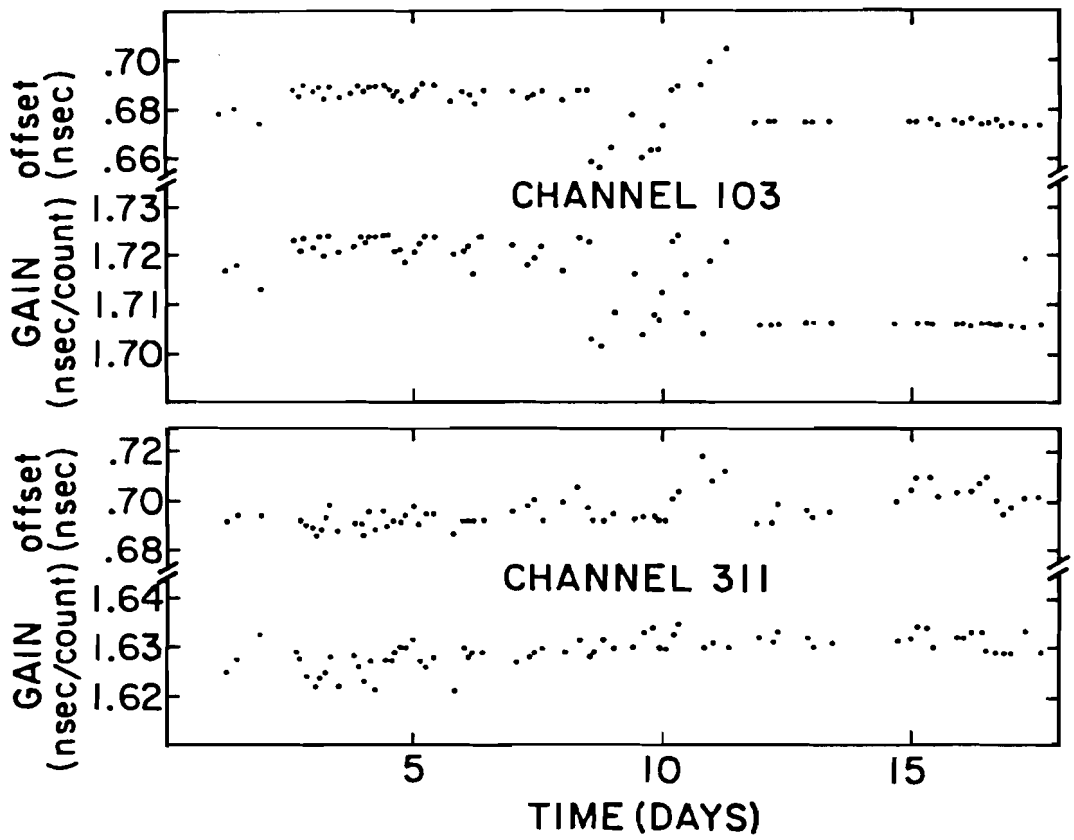
offset (nsec)
.70
.68
.66
GAIN (nsec/count)
1.73
1.72
1.71
1.70
CHANNEL 103
offset (nsec)
.72
.70
.68
GAIN (nsec/count)
1.64
1.63
1.62
CHANNEL 311
5
10
15
TIME (DAYS)

Figure 17

a coordinate system was established by using data from the beam chambers, J1 and J2. It was assumed that all chambers were perpendicular to the beamline and that the wires were oriented at the nominal design angles. Furthermore, it was assumed that the sense-wire spacing was uniform over each plane. Because of these assumptions, only one alignment parameter was required for each plane. The above assumptions were checked for consistency with the data and found to be reliable.

Initial estimates of the drift velocities and time offsets were obtained from the widths and cut-off values of the time distributions. The alignment parameters, time offsets and drift velocities were then varied in an iterative procedure to optimize the resolution of the chambers. In the final stage, the alignment parameters were fixed, and data from several normal RHO-trigger runs were used to determine the time offsets and drift velocities (this was done so as to include data covering a larger area than would normally be covered by the straight-through beam tracks).

The best fits yielded drift velocities of 5.15×10^{-3} cm/nsec for the chambers upstream of the BM109 magnet, and 5.03×10^{-3} cm/nsec for the downstream chambers. This small difference in velocity may be due to the fact that fewer field-shaping wires were used in the downstream

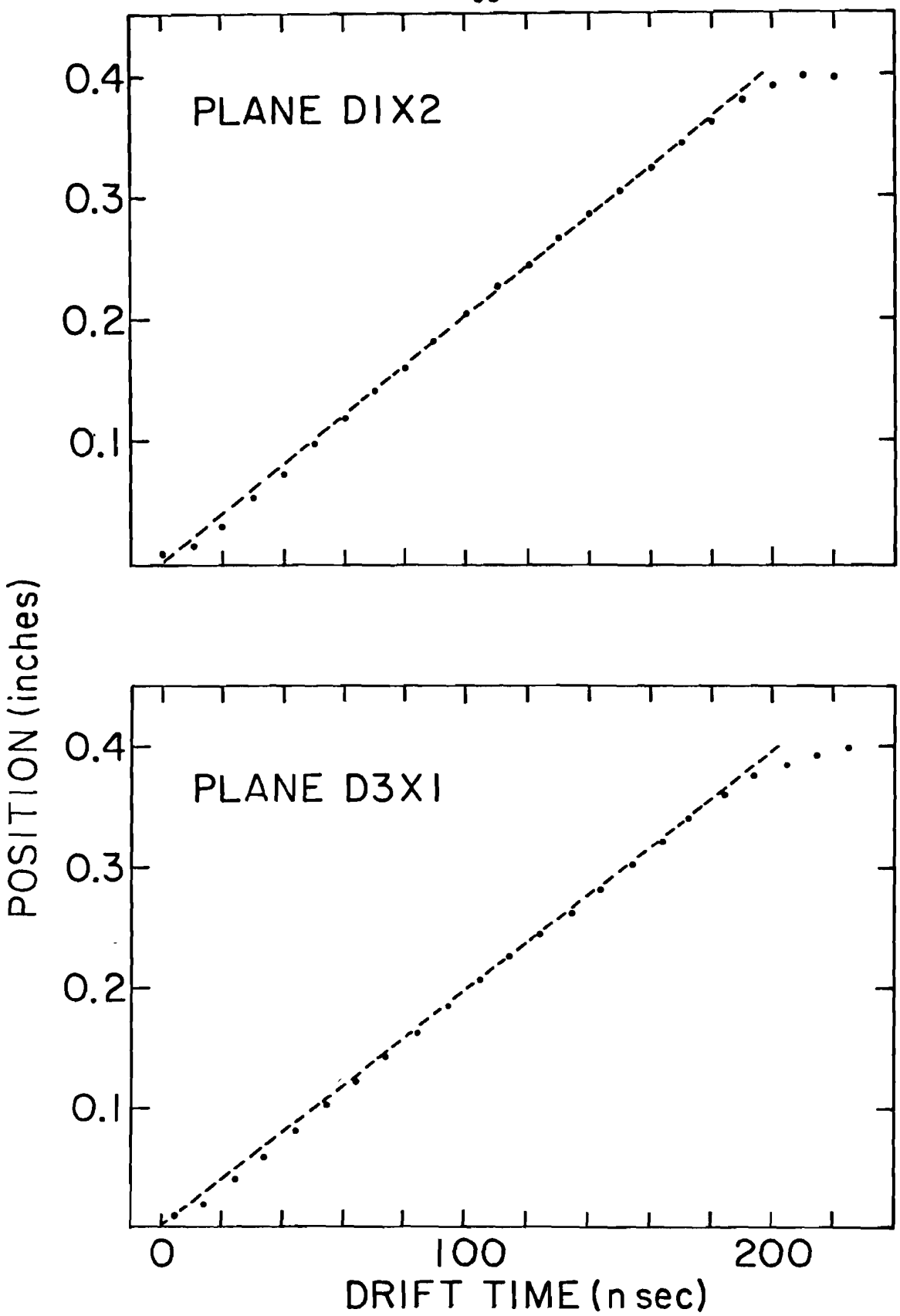
PLANE D1X2
PLANE D3X1
POSITION (inches)
0.4
0.3
0.2
0.1
0
100
200
DRIFT TIME (n sec)

Figure 18

chambers (see Appendix A). Plots of TDC times versus the positions as determined from the beam (J) chambers are shown in Fig. 18 for two drift planes. The dashed lines correspond to results expected for a linear relation based on the drift velocities given above. Except near the edge of the drift cell furthest from the sense wire (position=0.4 inches), deviations from the linear approximation are less than 0.008 inches (0.2 mm).

Using $K^- \rightarrow \pi^- \pi^0$ data, the resolution of the chambers was determined to be σ =0.18 mm (standard deviation per plane) for tracks outside the beam region, and σ =0.26 mm for tracks in the region of the beam (radius $\lesssim$0.3"). This effect can be attributed to an accumulation of space charge, which modifies the electric field in the vicinity of the beam. For most data accumulated using the RHO trigger, the charged tracks were located outside of the beam region; consequently, the deterioration in resolution in the beam region had only minimal effect on the data.

C. Calibration of the Liquid Argon Calorimeter

Just as for the drift chambers, the calibration constants for the LAC can be divided into two categories: (1) those relating strictly to the electronics, and (2) those depending on the construction of the LAC. The method

used for determining the electronic pedestals and gains of the amplifiers was described in Chapter II.D. The other parameters include coefficients for the conversion of digital counts for each of the channels to energies deposited in the corresponding strips of the LAC, and a set of coordinates to align the detector relative to the rest of the spectrometer.

The pedestal and gain measurements were recorded along with the data on magnetic tapes so that they could be used in the reconstruction of the accumulated events. It was found that the electronic gains fluctuated by less than 1% over the course of the experiment, so no corrections were made for them.

Fluctuations in the pedestal levels of the amplifiers were somewhat more problematic. Pedestal levels must, of course, be subtracted before the ADC counts can be converted to energies. The pedestal settings tended to drift during the run, and it was necessary to readjust them periodically. These fluctuations were accounted for by using the calibration constants that were accumulated along with the data.

A variation of pedestals with amplifier rates could have produced serious problems. A test of this possibility was made as follows. The pedestals on several amplifiers were set high enough so that they would be read out for

every event, and the response was studied as a function of beam intensity. This test indicated that pedestals increased by 20 counts (corresponding to ≈ 1.0 GeV of deposited energy) as the rate increased from 0.1 MHz to 1 MHz, but no further increase was observed at higher rates. A correction for this effect was subsequently applied to channels near the beam region, providing a small improvement in the resolution.

In order to determine the absolute value of the gain for each channel, calibration data runs were taken with the beam momentum set at 50 GeV/c and with the pressure in the K1 Cerenkov counter set to identify electrons. At this momentum the beam contained about 10% electrons. The drift chambers and the BM109 magnet were used to determine the momentum of the electrons to compare with the energy measured in the LAC. For a scan of the X-strips the detector was moved horizontally in steps of about two inches across the beam, and the current in the BM109 magnet was varied in order to illuminate the strips uniformly. The detector could not be moved vertically; consequently; for scanning the Y-strips, the beam was deflected up and down, using a dipole magnet (E1PM in Fig. 5).

Applying criteria to eliminate electrons that had emitted a Bremsstrahlung photon, and pions that were misidentified in the Cerenkov counter and subsequentally

interacted in the LAC, left about 150 acceptable events per strip, which were used to minimize the quantity $\sum_i (E_i^* - E_i)^2$. In this expression, E_i^* is the energy based on the drift chamber measurement for the ith event. E_i, the energy measured in the LAC, can be written in the form

$$E_i = \sum_j a_j n_i^j$$

where n_i^j is the digitizer count (corrected for pedestal) for the jth strip of the ith event, and a_j is a linear calibration coefficient for the jth strip. Five strips, centered on the shower maximum, were used to define each energy E_i (using additional strips further from the maximum produced a deterioration in the energy resolution).

The resulting coefficients for the channels in the front half of the LAC are shown in Fig. 19. The larger values obtained for the channels near the center of the detector are due to the shorter integration-time constants used for these amplifiers (see Chapter II.D). Fluctuations in the gain along the length of a strip were found to occur at the 3% level; this was presumably due to nonuniform spacing of the lead plates.

In obtaining the LAC coefficients it was necessary to account for the energy deposited in the back half of the detector. But, because this amount of energy was generally very small and fluctuations in this amount large, it was

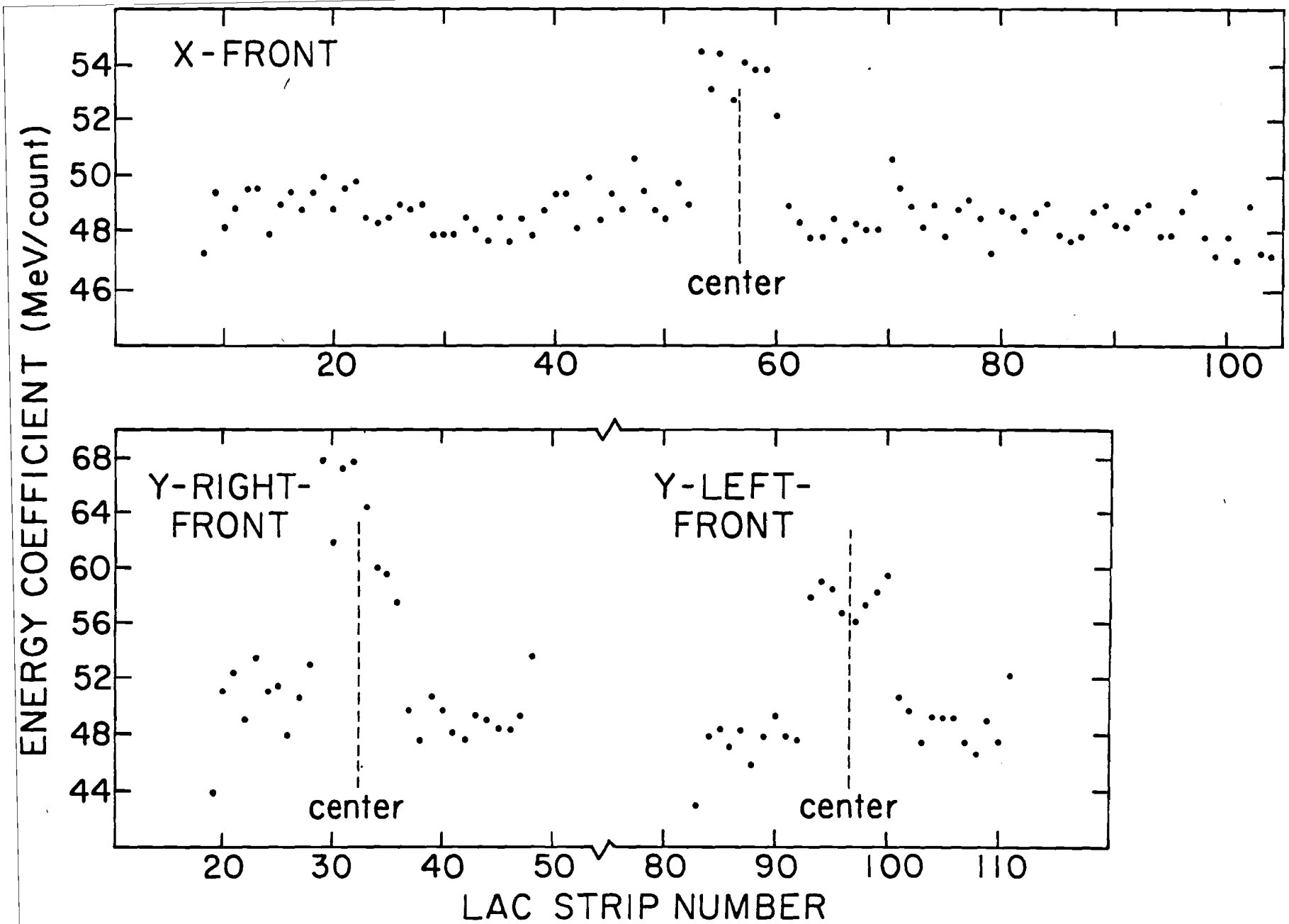
X-FRONT
center
Y-RIGHT-FRONT
center
Y-LEFT-FRONT
center
ENERGY COEFFICIENT (MeV/count)
LAC STRIP NUMBER
54
52
50
48
46
68
64
60
56
52
48
44
20
40
60
80
100
20
30
40
50
80
90
100
110

Figure 19

difficult to obtain unique coefficients for the channels in the back half of the detector. It was therefore decided to use two average coefficients (corresponding to the two types of amplifiers) for these channels. The best results were achieved using average coefficients for the back of the LAC of 38 MeV/count for the standard amplifiers, and 46 MeV/count for the fast amplifiers.

Figure 20 shows the response of the LAC to electrons as a function of their momentum. These data, resulting mainly from Ke3 decays, were accumulated during the normal data runs. The electron momenta were measured using the drift chambers and analyzing magnet. In Fig. 20.a the response of the detector is seen to be linear to better than 5% over the momentum range from 20 GeV/c to 80 GeV/c. The energy resolution of the LAC is indicated in Fig. 20.b. The dashed line corresponds to a resolution of $\sigma_E/E \sim 17\%/\sqrt{E}$. The resolution of our detector at high energies appears to be somewhat worse than expected. This may be due to the fact that, at higher energies, a larger fraction of the energy is deposited in the back half of the detector; as mentioned above, this part was not calibrated as accurately as the front half.

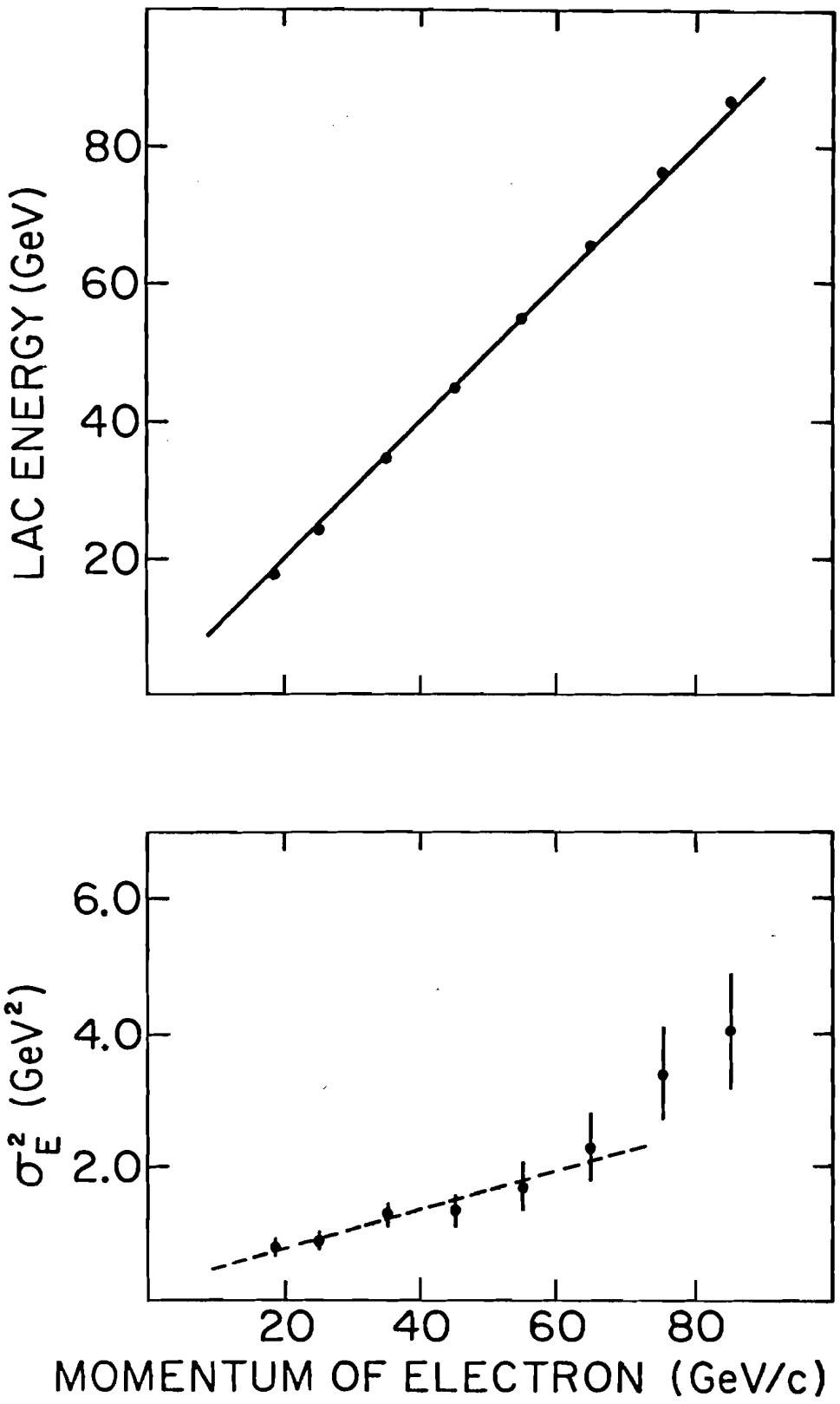
LAC ENERGY (GeV)
80
60
40
20
σ_E^2 (GeV^2)
6.0
4.0
2.0
20
40
60
80
MOMENTUM OF ELECTRON (GeV/c)

Figure 20

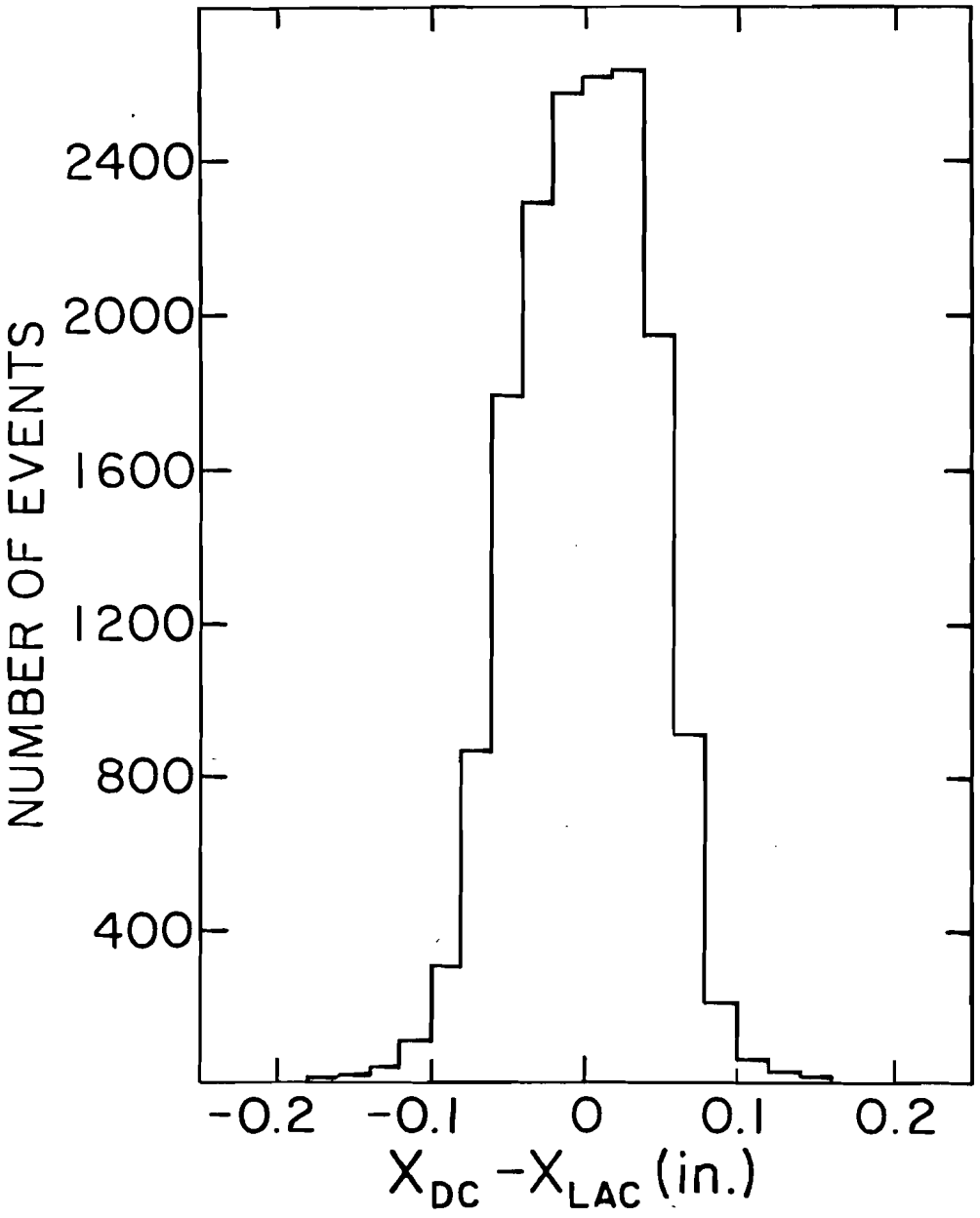
2400
2000
1600
1200
800
400
NUMBER OF EVENTS
-0.2
-0.1
0
0.1
0.2
$X_{DC} - X_{LAC}$ (in.)

Figure 21

Electron data were used for aligning the LAC with respect to the rest of the spectrometer, as well as to measure the position resolution of the LAC. Figure 21 shows a distribution for the difference between the position of an electron, as calculated in the LAC (X_{LAC}), and as predicted by the drift chambers (X_{DC}). The centroid of the energy distribution of the electron shower defines the position as measured by the LAC. The algorithm employed in this determination is described in Chapter IV.C. Assuming the drift-chamber resolution to be $\approx \pm 0.2$ mm per plane, the data in Fig. 21 indicate a spatial resolution for the LAC of $\lesssim 1$ mm (standard deviations per projected coordinate).

D. Resolution as Indicated by K-Decays

The resolution of the spectrometer can best be determined from studies of properties of well known processes such as kaon decays. In particular, the decay $K^- \rightarrow \pi^- \pi^0$ is ideal for comparing with the decay $\rho^- \rightarrow \pi^- \pi^0$. Cerenkov counters were used to identify the incident kaon, and, as a result, the K-decays that reconstructed within the decay pipe constituted a set of unambiguous events that could be used for studying the resolution and acceptance of the spectrometer, as well as the efficiency of the reconstruction program. (Acceptance and efficiency will be discussed in Chapter V.)

A Monte Carlo program was used to generate kinematic variables for processes of interest (e.g. $K^- \to \pi^- \pi^0$ or $\rho^- \to \pi^- \pi^0$). The generated values were then smeared out to simulate the resolution of the spectrometer. Using the measured angular resolution of the drift chamber system (± 0.04 mr), Gaussian errors were imposed on charged-track trajectories. The measured energy and position resolutions for the LAC (see Section C) were used in generating smeared energies and positions of photons. In addition, multiple Coulomb scattering of charged tracks passing through the target was accounted for using the Gaussian approximation for this effect given in the Particle Data Tables.[36]

Two-photon mass spectra are shown in Fig. 22 for 156 GeV/c and 260 GeV/c data. The selected events had two photons which each reconstructed to an energy, $E_\gamma > 10$ GeV, and a decay vertex occuring between the limits 25 inches and 125 inches downstream of the target. Unless otherwise indicated, these two restrictions will be applied to all K-decay events. (The decay vertex distribution will be discussed in Chapter V. No significant variation in resolution was found over the length of the decay pipe.) For further definition of the K-decay yields, the two-photon mass ($M_{\gamma\gamma}$) was restricted to limits indicated by the arrows in Fig. 22. The smooth curves are predictions (normalized to the number of events between the arrows) of the Monte Carlo model. From these plots, the two-photon mass

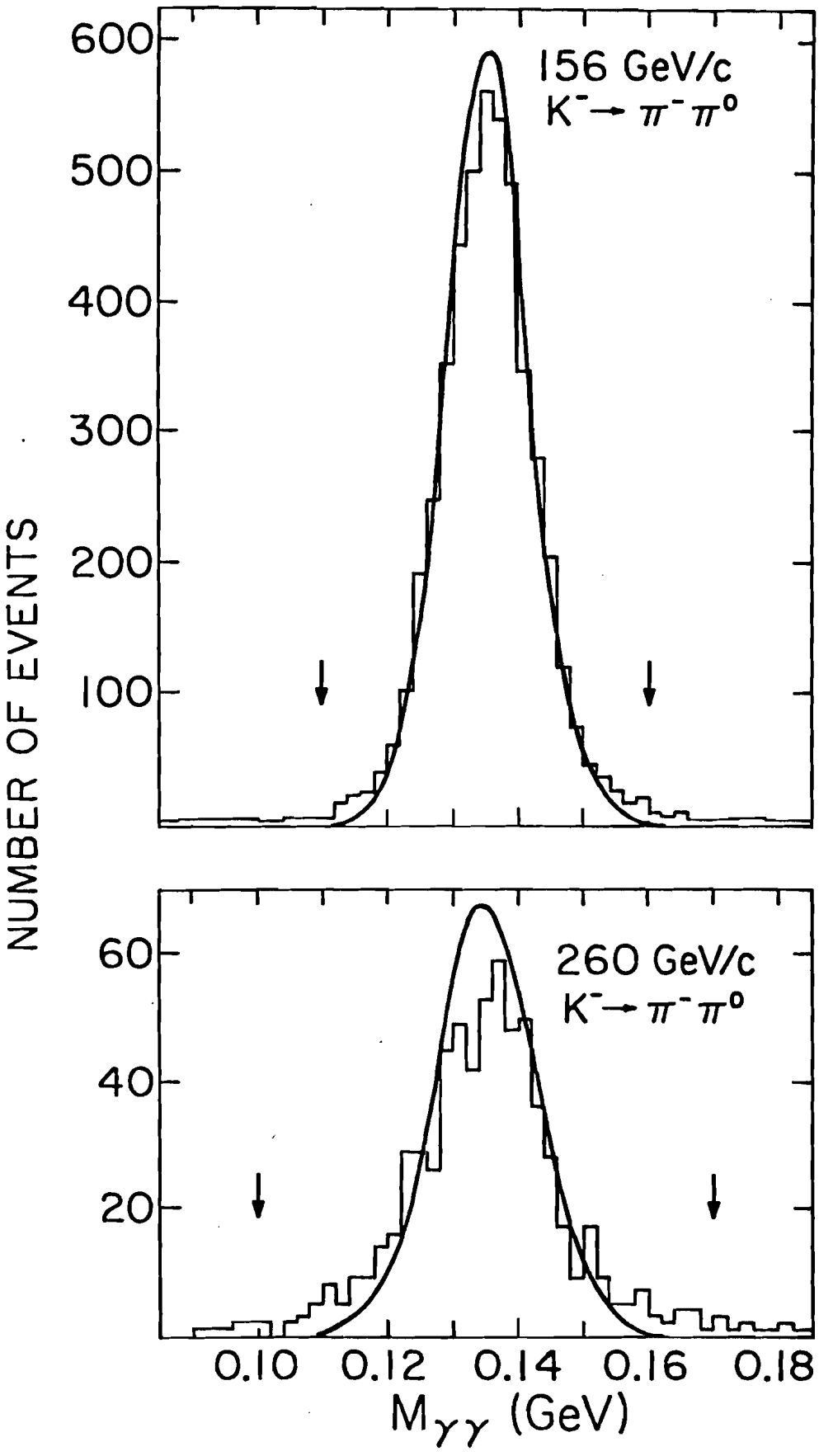
600
500
400
300
200
100
156 GeV/c
K⁻→ π⁻π⁰
NUMBER OF EVENTS
60
40
20
260 GeV/c
K⁻→ π⁻π⁰
0.10
0.12
0.14
0.16
0.18
Mγγ (GeV)

Figure 22

resolution is seen to be 7 MeV (standard deviation) at 156 GeV/c, and 9 MeV at 260 GeV/c.

Figure 23 shows the total summed energy of the π^- and two photons for those events between the arrows of Fig. 22. When additional restrictions are placed on the mass of the $\pi^-\pi^0$ system (0.46 GeV$< M_{\pi^-\pi^0} <$ 0.54 GeV at 156 GeV/c, and 0.45 GeV$< M_{\pi^-\pi^0} <$ 0.55 GeV at 260 GeV/c) and on the square of the momentum transfer ($t <$ 0.002 GeV^2), the events in the shaded regions are removed from the data samples (see Figs. 24 and 25 for a depiction of these cuts). The events with low total energies are predominately due to Kℓ3 decays with missing low-energy neutrinos. To eliminate such backgrounds, events in the $K^- \to \pi^-\pi^0$ signal were defined to have a restricted total energy ($E_{\pi^-\pi^0}$) as indicated by the arrows in Fig. 23. The smooth curves are the Monte Carlo predictions normalized to the number of events in the unshaded regions. The momentum spread of the beam was $\lesssim$1%, hence, the widths of these distributions are determined by the resolution of the spectrometer.

A comparison of the t-resolution for the $K^- \to \pi^-\pi^0$ signal for different targets and different beam momenta is presented in Fig. 24. Again, the smooth curves are the Monte Carlo predictions. (If the resolution of the spectrometer were perfect, we would expect all K-decays to occur at t=0.)

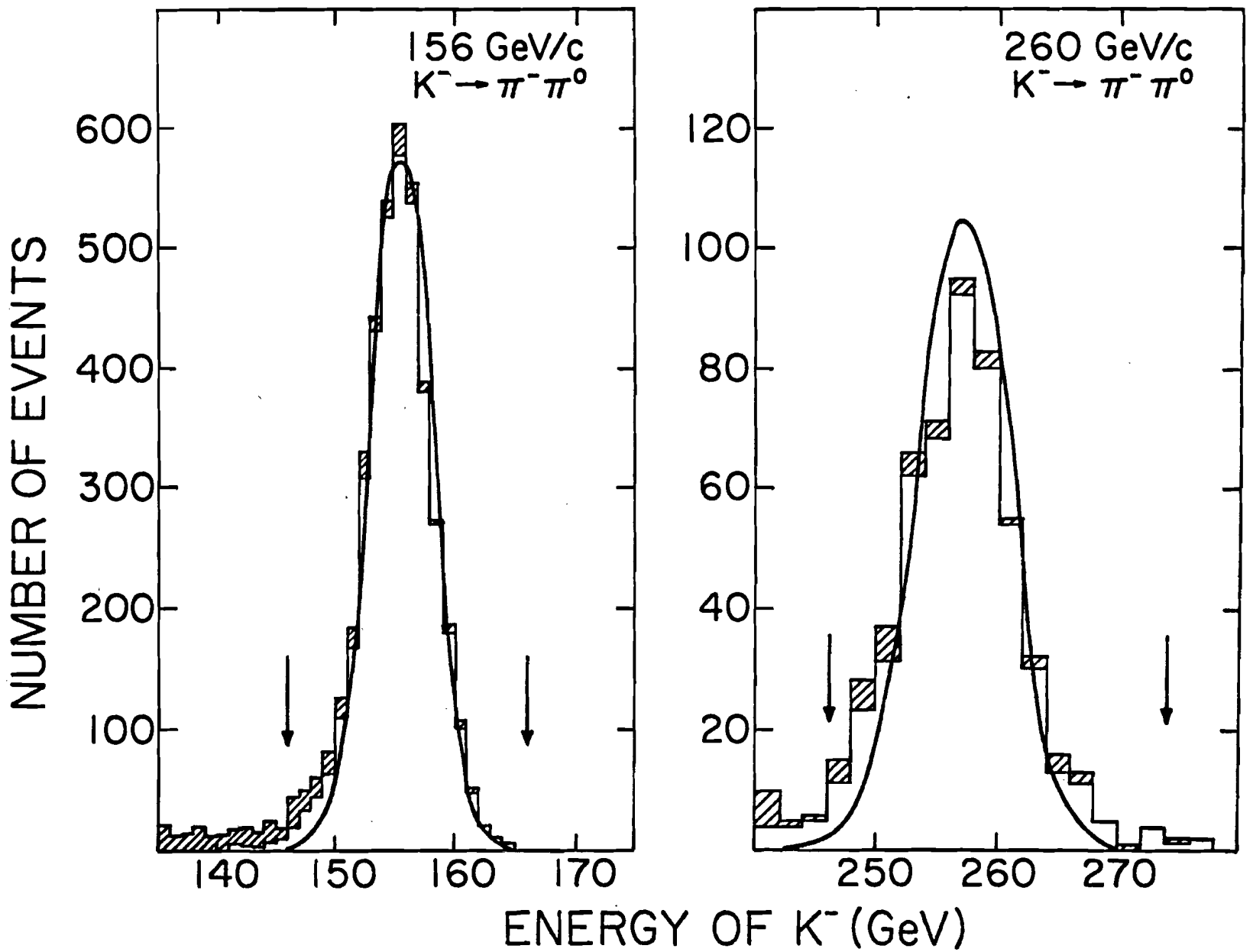
156 GeV/c
K⁻ → π⁻π⁰
260 GeV/c
K⁻ → π⁻π⁰
NUMBER OF EVENTS
600
500
400
300
200
100
120
100
80
60
40
20
140
150
160
170
250
260
270
ENERGY OF K⁻ (GeV)

Figure 23

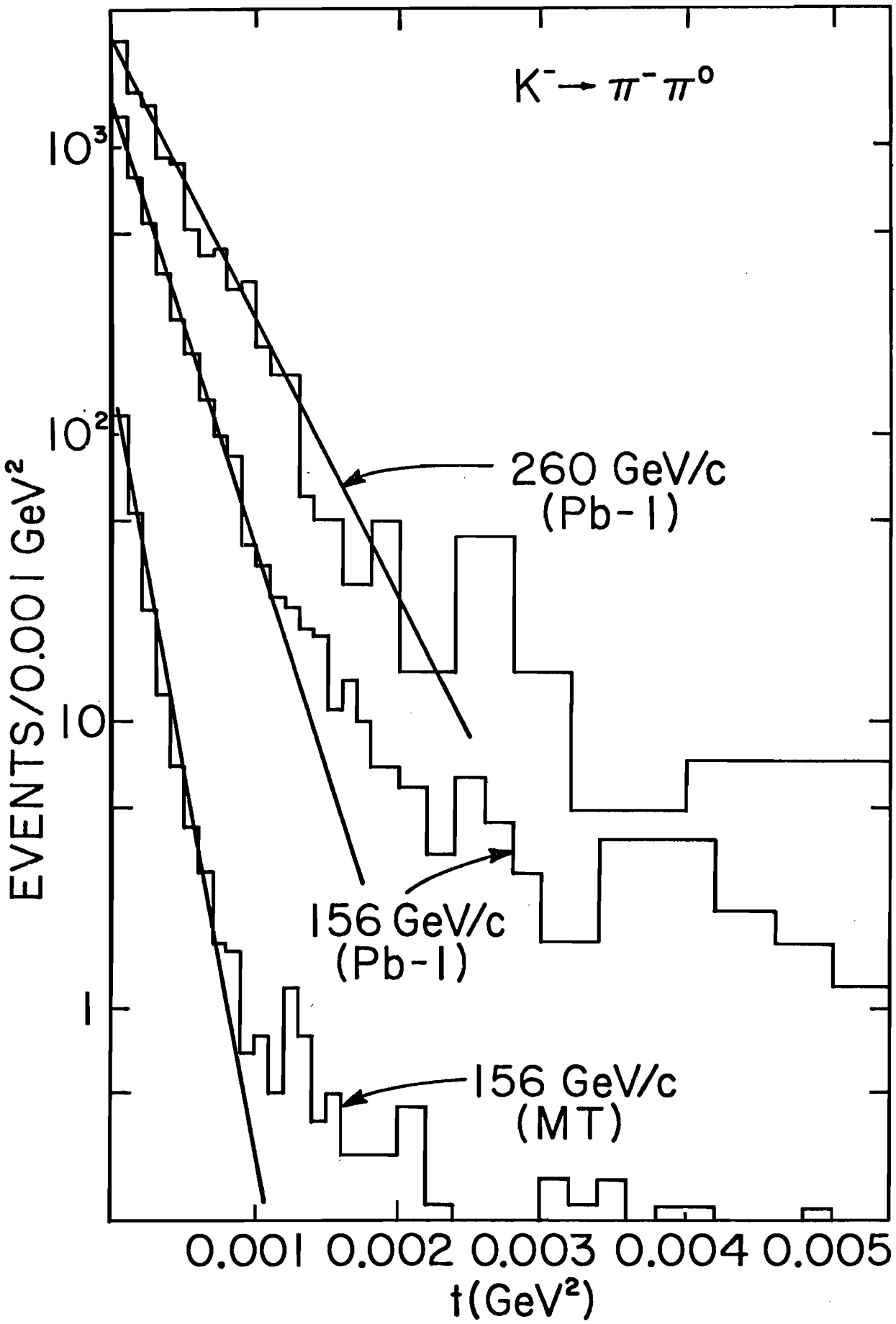
$K^- \rightarrow \pi^- \pi^0$
10^3
10^2
10
1
EVENTS/0.001 GeV^2
260 GeV/c
(Pb-1)
156 GeV/c
(Pb-1)
156 GeV/c
(MT)
0.001 0.002 0.003 0.004 0.005
t(GeV^2)

Figure 24

The effect of multiple Coulomb scattering is clearly observed in Fig. 24 and agrees well with expectations. There is an excess of events, relative to the Monte Carlo predictions, at larger values of t. This excess is partially due to $K\ell 3$ decays which were not eliminated by the cut on $E_{\pi^-\pi^0}$. Another possibility for this excess is due to deterioration in the resolution when the charged track is in the region of the beam (see Section B of this chapter); this effect and, in general, non-Gaussian errors were not included in the Monte Carlo.

Another variable that is quite sensitive to the resolution is the $\pi^-\pi^0$ mass ($M_{\pi^-\pi^0}$). Distributions of the $\pi^-\pi^0$ mass are shown in Fig. 25 for events satisfying the previously mentioned restrictions on $M_{\gamma\gamma}$ and $E_{\pi^-\pi^0}$; in addition, in this figure, we required $t < 0.001$ GeV^2. Once more, the smooth curves are the Monte Carlo predictions, normalized to the total number of events in the distributions. The $\pi^-\pi^0$ mass resolution is 10 MeV at 156 GeV/c and 12 MeV at 260 GeV/c. The $K^- \to \pi^-\pi^0$ signal was defined using the mass limits indicated by the arrows in these plots.

Recalling the remarks made in Chapter II.A, we see that the resolution is more than adequate for making a precise measurement of $\Gamma(\rho^- \to \pi^-\gamma)$.

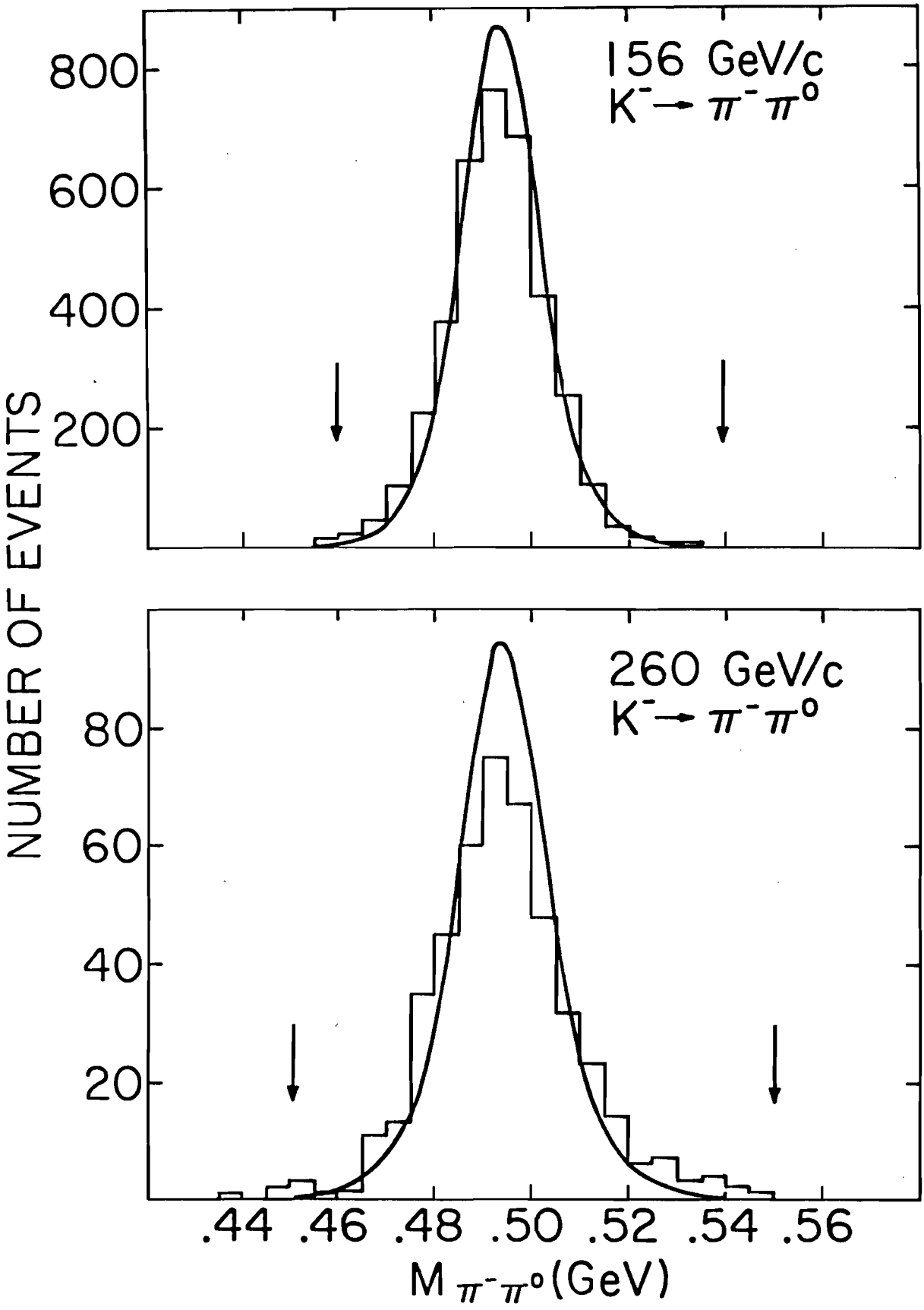
156 GeV/c
K⁻→ π⁻π⁰
800
600
400
200
NUMBER OF EVENTS
260 GeV/c
K⁻→ π⁻π⁰
80
60
40
20
.44 .46 .48 .50 .52 .54 .56
M π⁻π⁰(GeV)

Figure 25

CHAPTER IV

DATA REDUCTION

A. Introduction

Preliminary off-line analysis was performed using the Fermilab CDC 6600 computer system. However, the bulk of the data was analyzed using the new CDC CYBER-175 system at Fermilab. In addition, Fermilab's DEC PDP-10 was used for making graphic displays of individual events. Because the amount of data collected during this experiment was quite large ($\sim 2 \times 10^6$ events), it was important to establish standard procedures for performing the analysis.

The first step was to assure that a complete set of chamber and LAC calibration constants was available for each data run. The events from each data tape (written on-line at 800 BPI) were reconstructed (the same version of the reconstruction program was used for analyzing all events), and the resulting information was written onto a "summary tape" (with a density of 6250 BPI). The summary tape contained a copy of the input data, and the information

generated by the reconstruction program. This information included trajectories and momenta of the charged tracks, energies and positions of the photons, and diagnostics that provided a check of the performance of the apparatus and of the reconstruction program.

As pointed out in Chapter II.G, three triggers were simultaneously accepted during this experiment. Data from all triggers were stored on the same summary tapes. Subsequently, events from several summary tapes (corresponding to a single target material), were sorted according to trigger type, and condensed onto a single "super-summary tape". These super-summary tapes were then used for kinematic analysis.

The reconstruction program was divided into two independent parts: (1) charged-track reconstruction, and (2) photon reconstruction. These programs, along with the diagnostics used to monitor the quality of the data, will be described in the following sections.

B. Charged-Track Reconstruction

Using the calibration constants described in the previous chapter, digital data from the drift and proportional chambers were first converted to spatial coordinates. Because of the left-right ambiguity, each hit

in a drift chamber provided two possible coordinates for a particle's trajectory. Although in the reconstruction process both coordinates were treated on an equal footing, only one was allowed to contribute to the definition of a reconstructed track.

The magnetic field of the BM109 analyzing magnet deflected charged particles horizontally. Because the field was very uniform, the trajectory of a charged particle passing through the spectrometer could be approximated by two straight line segments that intersected at the center of the magnet.

Using the hits from the P2, D3, and D4 chambers, the reconstruction program initiated a search for track segments downstream of the magnet. The X and U projections were used to predict locations of hits in the V projection. Upon finding such a predicted hit, fits to straight lines were performed using those sets of hits for which at least one plane in each doublet (pair of staggered planes) had a hit. All possible combinations for which all hits were within 0.045 inches of the fitted line segment were considered, and the fit with the best χ^2 was chosen as the initial downstream track segment.

Next, a crude definition of the upstream track segment was made as follows. The constraint that the upstream and downstream segments of a track intersect at the center of

the magnet gave one starting point for the upstream segment. Another point was obtained from the hits found in the P1 proportional chamber; also, because tracks do not deviate in the vertical plane, the slope of the trajectory along the vertical projection could be extrapolated upstream.

The upstream and downstream segments were then combined to form a five-parameter description of the track trajectory. The parameters used were: the X and Y coordinates at the center of the magnet, the vertical slope of the track, and the horizontal slopes upstream and downstream of the magnet. All hits (including ambiguities) which fell within a 0.15 inch radius of this initial track hypothesis were considered in the next stage of fitting. Prior to performing this fit, a weight (w_i) was calculated for each hit according to the distance ($x_i - x_0$) between the hit and the track hypothesis:

$$w_i = \exp\left[-\frac{(x_i - x_0)^2}{2\sigma^2}\right] .$$

Initially, the procedure used a standard deviation $\sigma = 0.25$ inches for this weight function; the fit was iterated to obtain new parameterizations of the track hypothesis, reducing σ by a factor of 3/4 each time.

After this process converged, left-right ambiguities were resolved by eliminating the hit (from each pair) which had the smaller weight. The radius of the search volume

around the track was then reduced from 0.15 in. to 0.045 in., and a final fit was performed using all hits (now with equal w_i's) which fell within this volume.

In a separate routine, the program used the hits from the beam chambers, J1 and J2, to calculate the trajectory of the beam track. The vertex for the interaction was defined by the point of closest approach between the trajectories of the beam and the outgoing charged track.

The combined efficiency for reconstructing the K^- beam track and the π^- track from $K^- \rightarrow \pi^- \pi^0$ events was found to be $\approx$95%; about 1% of the loss was due to inefficiency in the beam chambers and the rest due to the conservative pattern-recognition algorithms employed for finding trajectories downstream of the magnet.

C. Photon Reconstruction

Photon energies and positions were calculated from the pulses recorded by the liquid argon calorimeter. Applying the LAC calibration constants described in the previous chapter, the reconstruction program converted the digital signals for all strips of the detector to energies deposited along those strips.

During the initial stages of photon reconstruction, the X and Y projections of the LAC were treated independently. The reconstruction program first searched for "groups" of active strips in each projection in the front half of the detector. Each peak within a group was then separated from other peaks in that group to define a "gamma". Pulse heights from the three strips centered on a peak were used to calculate the energy and position of the "gamma" in the following manner. For pulse heights denoted as P1, P2, P3 (with P2 being the largest), the energy of the "gamma" was defined by $E=b(a(P1+P3)+P2)$, where a and b are constants which were determined empirically using the electron-calibration data. The position of the "gamma" relative to the center of the P2 strip was given by $x=\pm\left[C1\pm(C2+C3/A^2)^{1/2}\right]$, where $A=|P3-P1|/P2 - C4$, and C1, C2, C3, and C4 are constants determined, once again, using electron calibration data.

Certain minimum requirements were imposed on the found "gammas". Those "gammas" with less than a minimum cutoff energy (2.5 GeV per projected view), and those with too much energy in the back half of the detector ($E_{back}/E_{front} > 0.67$) were eliminated from further consideration. The requirement on the back to front energy ratio was imposed so as to eliminate interacting hadrons; these deposit a far larger fraction of their energy in the back of the LAC than photons deposit. In fact, $<1\%$ of all photons from $K^- \rightarrow \pi^- \pi^0$ decays

at 156 GeV/c deposit more than half their energy in the back of the LAC.

The next step was to correlate the "gammas" found in either projection, and thereby determine the parameters of the corresponding photons. Because the detector was finely segmented along the Z-direction and the read-out planes alternated between X and Y, a photon striking the detector should have deposited an equal amount of energy in each projection. Consequently, a photon was defined whenever the energies, E_X and E_Y, of a "gamma" from each projection agreed within a tolerance given by

$$\frac{|E_X - E_Y|}{\left[E_X + 0.5 + 0.03\,E_X^2\right]^{1/2}} < 0.5$$

This criterion was based on an empirical fit to the electron-calibration data.

This correlation procedure worked very well for events in which the "gammas" were well separated in both projections, but many events of interest contained photons that overlapped to some extent in at least one view. For cases in which the summed energy of two "gammas" in one view agreed with the energy of a single "gamma" in the other view, an attempt was made to split the single "gamma" into two "gammas" that would correlate with the two distinct "gammas" in the other view.

After all allowed correlations had been made, the energies from the two projections and from the corresponding strips in the back half of the detector were added together to define the total energy of each photon. The photon position was determined only from the projections in the front half of the detector. Before this information was written onto the summary tape, the photon positions were compared with the projected position of the charged track, and those photons that matched up with the charged track (within 0.75 inch) were flagged as possible electrons or interacting hadrons.

Studies of $K^- \rightarrow \pi^- \pi^0$ events, to be presented in the next chapter, showed that the efficiency for π^0-reconstruction for energies between 20 GeV and 140 GeV was about 80%.

D. Checks for Run to Run Consistency

In order to ensure that the apparatus worked in a consistent manner throughout the experiment, various quantities were examined for every run. Among these were chamber efficiency, the scaler rates, the $\pi^- \pi^0$ mass from K-decays, the neutral pion mass, and the overall yield of K-decays.

Because of their topological resemblence to $\rho^- \to \pi^- \pi^0$ events, $K^- \to \pi^- \pi^0$ decays served as a particularly important monitor. For each processed data tape, a record was made of the number of these decays that occurred within the decay pipe (25 inches to 225 inches downstream of the target). A plot of the yield of $K^- \to \pi^- \pi^0$ decays for a copper target is shown in Fig. 26.a. The low-yield point in the figure can be attributed to a known failure in the scalers that were used to record the incident beam count. Data runs that had severe difficultities of this kind were not used in the analysis. About 5% of the data were eliminated because of these types of failures. (The variation of the yield of K-decays as a function of target will be discussed in Chapter V.)

Figure 26.b shows the variation in the average value of the reconstructed $\gamma\gamma$ mass of the π^0's from K decays as a function of time. No clear reason could be found for the sudden shifts. One plausible explanation would attribute these fluctuations to changes in the high voltage that was applied to the LAC plates. These shifts are at the 1% level, which corresponds to a 2% change in the high voltage. Small empirical time-dependent correction factors were applied to the data to make the average calculated π^0 mass agree with the expected value.

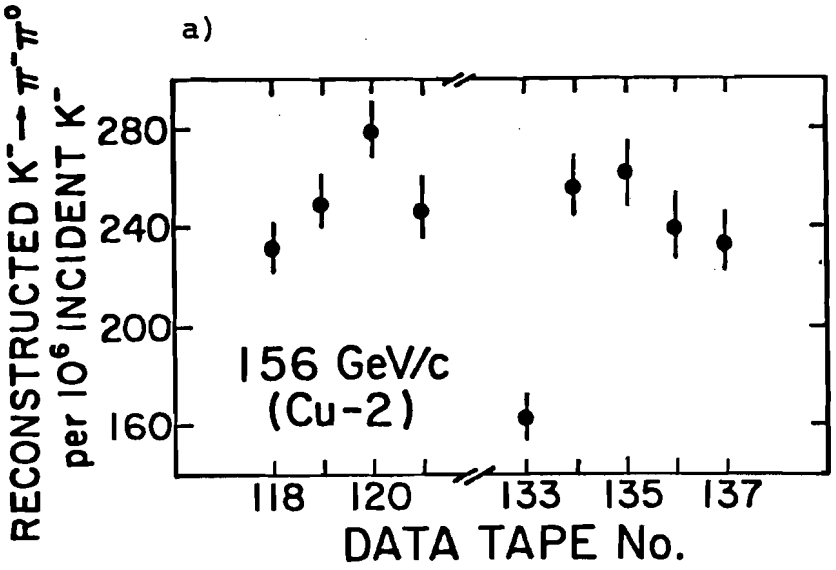
a)
RECONSTRUCTED K⁻ → π⁻π⁻π⁰
per 10⁶ INCIDENT K⁻
280
240
200
160
156 GeV/c
(Cu-2)
118
120
133
135
137
DATA TAPE No.

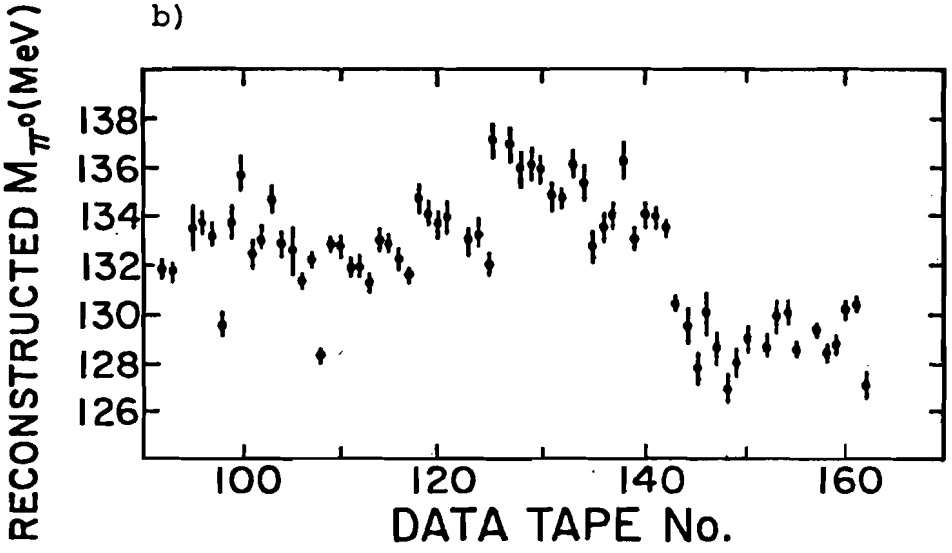
b)
RECONSTRUCTED M π⁰(MeV)
138
136
134
132
130
128
126
100
120
140
160
DATA TAPE No.

Figure 26

CHAPTER V

NORMALIZATION

A. Introduction

The partial width $\Gamma(\rho^- \to \pi^- \gamma)$ is directly proportional to the Coulomb production cross section for the ρ^-. Consequently, prior to extracting a value for $\Gamma(\rho^- \to \pi^- \gamma)$, it is essential to demonstrate that the absolute normalization of the cross section is reliable. Because it was difficult to determine the absolute efficiencies of certain parts of the spectrometer, and, moreover, because these efficiencies varied somewhat with time, kaon decays, collected simultaneously with ρ^- events, were chosen to establish the normalization of the data.

In Section B, we discuss correction factors that are independent of any specific reaction kinematics. The Monte Carlo model of the spectrometer acceptance, used to extrapolate efficiencies from K-decays to similar processes (e. g. $\rho^- \to \pi^- \pi^0$), is described in Section C. In Section D, the normalization procedure is checked through a comparison

of the observed cross section for $\Delta^+(1232)$ production with expectation from the Primakoff process.

B. Corrections Independent of Kinematics

Certain efficiencies, such as those related to performance of the electronics, were expected to be independent of the kinematics of any particular reaction. Corrections to account for these effects have been divided into the following categories: (1) beam related corrections, (2) target-dependent corrections, and (3) those factors related to the nature and performance of the spectrometer. These multiplicative correction factors are described below.

(1) Beam-related corrections

The procedure used for measuring the incident beam flux has been described in Chapter II. Corrections were applied to account for decays and interactions of beam particles, and for misidentification of particles by the Cerenkov counters.

Pions and kaons can decay before they reach the target. A Monte Carlo program was written to generate decays along the beamline of the type $\pi^- \rightarrow \mu^- \bar{\nu}$ and $K^- \rightarrow \mu^- \bar{\nu}$. It was found that the decay muon would be accepted by the beam defining elements only a small fraction of the time. Such decays

reduced the effective kaon and pion fluxes at both momenta by $\approx 0.4\%$.

Beam particles that interacted upstream of the target generally did not satisfy the strict beam definitions of the experiment. Also, because there was very little material in the 4 m upstream of the target ($\lesssim 2.0 \times 10^{-3}$ proton absorption lengths), the correction for such interactions was estimated to be $\lesssim 0.1\%$.

Another beam-related correction resulted from misidentification of particles in the Cerenkov counters. This was partially due to electronic noise, but mainly due to angular divergence of the beam. The efficiency curves shown in Figs. 6-8 were used to estimate the overall correction factors. The most significant problem occurred in the signal from the Cerenkov counter used to identify pions (K3). It was estimated from pressure curves that kaons caused a 0.1% background to the pion count at -156 GeV/c, 0.3% at +156 GeV/c, and 1.2% at -260 GeV/c. In addition, it was estimated from previous measurements[37] that the 156 GeV/c beam contained $\sim 0.5\%$ electrons and muons (the Cerenkov counters would record these as pions).

The above correction factors for different beam particles and incident momenta are listed in Table II.

Table II Correction Factors for Beam Flux

Particle type	Beam Momentum (GeV/c) -156	+156	-260
K	1.005 ± 0.002	1.005 ± 0.002	1.009 ± 0.003
P	1.015 ± 0.005	1.001 ± 0.001	1.11 ± 0.05
π	1.010 ± 0.003	1.012 ± 0.003	1.017 ± 0.003

Table III Target-Dependent Correction Factors

Target	δ-ray veto*	Absorption of photons from a π^0	Charged-track absorption π	K	P
C-1	1.063 ± 0.02	1.086 ± 0.0005	1.042	1.038	1.062
Al-1	1.043 ± 0.02	1.090 ± 0.0005	1.020	1.018	1.028
Cu-1	1.026 ± 0.02	1.089 ± 0.002	1.008	1.008	1.011
Cu-2	1.043 ± 0.005	1.188 ± 0.003	1.017	1.016	1.022
Pb-1	1.026 ± 0.02	1.243 ± 0.007	1.008	1.007	1.009
Pb-4	1.015 ± 0.02	1.116 ± 0.005	1.004	1.004	1.005

*This was measured for only Cu-2 and extrapolated to other targets, assuming that the effect scaled with target thickness in gm/cm^2.

(2) Target-dependent corrections

The yields were corrected for absorption of charged tracks and photons in the target, and for triggering losses caused by δ-rays produced in the target. (Refer to Table I for a summary of properties of the targets.)

The effect of losses due to δ-rays was measured for only one target (Cu-2), and the results were extrapolated to the other targets. To estimate vetos due to this source, a beam particle was required to pass through the target and strike the BA counter, located at the downstream end of the spectrometer (see Fig. 12). The rate at which the counters V1-V4 registered in coincidence with this signal was interpreted to be the level of vetoing of desired events due to δ-rays produced in the target. (A small correction of 0.5% was made for random firing by these counters.) The measurement for the Cu-2 target indicated a 4.1±0.5% veto rate. Owing to the multiple Coulomb scattering of the δ-rays, extrapolation to the other targets was somewhat uncertain. However, because the targets were all of similar thickness, the correction factors to account for δ-ray vetos (summarized in the second column of Table III) were estimated to be accurate to ±2%.

A correction for loss of photons caused by conversion to electron-positron pairs was calculated using the approximate formula, $N(t)=N_0\exp(-7t/9)$, for pair production

by a photon passing through t radiation lengths of material.[38] For interactions occurring in the target, t was taken to be half of the target thickness. The third column of Table III lists the correction factors to be applied to events for which two photons originated in the target.

In order to account for differences in the nuclear absorption cross sections for different types of incident particles, the data of Allaby et al[39] were used to calculate the correction factors for charged-particle absorption in the targets. These factors are listed in Table III for different beam particles and different targets.

(3) Spectrometer-related corrections

The remaining kinematics-independent correction factors are briefly described below.

	Correction Factor
a) Absorption in the S-counter (0.21 ±0.02 gm/cm^2 of polystyrene) provided the following correction factors:	
pion absorption	1.002 ±0.0002
kaon absorption	1.002 ±0.0002
proton absorption	1.003 ±0.0003
absorption of photons from a π^0	1.008 ±0.0006

b) Material in the chambers, counters, etc. amounted to $3.3 \pm 0.2 \times 10^{-2}$ proton-collision lengths and $7.6 \pm 0.4 \times 10^{-2}$ radiation lengths. The following corrections apply:

pion absorption	1.020 ± 0.002
kaon absorption	1.019 ± 0.002
proton absorption	1.035 ± 0.002
electron Bremsstrahlung (for Ke3 decays)	1.037 ± 0.005
absorption of photons from a π^0	1.060 ± 0.003

c) A measurement was made of losses caused by random firing of any of the counters V1-V4, H, A1, A2, AM, and the U/D counters. This required a correction of: 1.010 ± 0.003

d) An upper level discriminator threshold (S_{max}) was applied to the S-counter signal. The correction due to losses of triggers with large pulse heights (high energy tail of the Landau energy-loss distribution) was estimated from a pulse-height spectrum obtained with the $\overline{S_{max}}$ requirement removed from the trigger. This provided a correction of: 1.027 ± 0.005

Additional small losses were caused by inefficiencies in the chamber and trigger electronics, but because such losses affected all processes in the same manner, no major effort was made to quantify these corrections. (Such factors would be divided out in the process of normalizing to the $K^- \rightarrow \pi^- \pi^0$ yield.) It was seen in the previous chapter (Fig. 26.a) that fluctuations in such efficiencies were at a level of $\lesssim 10\%$.

C. Kaon Decays

In addition to the correction factors listed in the previous section, it was necessary to calculate geometrical and trigger-related acceptance factors for all processes of interest. This was accomplished using a Monte Carlo model of the spectrometer. The parameters of this model were determined, as indicated below, from a comparison of predictions with data.

1) The spatial resolution of the chambers, and the spatial and energy resolution of the LAC were determined from the studies of resolution described in Chapter III.

2) Values used for the magnetic field and the effective

length of the analyzing magnet were determined from the calibration of the BM109 magnet (see Chapter II.C). The magnet-aperture limits were determined by observing sharp cutoffs in the distribution of reconstructed charged-particle positions at the downstream end of the magnet. Other limiting apertures, such as the edges of the D4 chambers, and the edges of the LAC and the hole through its center, were also included in the Monte Carlo.

3) The transverse dimensions, angular divergence, and focus of the beam were determined from data on reconstructed beam tracks.

4) The transverse positions of the BV, BA, and VE counters were established from sharp cutoffs observed in spatial distributions of reconstructed charged tracks.

5) The logic signals MBV^2 and TC_ρ (see Chapter II.E) were simulated. For this purpose, efficiencies and noise levels observed in the proportional chambers were used to generate patterns of signals produced by charged particles passing through these chambers.

6) In order to simulate the response of the γ-logic (see Chapter II.E and Fig. 14), an "UP/DOWN" energy correlation was imposed on the Monte Carlo events. The energy deposited

by a photon in the LAC was distributed according to the measured shower shape. To this, a random energy level due to amplifier noise was added. Finally, a minimum energy requirement was imposed on the vertical sector of the LAC opposite the charged particle's trajectory.

7) Hadrons that interacted in the LAC could cause confusion in photon reconstruction. As indicated in Chapter IV.C, photons that were reconstructed within 0.75 inches of the projected charged-track position were rejected. In addition, events that had a photon within a 4 inch radius of the hadron were weighted assuming a loss that varied linearly with separation distance. Finally, the $VE \cdot E_{back}$ logic requirement (see Chapter II.E) was imposed in the Monte Carlo by randomly vetoing 40% of the events in which the charged track struck the VE counter.

8) In analyses of the data and of the Monte Carlo events, it was required that each photon deposit at least 10 GeV of energy in the LAC. This minimized problems encountered in the reconstruction of low energy photons.

Comparisons were made between Monte Carlo predictions and data for a number of kinematic variables associated with the $K^- \rightarrow \pi^- \pi^0$ decay. Several of these comparisons are given below for data at 156 GeV/c and at 260 GeV/c. Except where noted, the cuts applied to the data were the same as

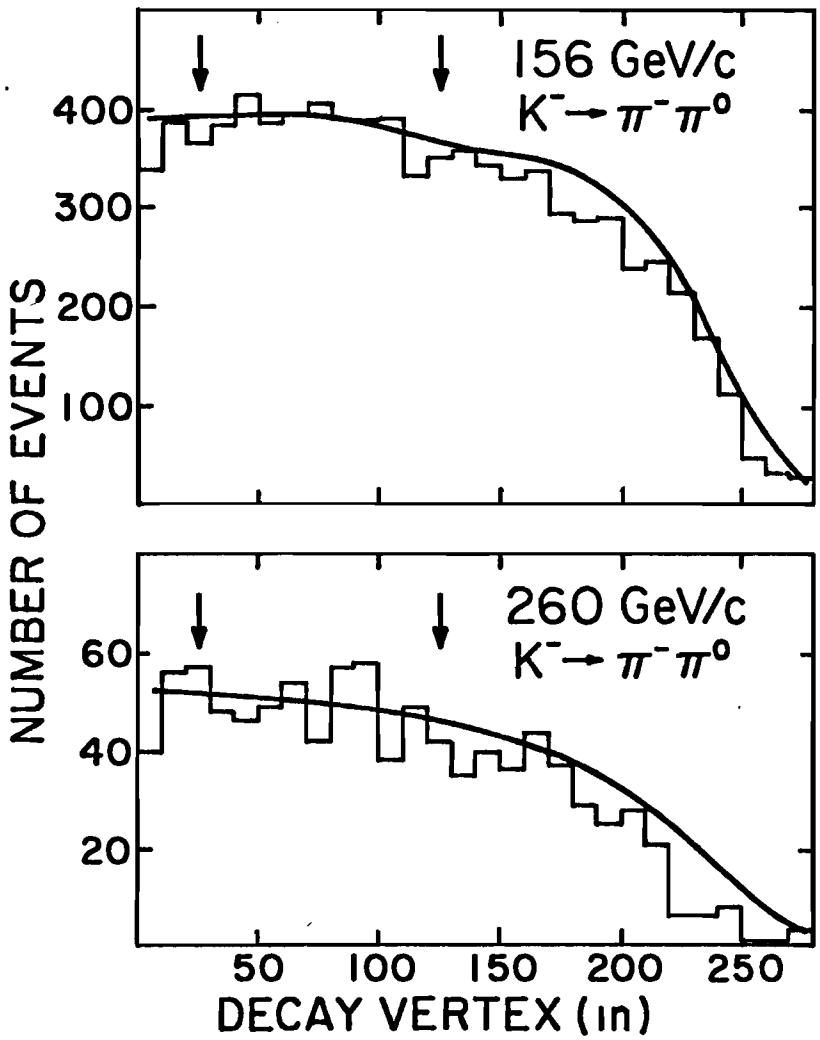
156 GeV/c
K⁻→π⁻π⁰
400
300
200
100
NUMBER OF EVENTS
260 GeV/c
K⁻→π⁻π⁰
60
40
20
50
100
150
200
250
DECAY VERTEX (in)

Figure 27

indicated in Chapter III.D.

Figure 27 shows the reconstructed decay-vertex distributions for $K^- \rightarrow \pi^- \pi^0$ decays. The sharp falloff at the downstream end of the decay pipe was caused primarily by the $\overline{MBV}^2$ requirement in the trigger. In order to avoid any problems associated with this logic circuit, only those events for which the decay vertex occurred between the arrows (25"-125") were selected for further analysis. The Monte Carlo prediction was normalized to the number of events within this cut. Losses near the origin (first bin) were caused principally by vetoing in the counters V1-V4; such losses were not considered in the Monte Carlo model.

Plots of the reconstructed radial positions of the charged pions at the P1 chamber are shown in Fig. 28. For these plots, an additional cut was made, as indicated, on the energy of the π^0. It was found (see below) that there was an excessive loss of high energy π^0's; because there is a correlation between π^0 energy and the transverse position of the π^-, such a loss would bias the above distributions. Agreement with the Monte Carlo predictions shows that there was no excessive loss of events caused by chamber inefficiency in the region of the beam. (In fact, at 156 GeV/c, most of the events within the acceptance of the spectrometer pass outside of the ($\lesssim$0.3" radius) region of the beam.)

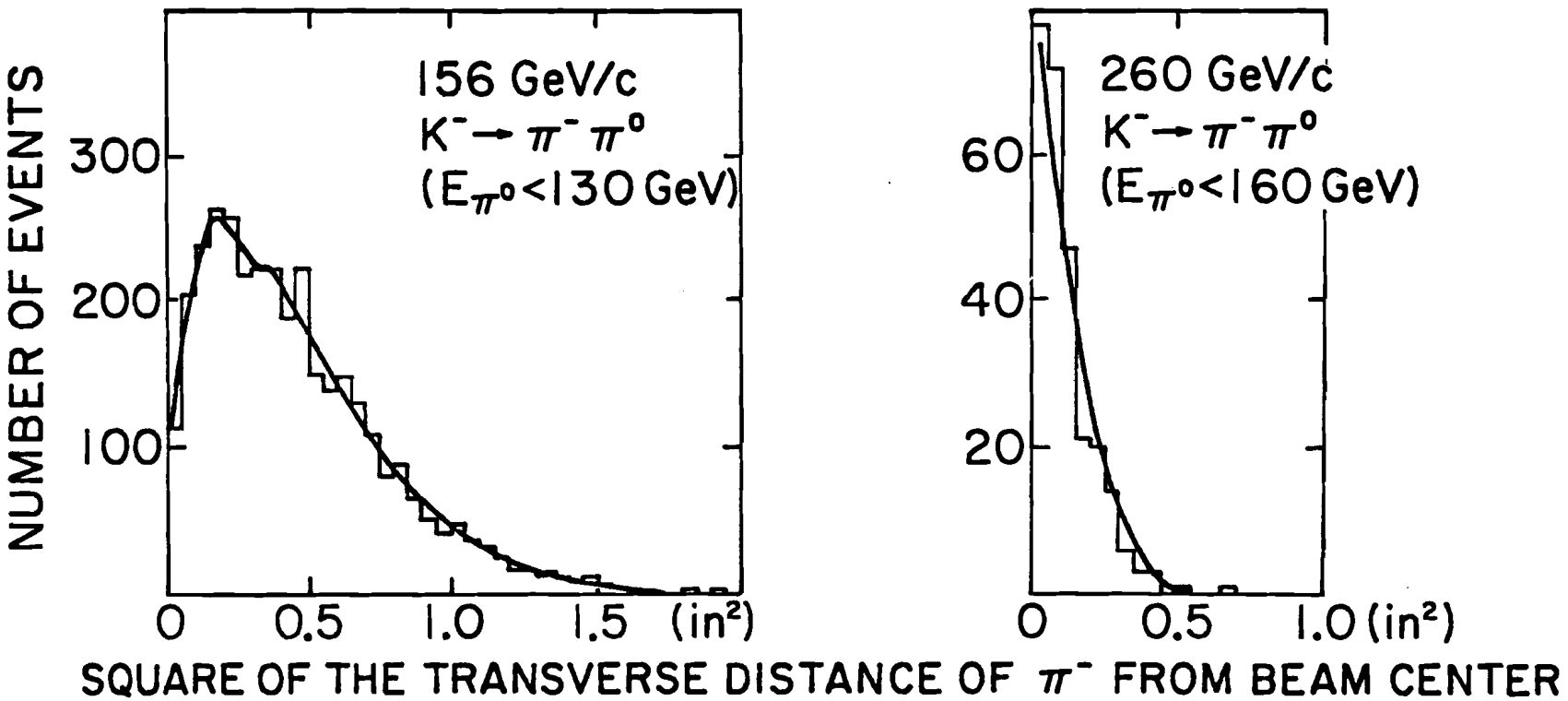
NUMBER OF EVENTS
300
200
100
156 GeV/c
K⁻→π⁻π⁰
(Eπ⁰<130 GeV)
0
0.5
1.0
1.5
(in²)
60
40
20
260 GeV/c
K⁻→π⁻π⁰
(Eπ⁰<160 GeV)
0
0.5
1.0 (in²)
SQUARE OF THE TRANSVERSE DISTANCE OF π⁻ FROM BEAM CENTER

Figure 28

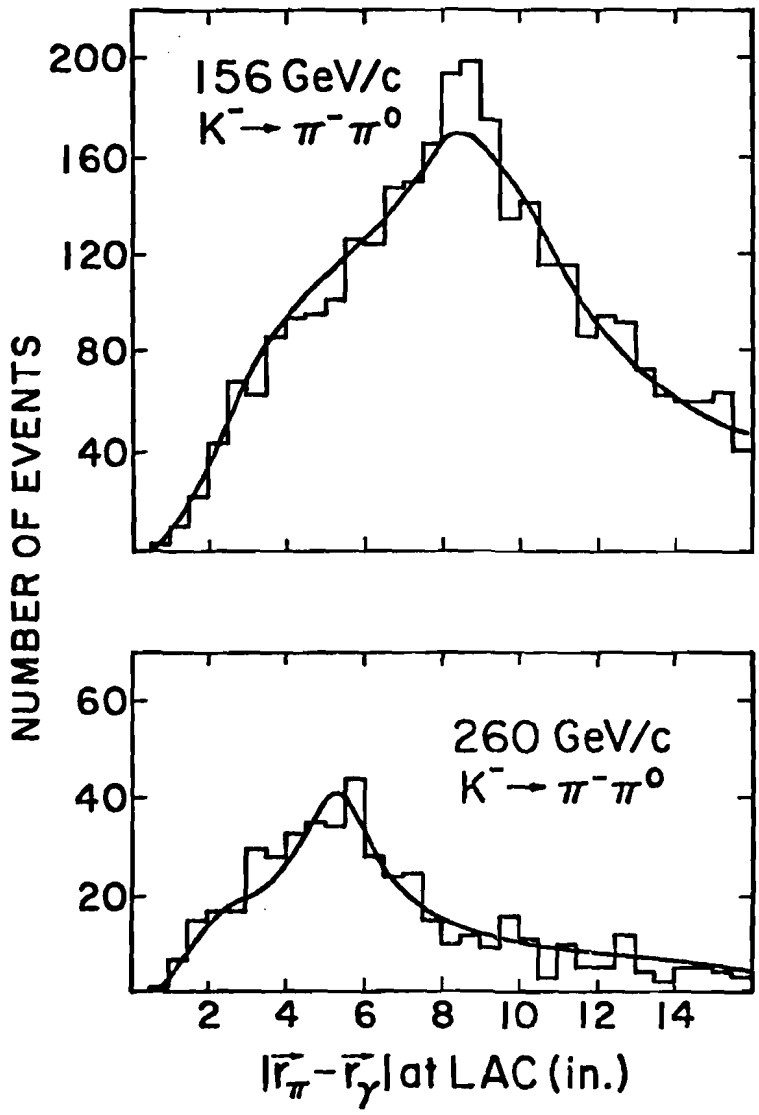
156 GeV/c
K⁻→π⁻π⁰
260 GeV/c
K⁻→π⁻π⁰
NUMBER OF EVENTS
200
160
120
80
40
60
40
20
2
4
6
8
10
12
14
|r⃗π − r⃗γ| at LAC (in.)

Figure 29

Figure 29 displays distributions of the separation between the pion and the nearest photon, calculated at the position of the LAC. Good agreement between the Monte Carlo predictions and the data indicates that the model used for handling hadronic interference with photon reconstruction is reasonable.

Helicity decay-angle distributions for $K^{\pm} \rightarrow \pi^{\pm}\pi^{0}$ decays are presented in Fig. 30. The angle θ is that of the charged pion relative to the flight direction of the kaon, as measured in the rest frame of the kaon. Because the kaon has no spin, its decay angular distribution should therefore be isotropic. Poor acceptance in the region of large $\cos\theta$ corresponds to losses due to vetoing of the charged track in the MBV^2, BA, and VE counters, as well as losses due to vetoing of low energy π^0's in the AM counters, and due to the threshold imposed on energy deposited in the LAC. The disagreement between the Monte Carlo prediction and the 260 GeV/c data is largely due to additional loss of high energy π^0's. For events which did not reconstruct, the LAC energy distributions for the two photons tended to overlap somewhat, and the reconstruction algorithm employed did not properly separate the two photons.

Further evidence of problems associated with photon reconstruction is indicated in Fig. 31; here we show distributions of the energy asymmetry, $|E_{\gamma 1} - E_{\gamma 2}|/(E_{\gamma 1} + E_{\gamma 2})$,

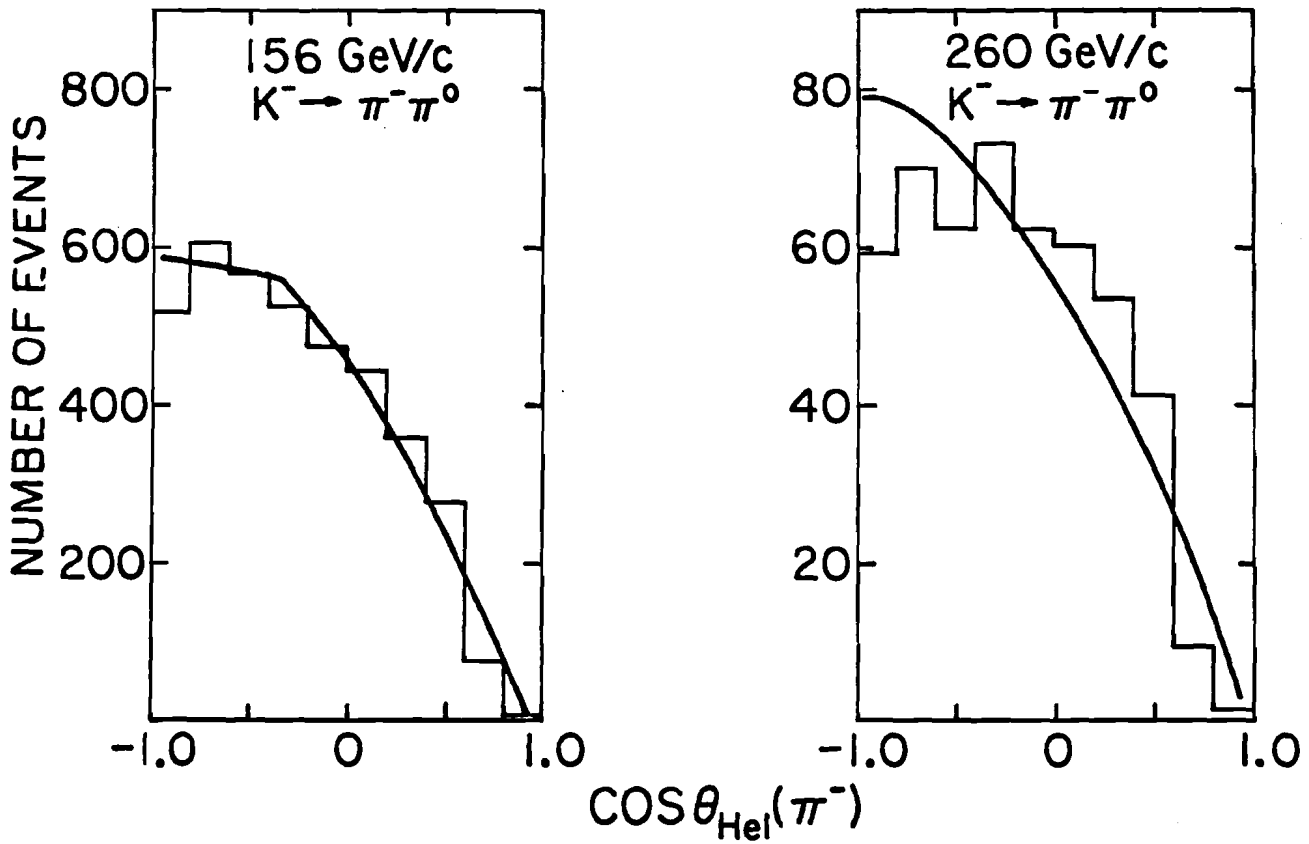
156 GeV/c
K⁻ → π⁻π⁰
260 GeV/c
K⁻ → π⁻π⁰
NUMBER OF EVENTS
800
600
400
200
80
60
40
20
-1.0
0
1.0
-1.0
0
1.0
COS θHel(π⁻)

Figure 30

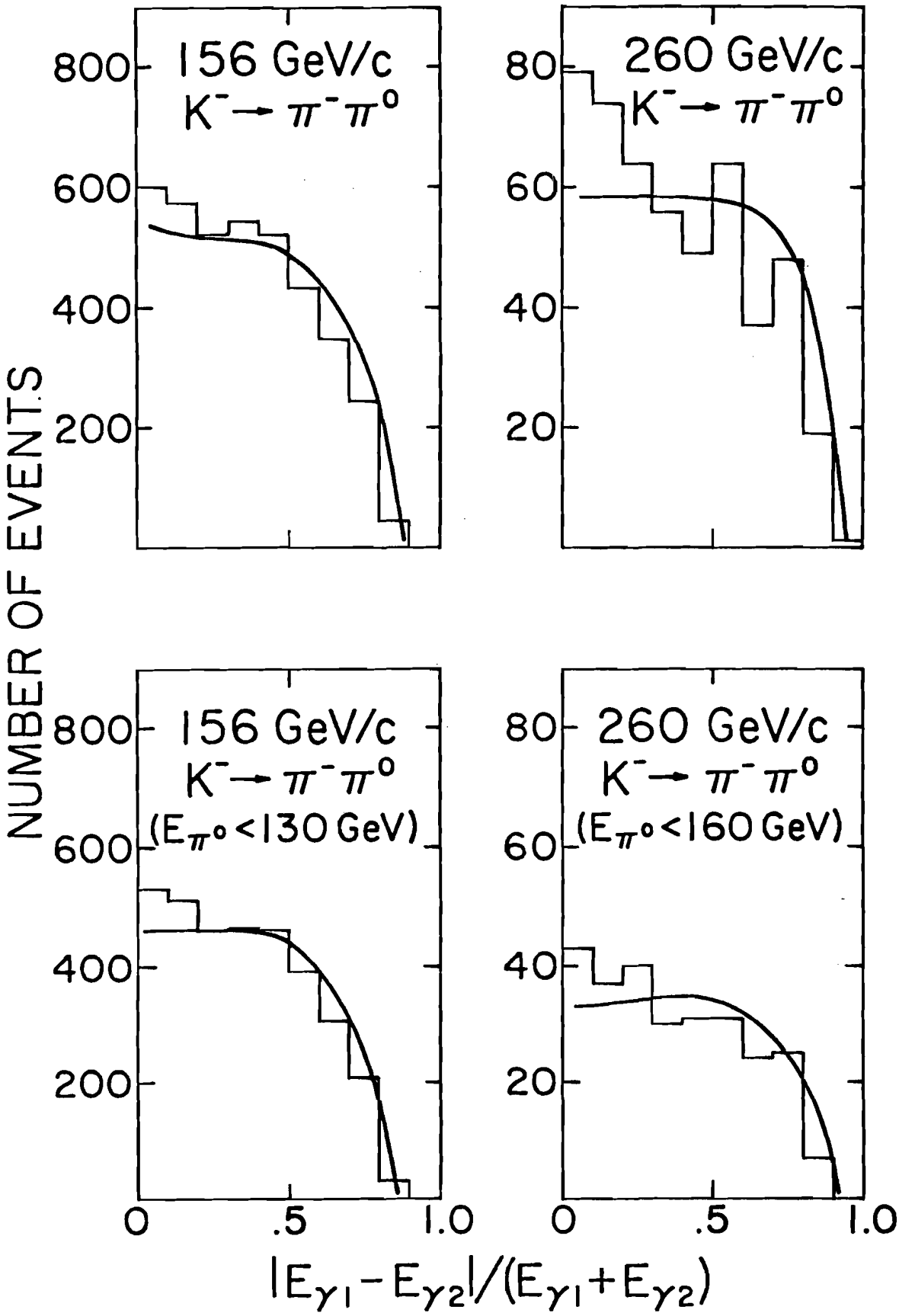
156 GeV/c
K⁻ → π⁻π⁰
260 GeV/c
K⁻ → π⁻π⁰
156 GeV/c
K⁻ → π⁻π⁰
(Eπ⁰ < 130 GeV)
260 GeV/c
K⁻ → π⁻π⁰
(Eπ⁰ < 160 GeV)
NUMBER OF EVENTS
800
600
400
200
80
60
40
20
0
.5
1.0
|Eγ1 − Eγ2|/(Eγ1 + Eγ2)

Figure 31

for the two photons from π^0 decays. In plots (a) and (b) the standard cuts used for defining $K^- \rightarrow \pi^- \pi^0$ events have been applied, whereas in (c) and (d), an additional cut was imposed (as indicated) to eliminate high energy π^0's. In all cases, the Monte Carlo predictions were normalized to the total number of events in the distributions. As can be seen, somewhat better agreement is obtained when high energy π^0's are eliminated. It would appear, therefore, that the losses observed in the decay-angle distributions tend to correspond to asymmetric π^0 decays.

The Ke3 decay process ($K^- \rightarrow e^- \bar{\nu} \pi^0$) was also studied in this experiment. Electrons were identified by requiring agreement between the LAC and the drift-chamber measurements of energies and positions of the charged tracks. The electron momentum spectrum and the decay-vertex distribution for Ke3 events are shown in Figs. 32.a and 32.b, respectively. The same acceptance model used for $K^- \rightarrow \pi^- \pi^0$ decays produced good agreement between the Ke3 data and the Monte Carlo predictions. The matrix elements listed in the recent Particle Data Tables[36] for Ke3 decay were used in generating the Monte Carlo events.

In order to verify that any remaining corrections (particularly those related to reconstruction efficiency) could be accounted for through normalization to K-decays, a small sample of K-decay candidates were analyzed in detail

a)

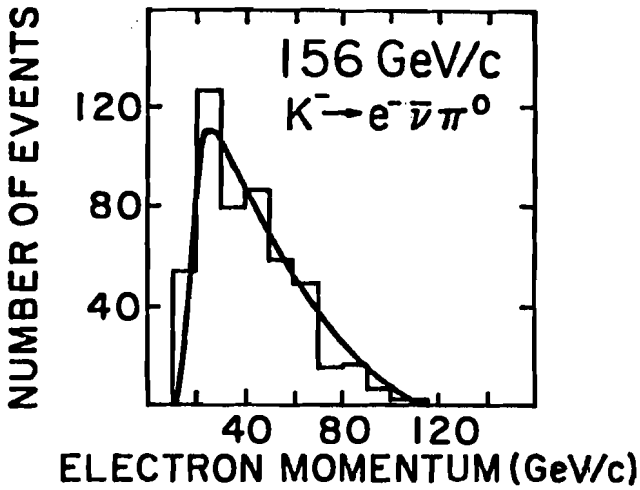
156 GeV/c
K⁻→e⁻ν̄π⁰
NUMBER OF EVENTS
120
80
40
40 80 120
ELECTRON MOMENTUM (GeV/c)

b)

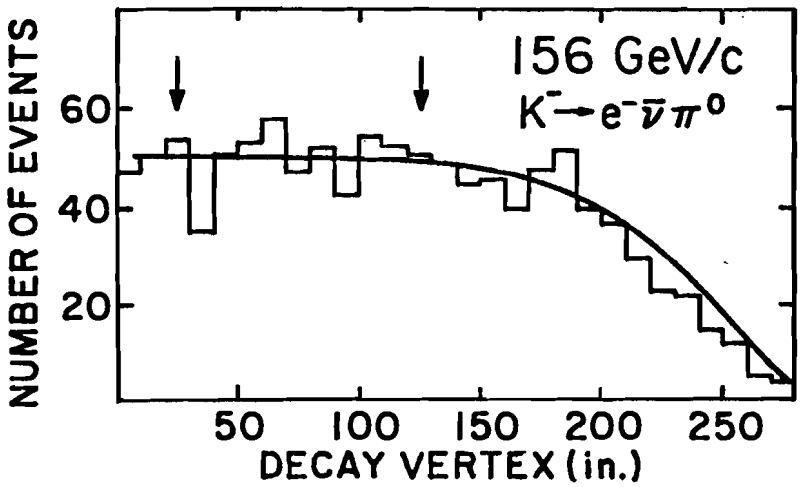
156 GeV/c
K⁻→e⁻ν̄π⁰
NUMBER OF EVENTS
60
40
20
50 100 150 200 250
DECAY VERTEX (in.)

Figure 32

using a visual display program. Approximately 600 triggers from each of two data runs were studied. For each event, a kaon signal was required to be present in the K1 Cerenkov counter and the reconstructed decay vertex was required to fall between 25 inches and 225 inches downstream of the target. Corrections for charged-track reconstruction efficiency and electronic triggering losses in the track-counters and in the γ-logic system were estimated from these data. The correction factors described in Section B were also applied, and, in addition, the Monte Carlo model was used to estimate the acceptance for the trigger.

The distribution of energy in the LAC was examined for each event with the aid of the graphical display program. For K-decay candidates which had not been uniquely defined by the reconstruction program, it was usually possible to observe one or more low energy photons which the reconstruction algorithm had failed to identify. This information, along with the kinematic quantities calculated by the reconstruction program, was used to determine, on an event-by-event basis, the type of kaon decay process that had occurred. The observed number of decays of any type was compared with the expected number based on the known K-decay branching ratios.[36] The excellent agreement shown in Table IV reenforced our confidence in the normalization procedure. On the basis of these studies, the single π^0 reconstruction

Table IV

Results from an event-by-event examination of K-decays occurring in the decay pipe

		TAPE 138 (Pb-1)	TAPE 155 (Empty)
K-beam count		1.291×10^6	1.100×10^6
efficiency common to all single-track decay modes		0.795 ± 0.024	0.854 ± 0.019
$K^- \to \pi^-\pi^0$	total efficiency	0.40 ± 0.03	0.43 ± 0.02
	observed/expected	0.96 ± 0.08	1.01 ± 0.08
$K^- \to e^-\bar{\nu}\pi^0$	total efficiency	0.30 ± 0.02	0.32 ± 0.02
	observed/expected	0.92 ± 0.11	1.00 ± 0.12
$K^- \to \pi^-\pi^0\pi^0$	total efficiency	0.28 ± 0.02	0.30 ± .02
	observed/expected	0.89 ± 0.23	0.92 ± .25

efficiency was estimated to be $\sim$80% at 156 GeV/c. This efficiency was calculated for only those events that had photon energies $>$10 GeV; in order to be considered an acceptable π^0, the two-photon mass had to be within the limits, 0.11 GeV $< M_{\gamma\gamma} <$ 0.16 GeV, as indicated in Chapter III.D. The primary cause of the 20% loss of genuine π^0's can be attributed to the lack of sophistication in the reconstruction algorithms employed; revised versions of these routines yielded better than a 95% reconstruction efficiency.

A test of the target-dependent correction factors is indicated in Fig. 33, where the ratios of observed to expected K-decay rates are plotted as a function of collision lengths of target material. Agreement among the yields for different targets was found to be good to $\pm$5%. In calculating these ratios, the correction factors listed in Section B as well as the Monte Carlo acceptance were taken into account. Electronic triggering losses and charged and neutral reconstruction efficiencies were not considered. The absolute value of this ratio for $K^- \to \pi^- \pi^0$ events is consistent with the 80% estimate for the reconstruction efficiency of a π^0 (the remaining $\sim$10% losses can be attributed to charged-track reconstruction and electronic triggering inefficiencies). The somewhat lower Ke3 detection efficiency can be attributed to the fact that, in addition to a π^0, an electron must also be reconstructed

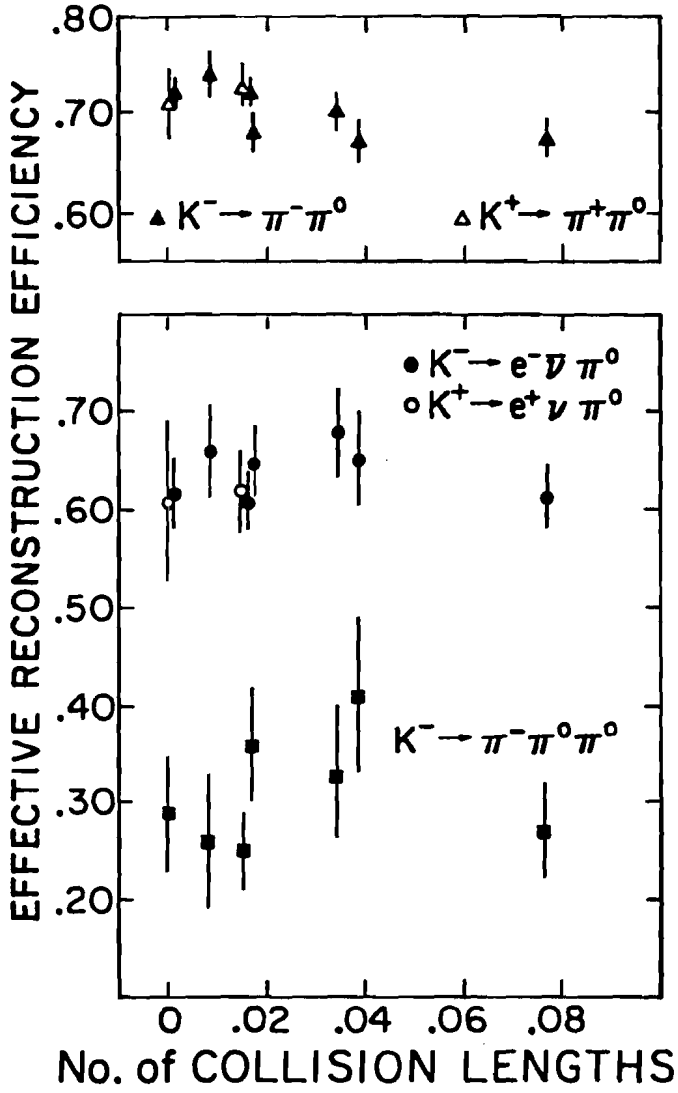
EFFECTIVE RECONSTRUCTION EFFICIENCY
.80
.70
.60
▲ K⁻→ π⁻π⁰
△ K⁺→ π⁺π⁰
.70
.60
.50
.40
.30
.20
● K⁻→ e⁻ν̄ π⁰
○ K⁺→ e⁺ν π⁰
K⁻→ π⁻π⁰π⁰
0
.02
.04
.06
.08
No. of COLLISION LENGTHS

Figure 33

in the LAC. The very low efficiency for $K^- \to \pi^- \pi^0 \pi^0$ events indicates the difficulty encountered in reconstructing photons with overlapping energy distributions.

The normalization procedure outlined in this section should be reliable for events that have kinematics similar to those for kaon decays. The largest uncertainties result from extrapolation of the preceding Monte Carlo estimated efficiencies to different processes, and from differences in the cuts applied to the different data samples.

As was shown in Chapter III.D, we imposed only loose requirements on the mass of the two photons, and on the total energy of the reaction products in $K^- \to \pi^- \pi^0$ decays. Consequently, because the same liberal cuts were applied in the analyses of other processes (e.g., $\rho^- \to \pi^- \pi^0$ events), the normalization to K-decays would be expected to take proper account for small overall losses imposed by such cuts.

A small correction (1.014±0.006 at 156 GeV/c, and 1.023±0.008 at 260 GeV/c) was made to account for the cut imposed on the $\pi^- \pi^0$ mass distribution defining the $K^- \to \pi^- \pi^0$ decay sample. Also, from a Monte Carlo analysis, the background to the accepted $K^- \to \pi^- \pi^0$ signal caused by $K\ell 3$ decays, was estimated to be about 1.5%.

The most noticeable difference between K-decays and data from interactions originating in the target is in the observed vertex distribution. To minimize any biases that this difference might introduce, the normalization procedure was carried out using only those K-decays having a vertex relatively close to the target (25 inches to 125 inches downstream). It was shown earlier in this section that the Monte Carlo predictions for these distributions from $K^- \rightarrow \pi^- \pi^0$ and Ke3 decays accurately reflect the observed data. Other tests of this question will be presented in the following section, where we will discuss $\Delta^+(1232)$ production. Data on ρ^- production will be described in Chapter VI.

D. $\Delta^+(1232)$ Production

In order to obtain sufficient statistics to study Coulomb production of the $\Delta(1232)$ resonance, several data runs were taken using a positively charged beam. The results from this study were compared with predictions of the Primakoff formula based on input from the well-measured photoproduction reaction $\gamma p \rightarrow p \pi^0$.[40,41] The cross section for the latter process is dominated by the $\Delta^+(1232)$ resonance.

The study of coherent production of $(p\pi^0)$ systems on nuclear targets is complicated somewhat by the presence of background from diffractive production. The Coulomb process, which is our primary concern, dominates at small momentum transfers (t). But just as in the case of ρ production, where other exchanges (ω and A_2) contribute at larger values of t, diffractive production of low-mass $(p\pi^0)$ systems contributes to coherent production for incident protons.[42,43,44] The diffractive process, which involves no isotopic spin exchange, can, in principle, be separated from resonant P_{33} Coulomb production by means of a partial wave analysis, but this requires substantially more data than we had available.

The t-distribution for the production of $(p\pi^0)$ systems on lead, for a reconstructed interaction vertex at the target, with the standard requirements for total energy balance, and for two-photon mass consistent with that of the π^0(see Chapter III.D), is shown in Fig. 34. When the mass of the $(p\pi^0)$ system is restricted to the Δ region (1.14 GeV $< M_{p\pi^0} <$ 1.28 GeV), the slope in the forward direction is seen to increase somewhat. In order to enhance the Coulomb contribution, the remaining analysis was performed using only those events that had $t < 0.001$ GeV^2.

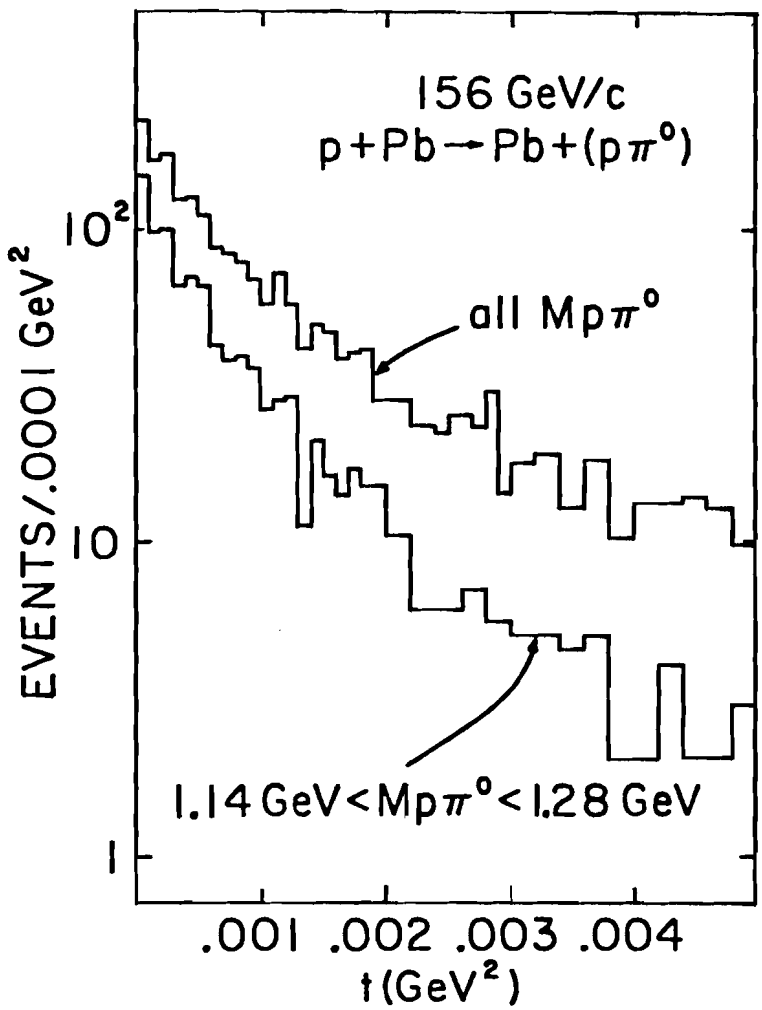
156 GeV/c
p+Pb→Pb+(pπ°)
all Mpπ°
1.14 GeV<Mpπ°<1.28 GeV
EVENTS/.0001 GeV²
10²
10
1
.001 .002 .003 .004
t(GeV²)

Figure 34

The ($p\pi^0$) production cross section was normalized to the $K^+ \rightarrow \pi^+\pi^0$ yield, in the manner described in the previous section. In order to best match the kinematics of the $\Delta^+ \rightarrow p\pi^0$ process, only those kaon decays for which the energy of the π^0 was less than 70 GeV were used in calculating the normalization factor. Using all kaon data yielded a ($p\pi^0$) cross section that was 10±7% lower. Because the $\Delta^+ \rightarrow p\pi^0$ kinematics differ substantially from those of $K^+ \rightarrow \pi^+\pi^0$ decays (the proton always carries away more than half of the total energy), this is an excellent check on the Monte Carlo model.

Figure 35 shows the distribution of the reconstructed interaction vertex for ($p\pi^0$) events with $t < 0.001$ GeV^2. (A background subtraction has been performed using target-empty data. The level of this background was 10%.) The smooth curve in the figure is the Monte Carlo prediction based on the same parameters as were used to describe K-decays. The arrows indicate the vertex limits used for analysis of the ($p\pi^0$) data. On the basis of the Monte Carlo curve, as well as the shape of the data, the correction for events falling outside these limits was estimated to be 4.0±2.0%.

The measured cross section for events at $t < 0.001$ GeV^2 is shown in Fig. 36.b as a function of mass. Figure 36.a shows the mass dependent acceptance for the decay of a J=3/2 state produced at small t through photon exchange (that is

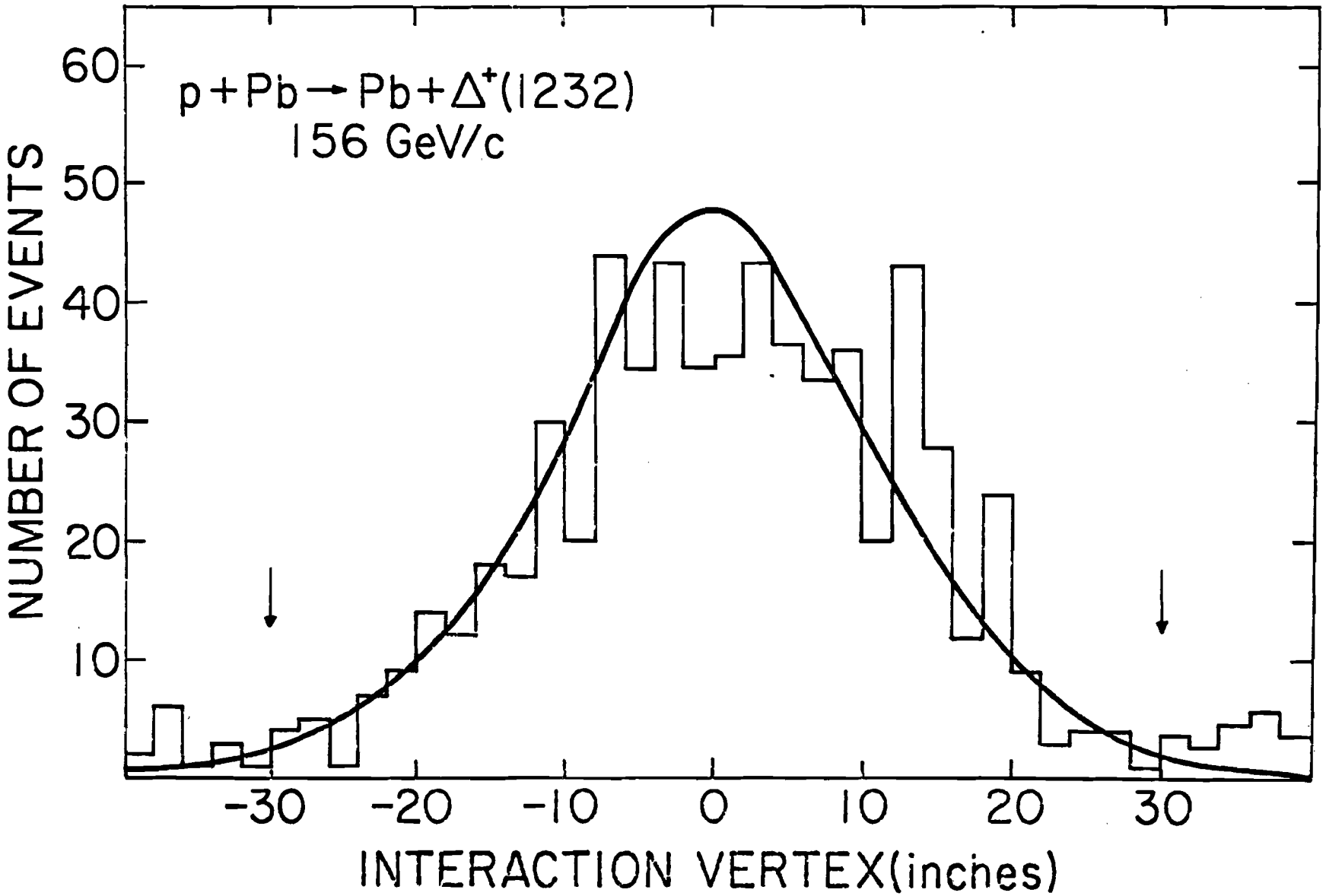
p+Pb→Pb+Δ⁺(1232)
156 GeV/c
NUMBER OF EVENTS
60
50
40
30
20
10
-30
-20
-10
0
10
20
30
INTERACTION VERTEX(inches)

Figure 35

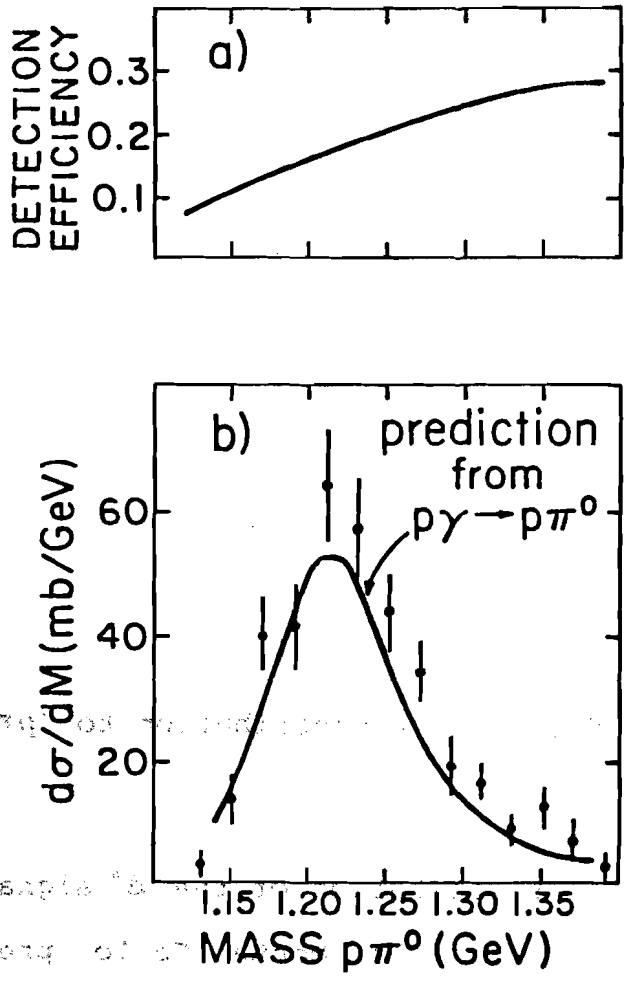
a)
DETECTION EFFICIENCY
0.3
0.2
0.1
b)
prediction from
pγ → pπ⁰
dσ/dM (mb/GeV)
60
40
20
1.15 1.20 1.25 1.30 1.35
MASS pπ⁰ (GeV)

Figure 36

using the "Stodolsky-Sakurai" decay distribution $1+3\sin^2\theta \sin^2\phi$ in the Gottfried-Jackson frame).[45] The solid curve was obtained by substituting the cross section $\sigma_\gamma(\gamma p \rightarrow p\pi^0)$ measured by Fischer et al[40], into Equation (3) of Chapter I, and integrating over t. In performing this integration, it was necessary to account for the resolution of the spectrometer. Owing to uncertainties in the parameters of the resolution function, the accuracy of the prediction was judged to be no better than $\pm 5\%$. (The resolution was determined by extrapolating the t-resolution from K-decays to Δ^+ production.)

Up to a mass of 1.25 GeV (Δ production should dominate in this interval), the expected yield agrees with our data to better than 10%. If the predicted cross section is subtracted from the data, the residual exhibits a broad peak at about 1.25 GeV. This is consistent with what might be expected for the diffractive contribution to $(p\pi^0)$ coherent production.[42,43]

The decay-angle distribution of the Δ^+ signal is shown in Fig. 37, along with the Monte Carlo prediction for $\Delta^+(1232)$ decay. The data selected for this plot were restricted to the mass interval $1.14\ \text{GeV} < M_{p\pi^0} < 1.28\ \text{GeV}$, and to $t < 0.001\ \text{GeV}^2$. For pure Δ^+ production, ignoring acceptance, the distribution should have the form $1+(3/2)\sin^2\theta$. Background from an S_{11} term should yield a

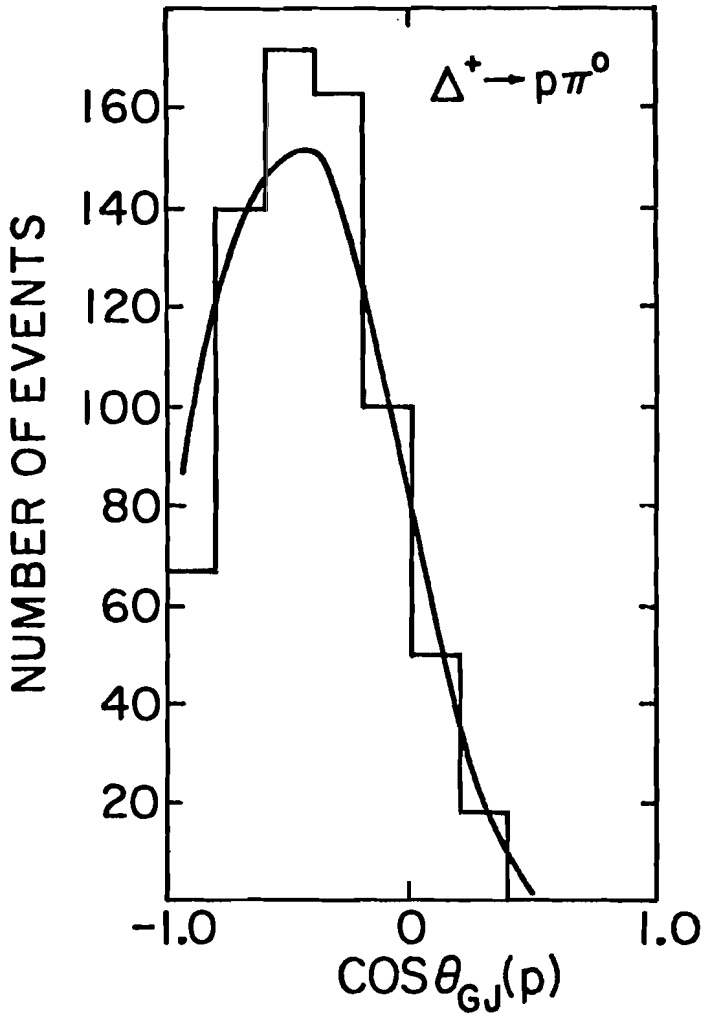
$\Delta^+ \rightarrow p\pi^0$
NUMBER OF EVENTS
160
140
120
100
80
60
40
20
-1.0
0
1.0
$\cos\theta_{GJ}(p)$

Figure 37

flat distribution, and background from diffractive production has a form which depends on mass and momentum transfer.[42,43,44] As was just noted for the ($p\pi^0$) mass spectrum of Fig. 36, these results are also consistent with Δ^+ dominance of the data and with negligible diffractive background for $t<0.001$ GeV^2 and $M_{p\pi^0}<1.28$ GeV.

This check has therefore provided further confidence in our normalization procedure. Even for the kinematically sensitive region of Δ^+ production and decay we have obtained results which are consistent with expectations to better than 10% accuracy.

CHAPTER VI

THE RHO DATA

A. Introduction

In this chapter we will check the reliability of our normalization procedures for the ρ^- data by comparing results of our Monte Carlo model with these data. Subsequently, we will normalize the cross section for Reaction (1) to the rate for $K^- \to \pi^-\pi^0$ decays. We will then present the mass and t-dependence of ρ production off several nuclei, and discuss the extraction of the radiative decay width of the ρ .

The evidence that Reaction (1) is dominated by ρ production is given in Figs. 38-40, where we display the observed $\pi^-\pi^0$ mass distributions for the different nuclear targets at the two energies. The events contained in these distributions have production vertex near the target (see next section), and restrictions on E_γ, $E_{\pi^-\pi^0}$, and $M_{\gamma\gamma}$ identical to those chosen to define $K^- \to \pi^-\pi^0$ decays (see Chapter III.D). All spectra display prominent peaks at the

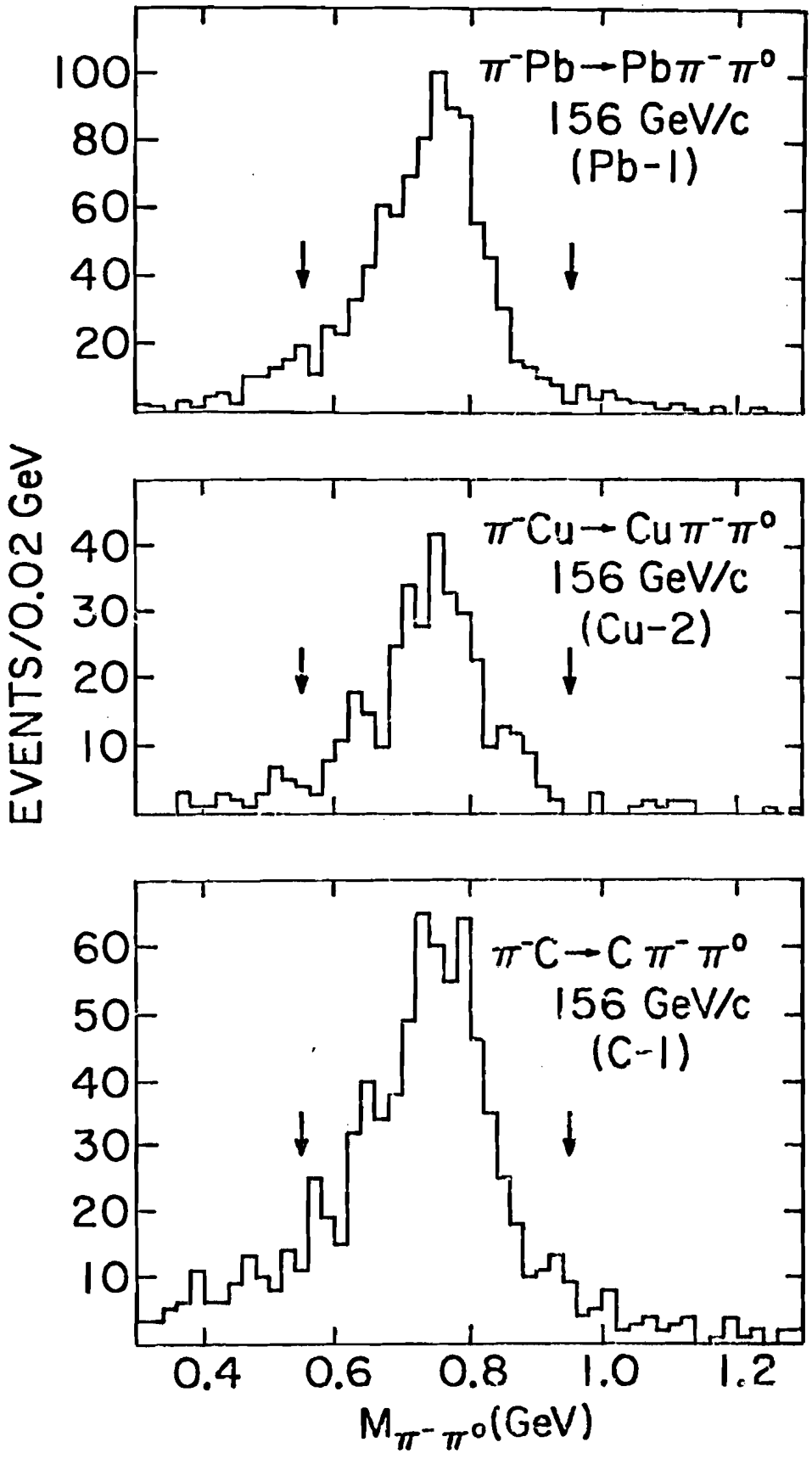
$\pi^- Pb \rightarrow Pb\pi^-\pi^0$
156 GeV/c
(Pb-1)
$\pi^- Cu \rightarrow Cu\pi^-\pi^0$
156 GeV/c
(Cu-2)
$\pi^- C \rightarrow C\pi^-\pi^0$
156 GeV/c
(C-1)
EVENTS/0.02 GeV
$M_{\pi^-\pi^0}$(GeV)
0.4
0.6
0.8
1.0
1.2

Figure 38

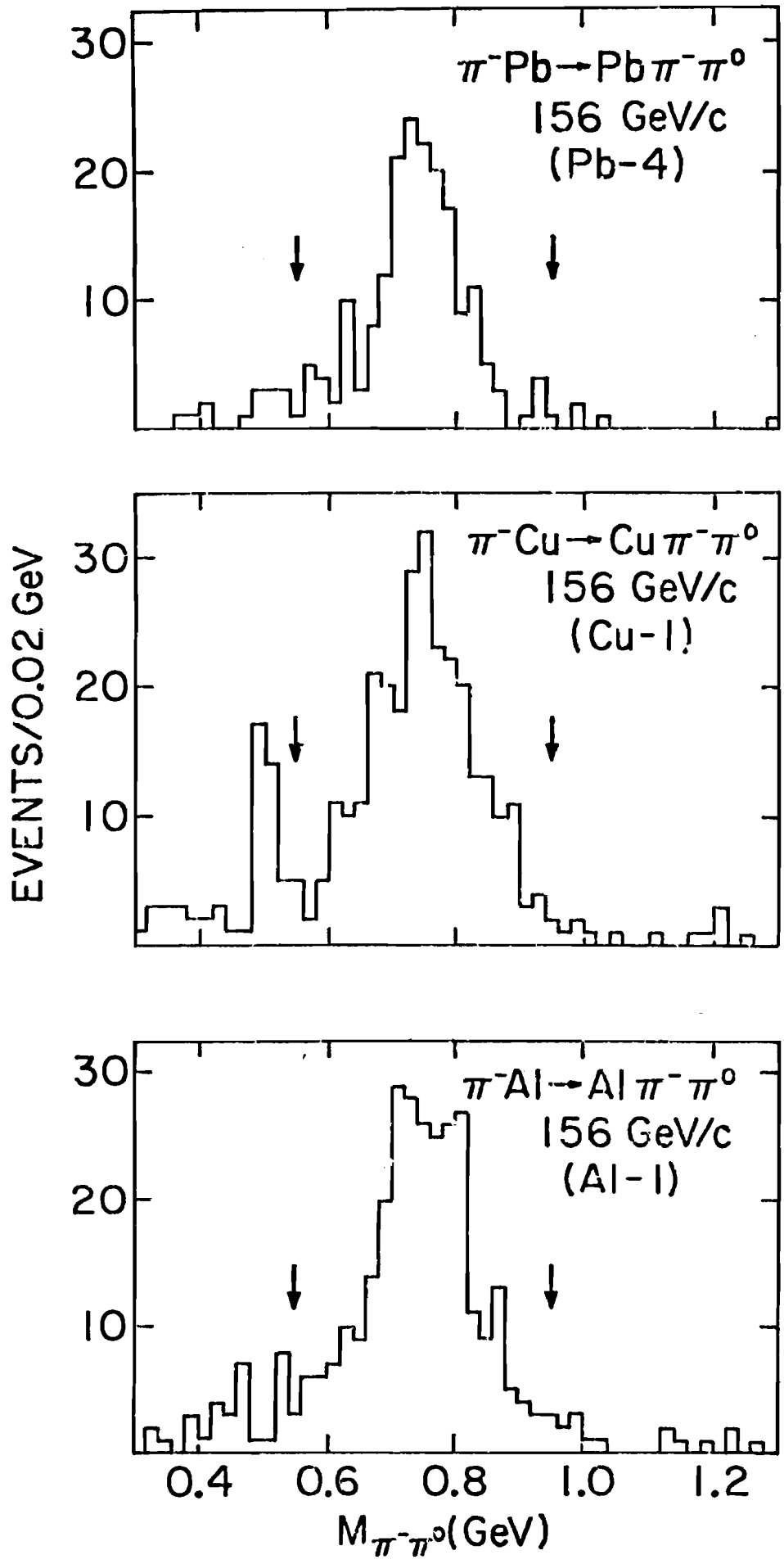
$\pi^- Pb \to Pb\pi^-\pi^0$
156 GeV/c
(Pb-4)
$\pi^- Cu \to Cu\pi^-\pi^0$
156 GeV/c
(Cu-1)
$\pi^- Al \to Al\pi^-\pi^0$
156 GeV/c
(Al-1)
EVENTS/0.02 GeV
30
20
10
0.4
0.6
0.8
1.0
1.2
$M_{\pi^-\pi^0}$(GeV)

Figure 39

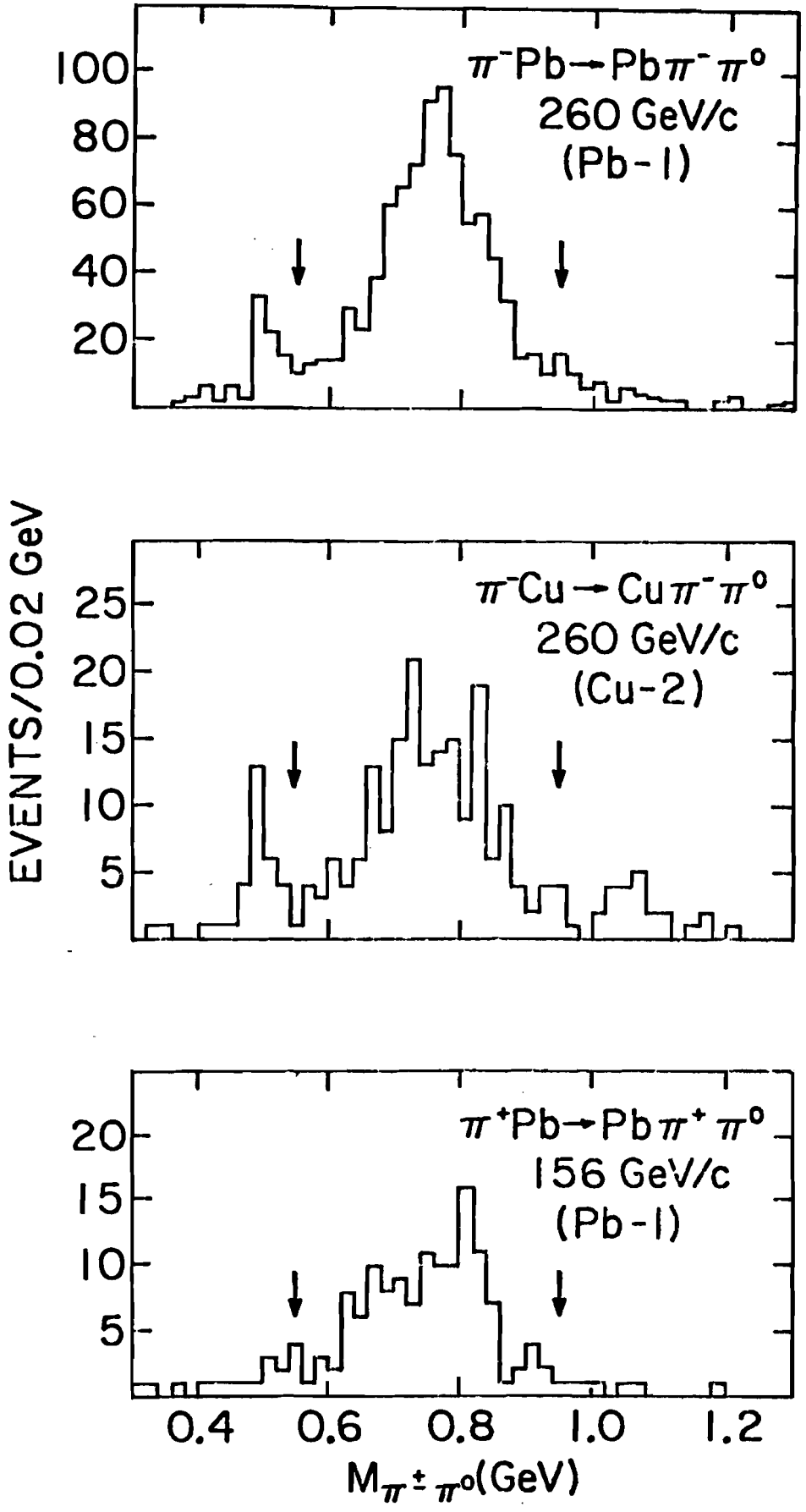
$\pi^- Pb \rightarrow Pb\pi^-\pi^0$
260 GeV/c
(Pb-1)
$\pi^- Cu \rightarrow Cu\pi^-\pi^0$
260 GeV/c
(Cu-2)
$\pi^+ Pb \rightarrow Pb\pi^+\pi^0$
156 GeV/c
(Pb-1)
EVENTS/0.02 GeV
$M_{\pi^\pm\pi^0}$(GeV)
0.4
0.6
0.8
1.0
1.2

Figure 40

mass of the ρ. The distributions for the Cu-1 target at 156 GeV/c and for all the 260 GeV/c data show an additional peak at $\sim$0.5 GeV caused by $K^- \to \pi^- \pi^0$ events for which the incident K^- was improperly tagged as a π^- by the Cerenkov counters. To avoid this background, in the following sections when we speak of ρ^- data, we will impose a cut on the $\pi^- \pi^0$ mass between 0.55 GeV and 0.95 GeV.

B. Comparison of ρ Data to the Monte Carlo Model

The model of the spectrometer described in Chapter V.C was also used to study the process $\rho^- \to \pi^- \pi^0$. In the Monte Carlo program, ρ^- events were generated at small t ($\lesssim$0.001 GeV^2; the acceptance was found to be essentially independent of t for t$\lesssim$0.1 GeV^2), and with a mass spectrum characteristic of the Primakoff process (see Chapter I.C and Section D of this chapter). The decay $\rho^- \to \pi^- \pi^0$ was then generated according to the angular distribution, $\sin^2\theta \sin^2\phi$ in the Gottfried-Jackson frame, expected for coherent production of the ρ^- (see Chapter I.B). For each event, the reaction products were traced through the apparatus to determine whether that event would be accepted, and the trajectories and energies were then smeared out to account for the resolution of the spectrometer. We compare below the predictions of this model with the data for Reaction (1).

Figure 41 shows distributions for the reconstructed interaction vertex for ρ^- candidates from Reaction (1) on a lead target. In addition to the requirements stated in the previous section, these data were restricted to $t < 0.002$ GeV^2; this emphasizes the coherent Coulomb production of the ρ^- (see Figs. 47-49 for t-distributions for ρ^- events). These data have also been corrected for target-empty background (present at a level of $\approx$3% for the Pb-1 target). Predictions from the Monte Carlo (solid curves) are in good agreement with the data at both energies. On the basis of this comparison, data selected to define Reaction (1) were required to have a vertex position between the arrows indicated in these plots ($\pm$10 in. at 156 GeV/c and $\pm$20 in. at 260 GeV/c). Losses due to these cuts were estimated from the Monte Carlo curves to be 3.0$\pm$1.5% at 156 GeV/c and 2.5$\pm$1.5% at 260 GeV/c (the numbers of events appearing outside these limits are consistent with these estimates).

Studies of K-decay data presented in Chapter V indicated an apparant π^0 reconstruction efficiency of $\sim$80%. To determine whether these losses were different for $\rho^- \to \pi^-\pi^0$ events, we investigated the dependence of the ρ^- data and of the $K^- \to \pi^-\pi^0$ events on several kinematic variables. To assure that there were no biases inherent in the normalization of Reaction (1) to $K^- \to \pi^-\pi^0$ events (due to the slightly different kinematic properties of the two processes), we compared the observed data for each process

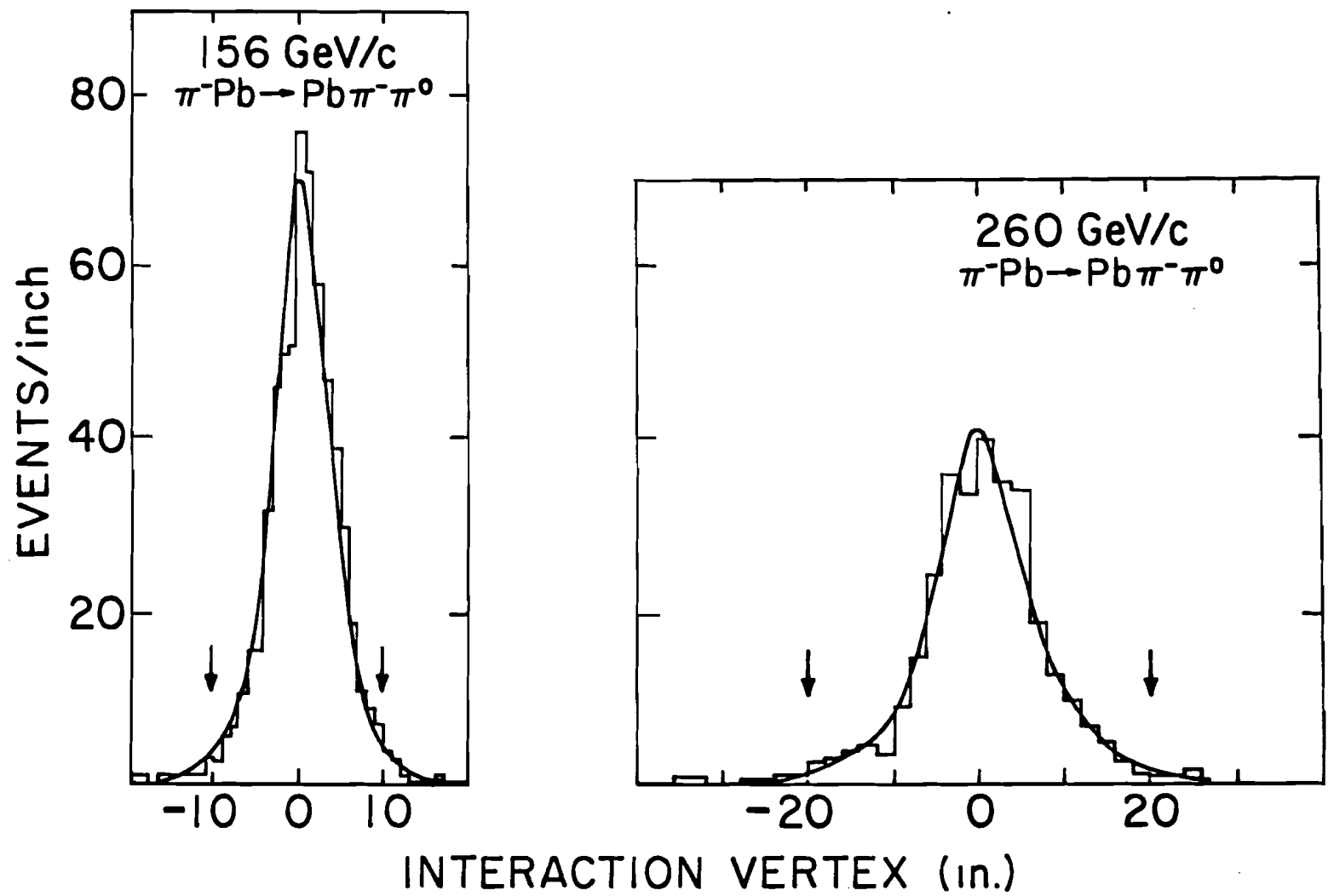
156 GeV/c
$\pi^- Pb \rightarrow Pb\pi^-\pi^0$
260 GeV/c
$\pi^- Pb \rightarrow Pb\pi^-\pi^0$
EVENTS/inch
80
60
40
20
-10
0
10
-20
0
20
INTERACTION VERTEX (in.)

Figure 41

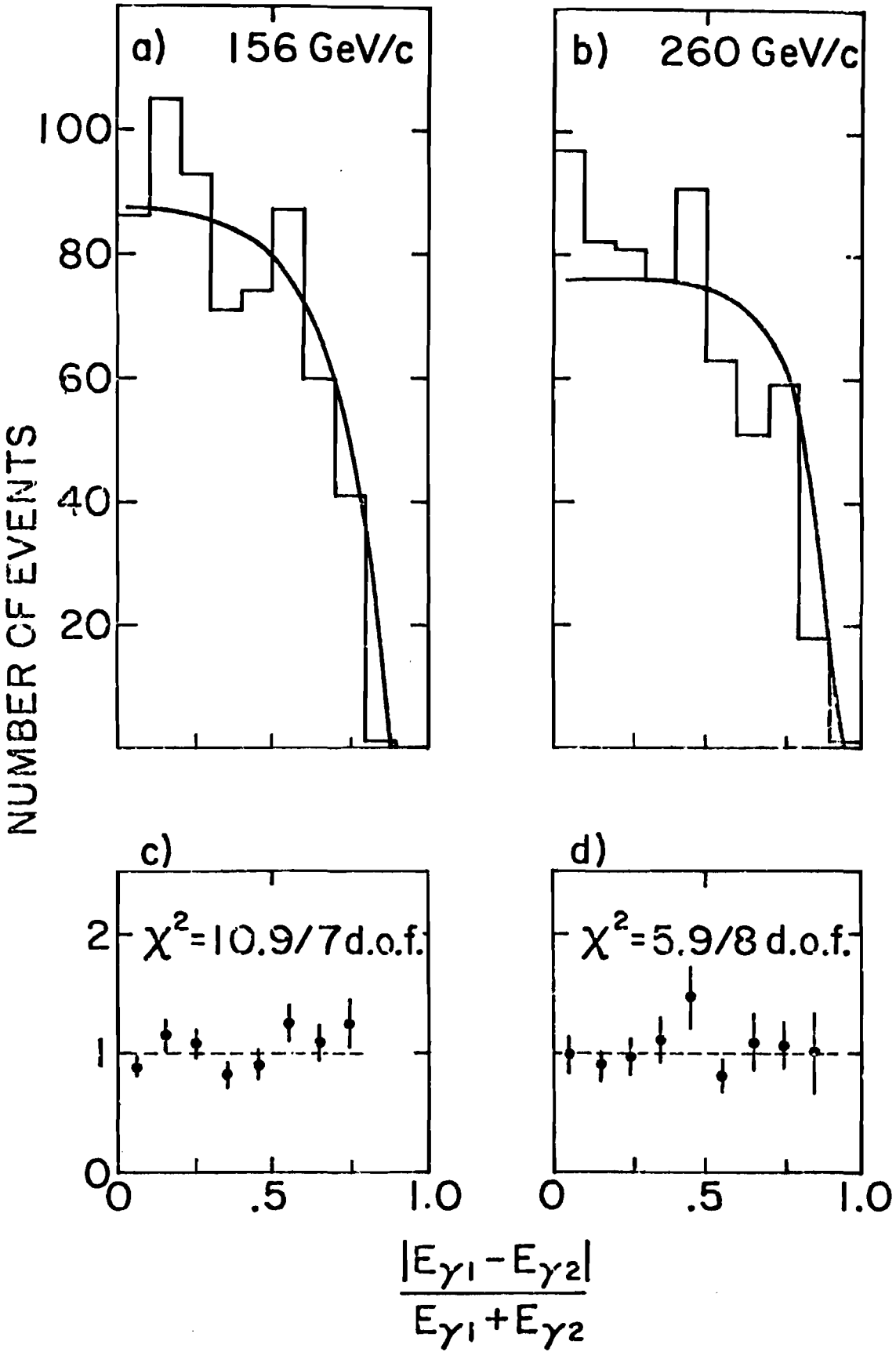
a) 156 GeV/c
b) 260 GeV/c
NUMBER OF EVENTS
100
80
60
40
20
c)
d)
χ^2=10.9/7d.o.f.
χ^2=5.9/8 d.o.f.
2
1
0
0
.5
1.0
$\frac{|E_{\gamma 1}-E_{\gamma 2}|}{E_{\gamma 1}+E_{\gamma 2}}$

Figure 42

with the predictions of our Monte Carlo model.

Figures 42.a and 42.b show the asymmetry in the photon energies for $\pi^0 \rightarrow \gamma\gamma$ decays from Reaction (1) on a lead target at 156 GeV/c, and 260 GeV/c, respectively (the corresponding distributions for $K^- \rightarrow \pi^- \pi^0$ decays were presented in Fig. 31). The restrictions applied to these data were the same as described in Section A, with an additional requirement that $t < 0.002$ GeV^2. The Monte Carlo predictions are indicated by the solid curves. In Figs. 42.c and 42.d we show the ratio of the acceptance-corrected ρ^- data to the corresponding $K^- \rightarrow \pi^- \pi^0$ data. The constancy of the ratio indicates good internal agreement between the ρ^- and K^- processes.

Further confirmation of the self-consistency of the normalization procedure is provided by the decay-angle distributions shown in Figs. 43.a and 43.b. Restrictions on these data were the same as for the asymmetry plots, and the data points have been corrected for target-empty background and for geometric acceptance. The results are in excellent agreement with the $\sin^2\theta$ dependence expected for the decay of coherently produced ρ^- mesons (see Chapter I.B). At small values of t, the ϕ dependence is dominated by the resolution of the spectrometer. Thus we do not observe the expected $\sin^2\phi$ form; a result consistent with the Monte Carlo predictions. Figures 43.c and 43.d show the ratio of

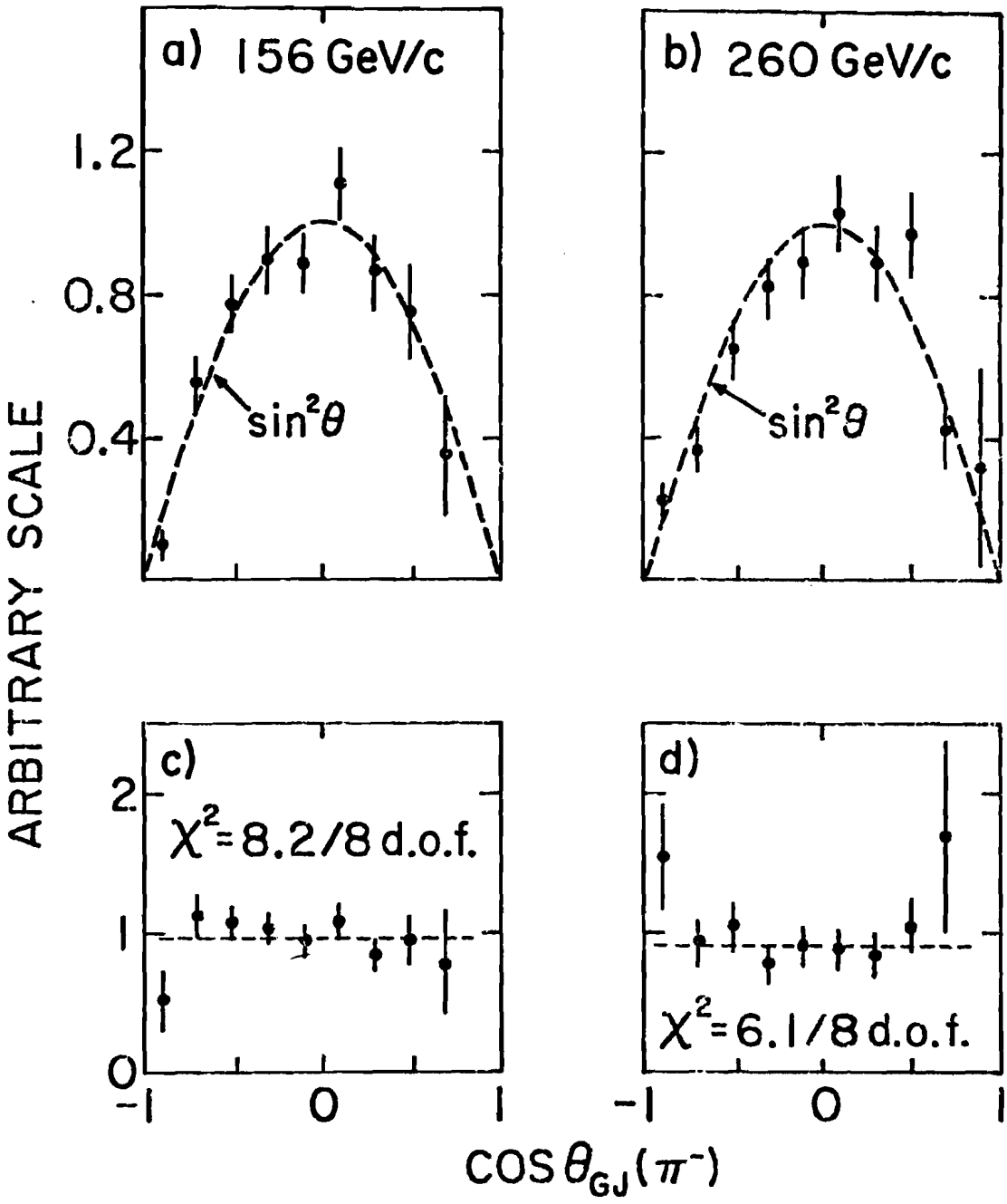
a) 156 GeV/c
b) 260 GeV/c
1.2
0.8
0.4
sin²θ
sin²θ
ARBITRARY SCALE
c)
χ²=8.2/8 d.o.f.
d)
χ²=6.1/8 d.o.f.
2
1
0
-1
0
1
-1
0
1
COS θGJ(π⁻)

Figure 43

the acceptance-corrected ρ^- data to the corresponding $K^- \to \pi^- \pi^0$ data. Once again, the observed ratio is consistent with being constant and indicative of the reliability of our normalization procedure.

Agreement of the angular distribution with a $\sin^2\theta$ shape is also an indication that there is very little inelastic background present in the data at small t. The most likely source of such background would be coherent $A_1^- \to \pi^- \pi^0 \pi^0$ production in which one of the π^0's was not detected or was improperly reconstructed. The background from A_1^- production would be expected to yield a large $\cos^2\theta$ component due to the presence of contributions from the π-exchange Deck diagram.[46] The good energy resolution of our apparatus allowed us to eliminate most of this background. Distributions of the reconstructed energy of the $\pi^- \pi^0$ system are shown in Figs. 44.a, and 44.b for carbon, and lead targets, respectively. The upper data have no t-restriction, while the shaded area contains only those events for which $t < 0.002$ GeV^2; Coulomb production dominates in this region. Inelastic background is evident in the low energy tail of the distributions. Most of this background was eliminated by requiring that the total energy for a candidate for Reaction (1) be between the arrows indicated in Fig. 44. From studies of these distributions, we have estimated that, for the worst case (carbon target), the inelastic background is $\lesssim 2\%$ of the coherent signal for

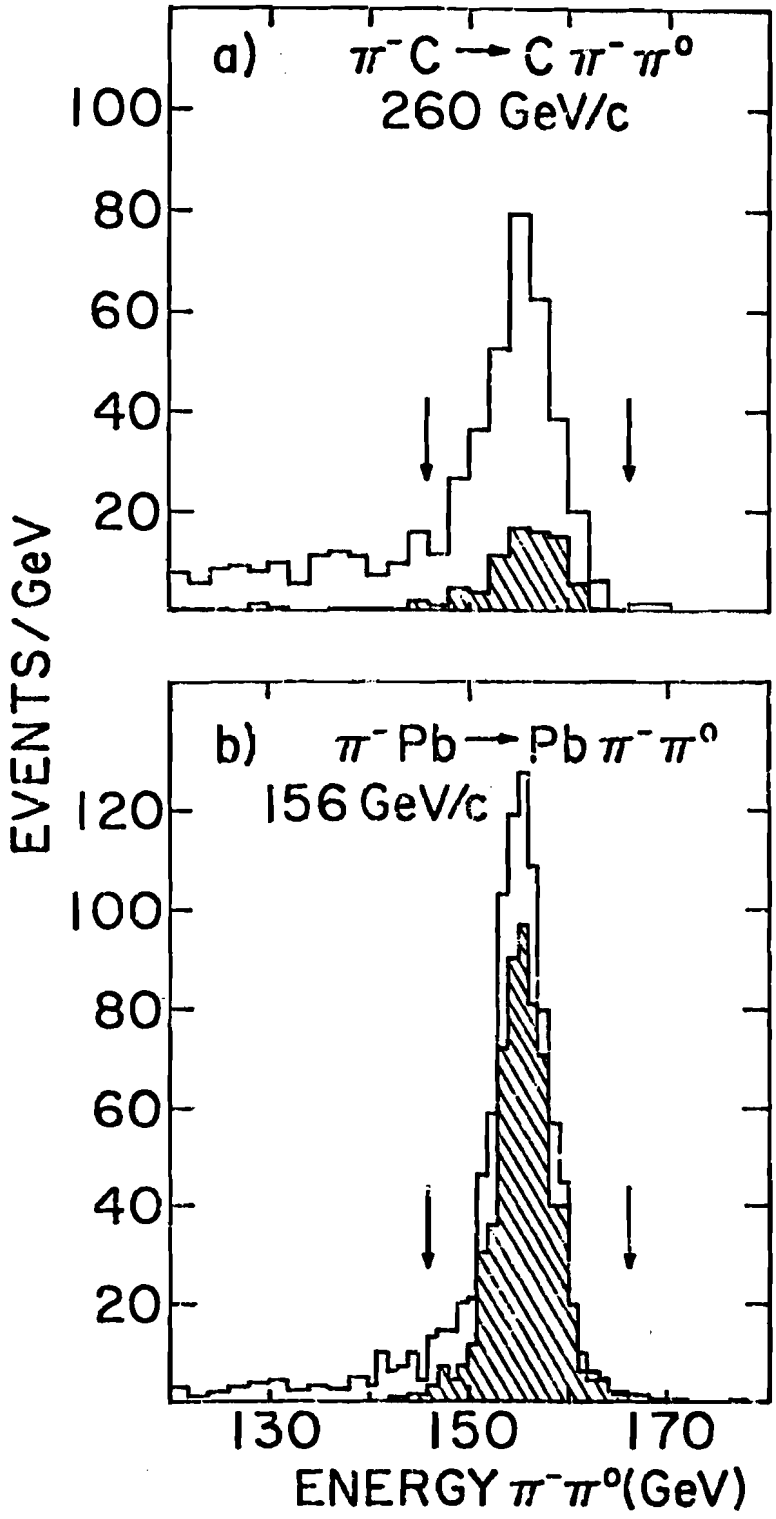
a) $\pi^- C \rightarrow C \pi^- \pi^0$
260 GeV/c
b) $\pi^- Pb \rightarrow Pb \pi^- \pi^0$
156 GeV/c
EVENTS/GeV
100
80
60
40
20
120
130
150
170
ENERGY $\pi^- \pi^0$(GeV)

Figure 44

$t<0.002$ GeV^2.

C. Calculation of Cross Sections

The cross section for one interaction can be written as follows:

$$\sigma(\text{per event}) = \frac{A}{N_0 \rho t} \frac{\text{C. F.}}{(\text{incident flux})}$$

where $N_0 = 6.02 \times 10^{23}$ is Avogadro's number, and ρt is the thickness of the target in gm/cm^2. The incident flux was determined using the scintillation and the Cerenkov counters described in Chapter II.B. The correction factor (C. F.) includes the geometric acceptance (averaged over any particular range of kinematics, e. g., a $\pi^-\pi^0$ mass interval) and the normalization factor from the yield of K-decays. These correction factors are tabulated in Table V, along with the values of the cross section per event, for the different targets and different energies. In this table, the geometric acceptance has been averaged over the mass interval 0.55 GeV$< M_{\pi^-\pi^0} <$ 0.95 GeV. (The differences in the geometric acceptance between the two targets at 260 GeV/c are due to small changes made in the trigger used for accumulating data.)

Table V

Correction factors to be applied in determining the cross section for the process

$\pi^- A \rightarrow A\pi^-\pi^0$

Energy (GeV/c)	-156						+156	-260	
Target	C-1	Al-1	Cu-1	Cu-2	Pb-1	Pb-4	Pb-1	Cu-2	Pb-1
Corrections common to K-decay	1.284	1.258	1.237	1.261	1.236	1.223	1.262	1.256	1.240
Beam-count correction	1.010 ± 0.001						1.012±0.003	1.017 ± 0.003	
Absorption in S-counter	1.010 ± 0.001								
Absorption in target	1.132±0.001	1.112±0.001	1.098±0.002	1.208±0.003	1.253±0.007	1.120±0.007	1.253±0.007	1.208±0.003	1.253±0.007
Interaction-vertex cut	1.03 ± 0.015							1.025 ± 0.015	
Geometric[a] acceptance	2.09 ± 0.04							1.70 ± 0.03	1.62 ± 0.03
K-decay normalization	1.52 ± 0.06	1.51 ± 0.06	1.46 ± 0.06	1.45 ± 0.06	1.40 ± 0.06	1.37 ± 0.06	1.38 ± 0.06	1.51 ± 0.12	1.60 ± 0.10
Total C.F.	4.85 ± 0.23	4.64 ± 0.22	4.35 ± 0.21	4.85 ± 0.23	4.76 ± 0.23	4.12 ± 0.20	4.80 ± 0.23	4.10 ± 0.62	4.24 ± 0.64
σ (per event) (μb/event)[b]	0.040±0.002	0.302±0.014	0.763±0.037	0.624±0.030	1.38 ± 0.07	6.55 ± 0.31	6.98 ± 0.34	1.30 ± 0.20	1.81 ± 0.28

(a) Averaged over the mass interval 0.55 GeV < $M_{\pi^-\pi^0}$ < 0.95 GeV, and using a $\sin^2\theta \sin^2\phi$ distribution for the decay of the ρ^-.

(b) Errors include uncertainties in the target thicknesses, as well as in the correction factors.

The major source of error in the cross section per event was due to the normalization of the ρ data to the yield of K-decays. To further probe this uncertainty, we varied several of the cuts applied to the data and observed the extent to which the resulting cross sections were modified. For instance, changing the requirement for the minimum value of the energy of a reconstructed photon from 8 GeV to 12 GeV, or restricting the energy of the π^0 to $<$130 GeV, resulted in $\pm$3% variations in the cross section at 156 GeV/c.

Results at 260 GeV/c were found to be somewhat more sensitive to changes in the cuts applied to the data, however, the statistics for K-decays at 260 GeV/c were poor. Using events for which the π^0 energy was $<$160 GeV, yielded a cross section for ρ^- production that was 10$\pm$7% lower for the lead target, and 20$\pm$15% higher for the copper target, than when no such energy restriction was imposed on the data. Thus the cut on the π^0 energy does not appear to have any systematic effect on the ρ^- yield.

D. The $\pi^-\pi^0$ Mass Spectrum

Figures 45, and 46 show the dipion mass spectra for Reaction (1) for events with $t < 0.002$ GeV^2 produced on the Pb-1 target at 156 GeV/c, and 260 GeV/c, respectively. The

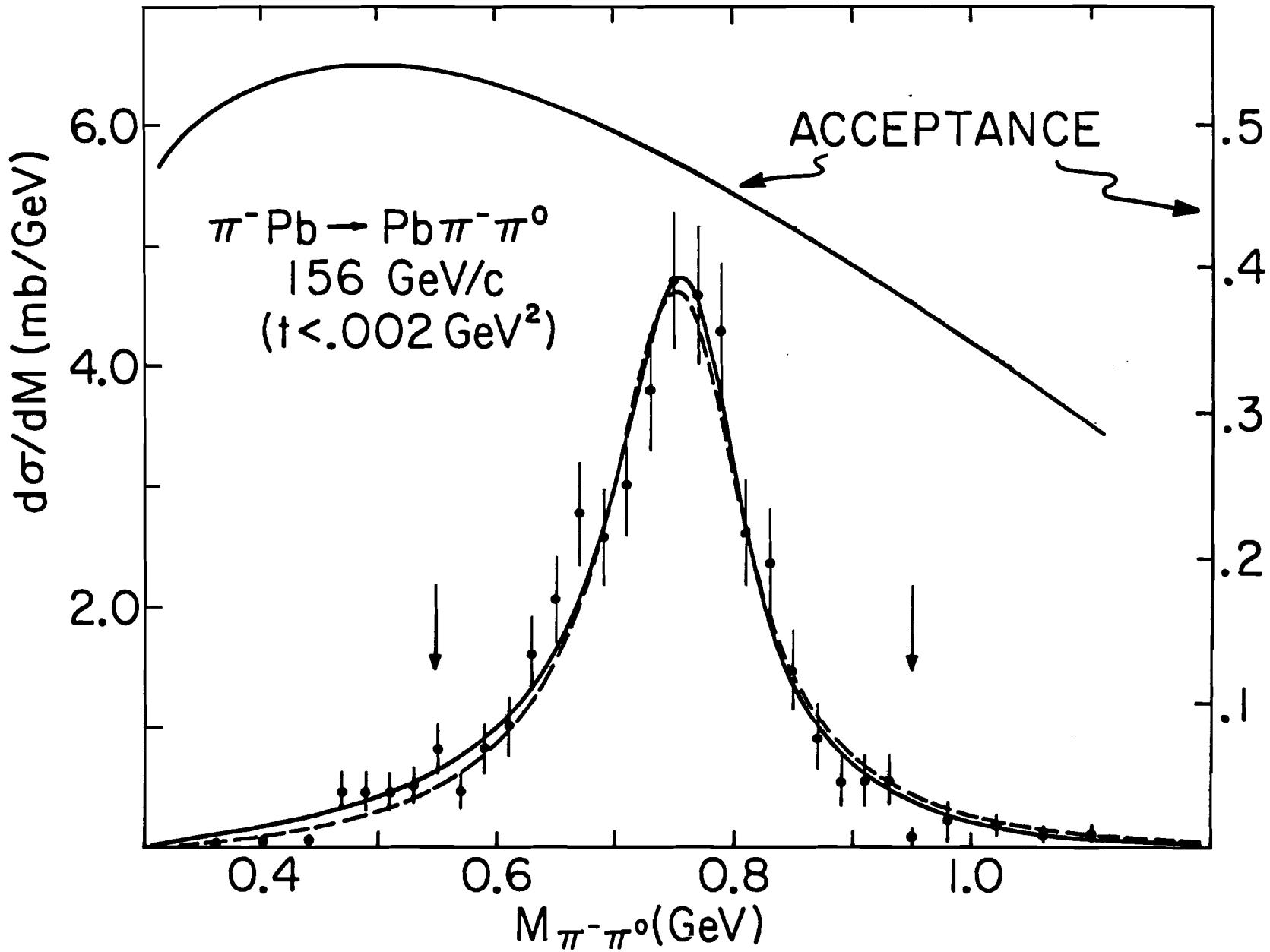
ACCEPTANCE
$\pi^- Pb \rightarrow Pb\pi^-\pi^0$
156 GeV/c
($t<.002\ GeV^2$)
$d\sigma/dM$ (mb/GeV)
6.0
4.0
2.0
.5
.4
.3
.2
.1
0.4
0.6
0.8
1.0
$M_{\pi^-\pi^0}$(GeV)

Figure 45

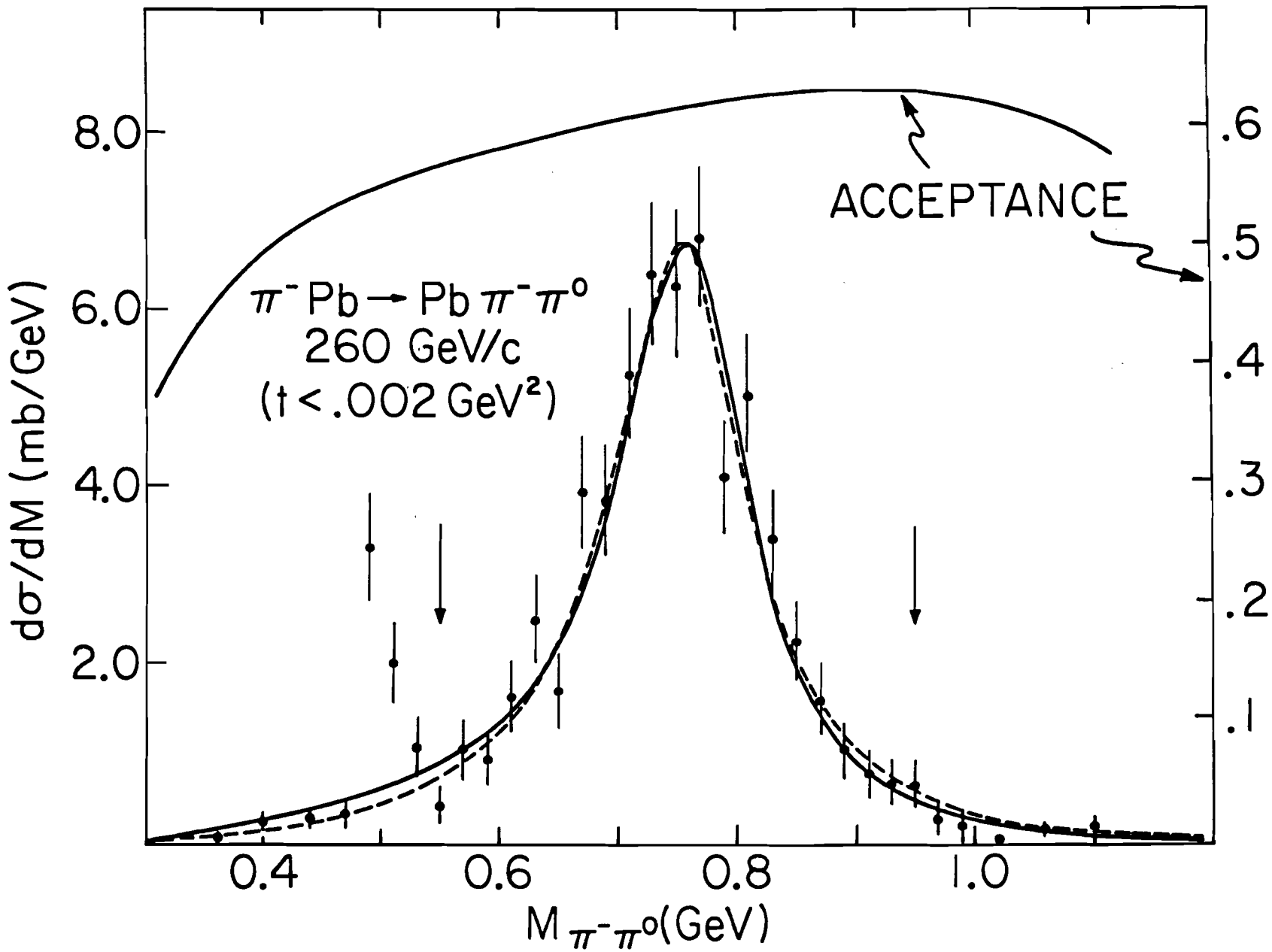
ACCEPTANCE
$\pi^- Pb \rightarrow Pb\, \pi^- \pi^0$
260 GeV/c
($t < .002\ GeV^2$)
$d\sigma/dM$ (mb/GeV)
8.0
6.0
4.0
2.0
.6
.5
.4
.3
.2
.1
0.4
0.6
0.8
1.0
$M_{\pi^-\pi^0}$(GeV)

Figure 46

data points have been corrected for geometric acceptance of the spectrometer assuming a $\sin^2\theta \sin^2\phi$ form for $\rho^- \to \pi^- \pi^0$ decay. The acceptance as a function of mass is indicated by the solid curves above the spectra. The errors on the data points are statistical.

Integrating Equation (3) over t, and substituting Equation (4) for $\sigma_\gamma(M^2)$ yields

$$\frac{d\sigma_c}{dM^2} \propto P_{inc}^2 \, t_{max} Z^2 \frac{M^2}{(M^2 - M_\pi^2)^3} \left| T(\gamma\pi^- \to \pi^-\pi^0) \right|^2 \tilde{F}(M^2) \qquad (8)$$

where t_{max} is the maximum range of integration. $\hat{F}(M^2)$ is a slowly varying function which results from the integration of the electromagnetic form factor over t, and accounts for the mass-dependent absorption of the $\pi^-\pi^0$ system. It was calculated using the optical model described in the following section. The value t_{max}=0.002 GeV^2 was chosen in order to emphasize the Coulomb contribution to ρ^- production.

We have assumed that the T-matrix has the form of a p-wave Breit-Wigner resonance:[47, 48]

$$\left| T(\gamma\pi^- \to \pi^-\pi^0) \right|^2 = \frac{M_0^2 \Gamma_{\gamma\pi}(M^2) \Gamma_{\pi\pi}(M^2)}{(M^2 - M_0^2)^2 + M_0^2 \Gamma_{\pi\pi}^2(M^2)} , \qquad (9)$$

where $\Gamma_{\pi\pi}$ and $\Gamma_{\gamma\pi}$ are the mass-dependent decay widths, and M_0 is the mass at resonance.

We have used several different phenomenological forms for the partial widths. Those which yielded the best fits to our data are:[47,48]

$$\Gamma_{\pi\pi} = \Gamma_0 \left(\frac{q}{q_0}\right)^3 \frac{2q_0^2}{q_0^2+q^2}$$

$$\Gamma_{\gamma\pi} = \Gamma_{\gamma 0} \left(\frac{k}{k_0}\right)^3 \frac{2k_0^2}{k_0^2+k^2} \quad ; \quad \Gamma_{\gamma 0}\left(\frac{k}{k_0}\right)^3 \frac{M}{M_0} \tag{10}$$

In these expressions q, and k are the momenta in the rest frame of the $\pi\pi$, and $\gamma\pi$ system, respectively. Values at resonance are subscripted with a zero.

In order to obtain better statistics for a fit of Equation (8) to the $\pi^-\pi^0$ mass, we combined data from both energies. According to Equation (8), there should be very little energy dependence in the shape of the mass spectrum. The two sets of data were therefore first corrected separately for geometric acceptance, and then combined for the fit. The fits were performed using the data between the arrows indicated in Figs. 45 and 46. These are the same limits used to define the ρ^- signal for the rest of the analysis (see Section A). As can be seen from the plots, the main differences in the fits to the forms given in Equation (10) occur in the tails of the distributions, where statistics are poor. The solid curves, corresponding to $\Gamma_{\gamma\pi} = \Gamma_{\gamma 0}(k/k_0)^3\,(2k_0^2)/(k_0^2+k^2)$, for example, give a χ^2 of 16

for 18 degrees of freedom. The resulting parameters for the ρ^-, M_ρ=772±3 MeV and Γ_ρ=139±6 MeV, are in reasonable agreement with the accepted values.[36]

The correction for events outside of the indicated limits on $M_{\pi^-\pi^0}$ was estimated from the acceptance-corrected mass spectra to be 1.10±.05. This is consistent with the values obtained using the fitted shapes given by Equation (10). The relatively large uncertainty is due to the fact that the shape of the ρ^- spectrum is not well known away from resonance.[47]

An additional correction determined by the shape of the ρ^- mass spectrum is needed in calculating the radiative width $\Gamma(\rho^- \to \pi^- \gamma)$. This is because equation (5) of Chapter I (see also Equation (11) in the following section) was obtained assuming a narrow-width resonance that can be approximated by a δ-function in the mass. The line shape of the ρ^- meson does not satisfy this condition. We therefore corrected the value of $\Gamma_{\gamma\rho}$ for the assumed narrow-width approximation by inserting into Equation (3) the parameterizations for the ρ-line shape given by Equations (9) and (10), and integrating numerically over the mass range of the ρ (0.55 GeV $< M_{\pi^-\pi^0} <$ 0.95 GeV). The resultant, essentially, energy independent correction factor is 1.14±0.02.[49]

E. Fits to the t-Distributions

The t-distributions for ρ-production from various nuclear targets are shown in Figs. 47-49. The restrictions on single-photon energy, two-photon mass, and total $\pi^-\pi^0$ energy applied to these data were the same as for the associated $K^- \rightarrow \pi^-\pi^0$ decays (see Chapter III.D) In addition, as indicated in Section A, to supress background from K-decays it was required that $0.55\ \text{GeV} < M_{\pi^-\pi^0} < 0.95\ \text{GeV}$. These data exhibit the qualitative features expected for electromagnetic production of the ρ. The sharp forward peak, increasing roughly as Z^2 for different targets, is characteristic of Coulomb production. The long tail at larger values of t indicates the presence of strong coherent production of the ρ.

The dashed lines are fits of the data to Equation (7). The fitting formalism which we applied to our data was developed previously and has been applied in several other experiments.[50] We therefore give only a brief outline of the procedure.

Assuming a narrow width approximation for the ρ-line shape, the cross section given by Equation (7) can be written in the form:

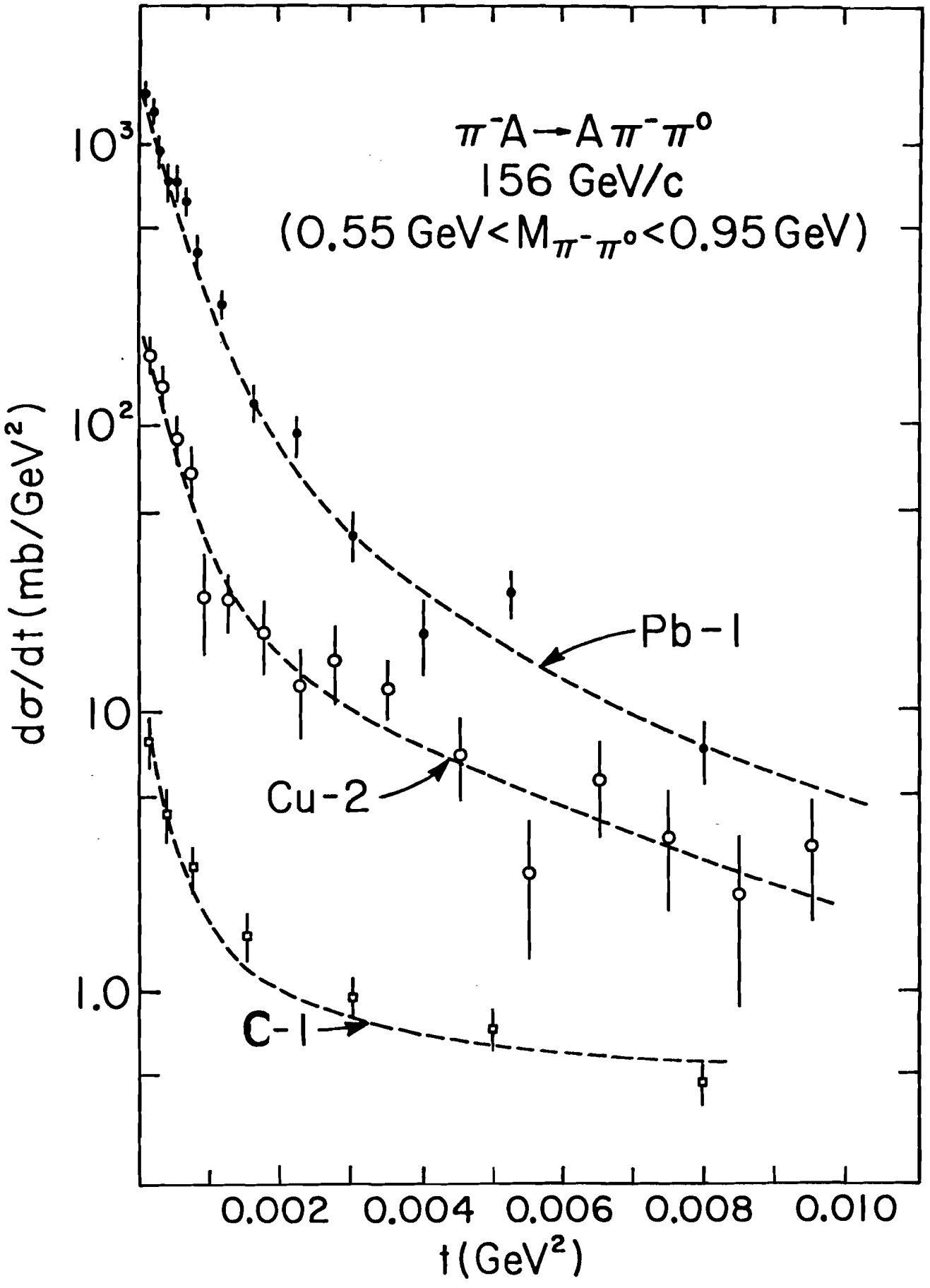
$\pi^- A \rightarrow A \pi^- \pi^0$
156 GeV/c
(0.55 GeV < $M_{\pi^-\pi^0}$ < 0.95 GeV)
Pb-1
Cu-2
C-1
10^3
10^2
10
1.0
$d\sigma/dt$ (mb/GeV^2)
0.002
0.004
0.006
0.008
0.010
t (GeV^2)

Figure 47

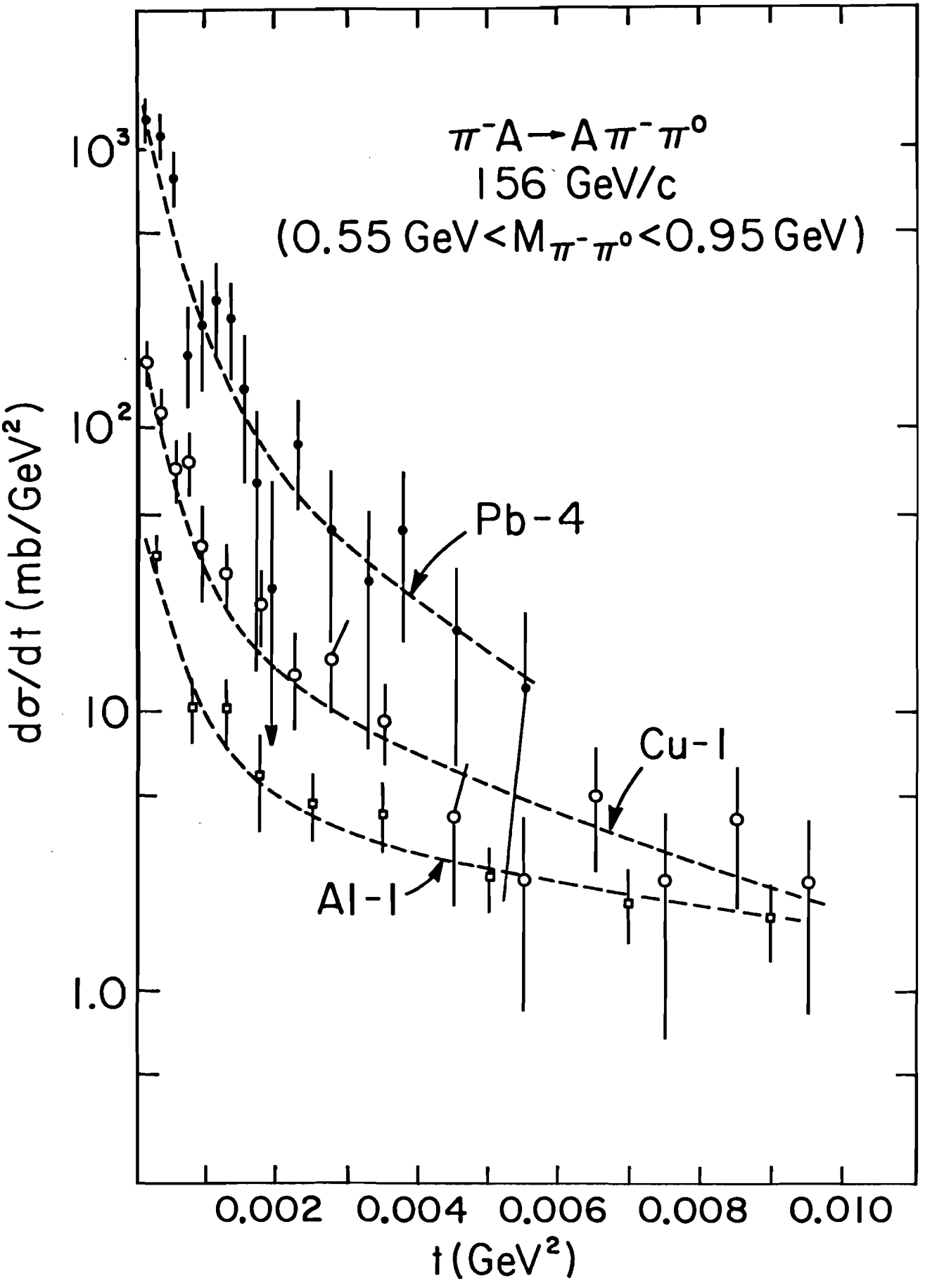
$\pi^- A \rightarrow A \pi^- \pi^0$
156 GeV/c
(0.55 GeV<$M_{\pi^-\pi^0}$<0.95 GeV)
Pb-4
Cu-1
Al-1
10^3
10^2
10
1.0
$d\sigma/dt$ (mb/GeV^2)
0.002
0.004
0.006
0.008
0.010
t(GeV^2)

Figure 48

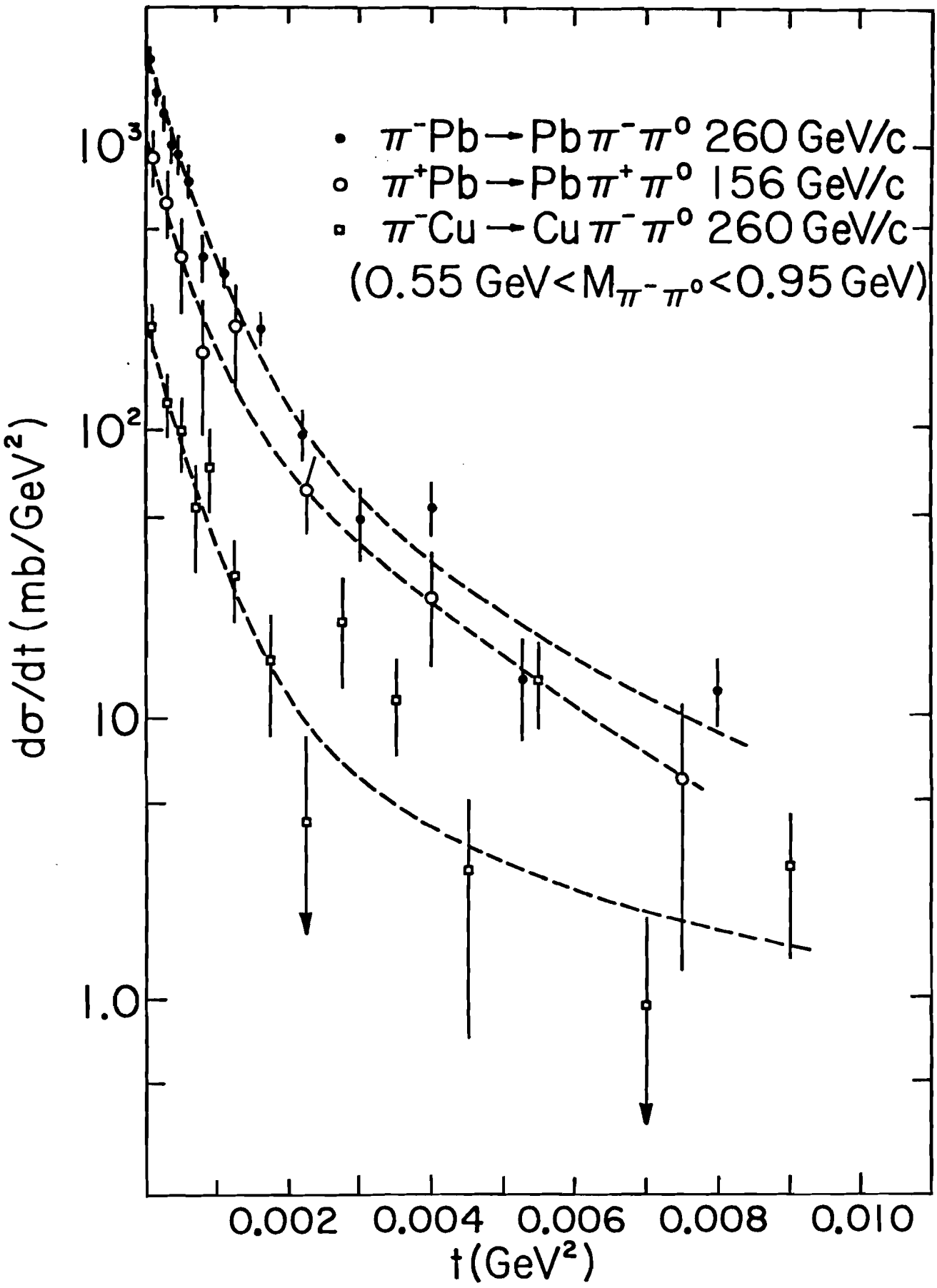
• $\pi^-Pb \rightarrow Pb\pi^-\pi^0$ 260 GeV/c
○ $\pi^+Pb \rightarrow Pb\pi^+\pi^0$ 156 GeV/c
▫ $\pi^-Cu \rightarrow Cu\pi^-\pi^0$ 260 GeV/c
(0.55 GeV < $M_{\pi^-\pi^0}$ < 0.95 GeV)
10^3
10^2
10
1.0
$d\sigma/dt$ (mb/GeV^2)
0.002
0.004
0.006
0.008
0.010
t(GeV^2)

Figure 49

$$\frac{d\sigma}{dt} = \Gamma(\rho^- \to \pi^-\gamma)|f_c(t)|^2 + C_s|f_s(t)|^2$$

$$+ 2\sqrt{\Gamma(\rho^- \to \pi^-\gamma)C_s}\Big[\Big\{Re[f_c(t)]Re[f_s(t)] + Im[f_c(t)]Im[f_s(t)]\Big\}\cos\phi$$

$$+ \Big\{Im[f_c(t)]Re[f_s(t)] - Re[f_c(t)]Im[f_s(t)]\Big\}\sin\phi\Big], \qquad (11)$$

such that $F_c(t) = [\Gamma(\rho^- \to \pi^-\gamma)]^{1/2} f_c(t)$ and $F_s(t) = C_s^{1/2} f_s(t)$.

The terms $f_s(t)$ and $f_c(t)$ account not only for the nuclear shape but also for absorption of the incoming and outgoing states within the nucleus. The explicit forms which we used for these terms are:[50]

$$f_s(t) = A\int d^3r \; \exp\left[i\vec{q}\cdot\vec{r} + i\chi_c(b)\right] \exp\left[-\sigma' T(b)/2\right] \sqrt{2}\,\frac{(\vec{\varepsilon}\times\vec{k})}{q_T}\cdot\vec{\nabla}_b g(b,z),$$

$$f_c(t) = \frac{z}{t}\left[2\frac{4\pi e^2}{\hbar c}\left(\frac{m_\rho}{m_\rho^2 - m_\pi^2}\right)^3\right]^{1/2} \sqrt{2}\,(\vec{\varepsilon}\times\vec{k})\cdot\vec{F}_{EM}(t),$$

where

$$\vec{F}_{EM}(t) = \frac{1}{4\pi i}\int d^3r \; \exp\left[i\vec{q}\cdot\vec{r} + i\chi_c(b)\right] \exp\left[-\sigma' T(b)/2\right] \vec{E}(\vec{r}).$$

$\vec{E}(\vec{r})$ is the electric field of the nucleus, and $\sigma' = (1 - i\kappa)\sigma$, where σ is the total π-nucleon cross section, and κ is the ratio of the real to imaginary part of the forward scattering amplitude for π-nucleon collisions (we have

assumed the same values for σ and κ for the outgoing ρ as for the incoming π).[51] The nuclear thickness as a function of impact parameter (b) is given by

$$T(b) = A\int_{-\infty}^{\infty} dz\, g(b,z)$$

where g is the density distribution of nuclear matter. The Coulomb phase due to the nuclear charge distribution is given by

$$\chi_c(b) = -\frac{Ze^2}{\hbar c}\int_{-\infty}^{\infty} dz\, \psi(\sqrt{b^2+z^2}) \quad ,$$

where

$$\psi(\vec{r}) = \int d^3r' \frac{g(\vec{r}')}{|\vec{r}-\vec{r}'|}$$

is the Coulomb potential of the nucleus.

Because Coulomb production occurs predominately outside of the nucleus, it is not expected that the form used for the nuclear density function will seriously affect the calculations. Hence, for computing the $f_c(t)$ term, we assumed a uniform nucleus of radius $R = \left[c^2 + (7/3)(\pi a)^2\right]^{1/2}$, where $c=1.12A^{1/3}$ fm, and $a=0.545$ fm.[52] These terms correspond to parameters for an average radius given by the Woods-Saxon distribution,

$$g(r) = \frac{g_0}{1+\exp\left(\frac{r-c}{a}\right)} \quad .$$

Because hadronic production is concentrated at the surface

of the nucleus, the $f_S(t)$ term is more sensitive to the distribution of nuclear matter, and we therefore employed the Woods-Saxon paramaterization in calculating $f_S(t)$.

The t-resolution of the spectrometer had to be taken into account in the fit of Equation (11) to the data. The observed cross section, $d\sigma/dt$, is a convolution of the true production cross section, $d\sigma/d\tilde{t}$, with a resolution function, $R(t,\tilde{t})$:

$$\frac{d\sigma}{dt} = \int d\tilde{t}\, R(t,\tilde{t})\, \frac{d\sigma}{d\tilde{t}} \; .$$

We have assumed that the resolution function can be parameterized as a two dimensional Gaussian distribution in transverse momentum; that is,

$$R(t,\tilde{t}) = \frac{1}{2\pi\Delta^2} \exp\left[-\frac{|\tilde{\vec{q}}_T - \vec{q}_T|^2}{2\Delta^2} \right] ,$$

where $\tilde{\vec{q}}_T$ and $\vec{q}_T$ are the exact and the resolution-smeared two-dimensional transverse momenta, respectively, and Δ is the standard deviation of the Gaussian distribution. The $K^- \rightarrow \pi^-\pi^0$ data, for which $\tilde{\vec{q}}_T = 0$, were consistent with this choice for the resolution function (see Chapter III.D). The value of Δ used in the analysis of any particular set of ρ data was determined from the t-distribution for the corresponding $K^- \rightarrow \pi^-\pi^0$ data sample. For example, the data for the Pb-1 target at 156 GeV/c (see Fig. 24) indicate $\Delta \approx 12$ MeV/c.

Folding in the resolution, the t-dependent factors $f_c(t)$ and $f_s(t)$ were calculated and tabulated in t-intervals for comparison with the data. The three parameters, $\Gamma(\rho^- \to \pi^- \gamma)$, C_s, and ϕ, were then varied to achieve the best fit of Equation (11) to the data.

Table VI summarizes the results of fits to the data for the regions of t indicated in column 3. The errors on the parameters are statistical. To check the stability of the solutions, we varied the ranges of t used in the fits; also, we performed fits including a background term of the form Dexp(-Et), where D and E are constants. In all cases the fits yielded acceptable χ^2 values, and fluctuations in the values of the parameters for any target were within statistical error. Fits were also performed using different values for the resolution (Δ). It was found that a 20% change in Δ produced a 15% change in the fitted value for $\Gamma(\rho^- \to \pi^- \gamma)$. In the global fits (for $t < .01$ GeV^2) we assumed that C_s and ϕ were independent of target material. In the values quoted for $\Gamma(\rho^- \to \pi^- \gamma)$, we have corrected for the finite width of the ρ-line shape in the manner described in the previous section.

Although the value obtained for $\Gamma(\rho^+ \to \pi^+ \gamma)$ is ~ 2.5 standard deviations below the value for $\Gamma(\rho^- \to \pi^- \gamma)$, owing to the limited statistics and the poorly determined resolution parameters for this data, we cannot attribute

Table VI

Results of Parameterization of Data (all quoted errors are statistical)

	Target	t-range (GeV^2)	$\Gamma(p^- \to \pi^- \gamma)$ (KeV)	$C_S \left[\frac{mb}{GeV^4}\right]$	ϕ	χ^2/d.o.f.
-156 GeV/c	C-1	<0.035	58.3 ± 5.5	0.67 ± 0.06	- 4 ± 32	11.0/8
	Al-1	<0.04	67.4 ± 8.1	0.86 ± 0.22	-16 ± 97	5.22/11
	Cu-1	<0.01	54.3 ± 5.6	0.55 ± 0.26	-28 ± 49	12.2/13
	Cu-2	<0.01	58.9 ± 5.4	0.57 ± 0.71	-32 ± 137	11.4/13
	Pb-1	<0.015	72.2 ± 3.7	0.74 ± 0.23	7 ± 17	16.9/12
	Pb-4	<0.006	61.2 ± 8.2	0.67 ± 0.65	7 ± 49	13.9/13
	Global Fit	<0.01	62.0 ± 2.5	0.59 ± 0.07	16 ± 22	79.5/75
-260 GeV/c	Cu-2	<0.02	63.2 ± 7.6	0.36 ± 0.25	87 ± 35	17.0/13
	Pb-1	<0.02	76.0 ± 4.6	0.79 ± 0.30	56 ± 29	13.0/13
	Global Fit	<0.01	76.0 ± 3.7	0.52 ± 0.25	82 ± 21	40/28
+156 GeV/c	Pb-1	<0.02	43.8 ± 9.3	0.60 ± 0.45	-36 ± 87	1.74/7

Table VII

Integrated Cross Sections for Coherent ρ Production on Nuclei

	Target	$\int_0^{.005} dt\|F_C\|^2$ (μb)	$\int_0^{.005} dt\|F_S\|^2$ (μb)	$2\mathrm{Re}\int_0^{.005} dt\, F_C^* F_S e^{i\phi}$ (μb)
-156 GeV/c	C-1	5.5 ± 0.5	0.9 ± 0.08	2.3 ± 1.3
	Al-1	28.2 ± 3.4	3.8 ± 1.0	9 ± 15
	Cu-1	107 ± 11	6.5 ± 3.1	24 ± 22
	Cu-2	116 ± 11	7 ± 7	24 ± 58
	Pb-1	979 ± 50	29.9 ± 9.3	8.9 ± 3.9
	Pb-4	833 ± 11	28 ± 26	10 ± 9
-260 GeV/c	Cu-2	147 ± 18	4.5 ± 3.1	-3.1 ± 2.9
	Pb-1	1254 ± 76	30.8 ±11.7	26.6 ±15.9
+156 GeV/c	Pb-1	595 ± 126	26 ± 20	65 ± 99

much significance to this result. Further data on the reaction $\pi^+A \rightarrow A\pi^+\pi^0$ has recently been collected by our group, and will be analyzed in order to establish $\Gamma(\rho^+ \rightarrow \pi^+\gamma)$.

In Table VII, we tabulate the integrated values of $|F_c|^2$, $|F_s|^2$ and of the interference terms, for $t < 0.005$ GeV^2. These values were calculated from integrations over the fitted curves.

F. Conclusions

Based on a weighted average of the fitted values for $\Gamma(\rho^- \rightarrow \pi^-\gamma)$ for the different targets at the two energies, and on the checks of our normalization procedure, we quote a new value, $\Gamma(\rho^- \rightarrow \pi^-\gamma) = 67 \pm 7$ KeV, for the radiative decay width of the ρ^-.[53] The major sources of the uncertainties are the normalization to K-decays ($\pm 5\%$), the correction for the ρ-mass cut ($\pm 5\%$), and the parameterization of the resolution function ($\pm 5\%$). The values for C_s and ϕ are not well determined, but are consistent with extrapolations from measurements made at lower energies.[54]

Our result for $\Gamma(\rho^- \rightarrow \pi^-\gamma)$ is substantially higher than that of the previous measurement of $\Gamma(\rho^- \rightarrow \pi^-\gamma) = 35 \pm 10$ KeV.[3,4] There is less than a 1% likelihood that both experiments are correct within their quoted

errors.

At our energies the ratio of Coulomb to hadron exchange is greatly enhanced relative to that of the previous experiment at 23 GeV/c. This enabled us to obtain stable and consistent fits for our individual target elements and at both incident energies. In contrast, the previous experiment was only able to extract a unique partial width after carrying out a global fit to all their elements assuming a constant value of C_S. Without this assumption, only the limits $30\pm10 < \Gamma(\rho^- \to \pi^- \gamma) < 80\pm10$ KeV could be reported,[3,4] a result which is in complete agreement with the value we have obtained. In fact, it has recently been suggested that a variation of C_S with A could result, particularly at lower beam energies, if A_2-exchange contributes to Reaction (1).

If our measurement of $\Gamma(\rho^- \to \pi^- \gamma)$ is preferred over the previous value, it is interesting to note that it is thereby possible to obtain a far more self-consistent overall fit to vector meson radiative widths.[56]

REFERENCES

1. R. P. Feynman, Photon-Hadron Interactions, (W. A. Benjamin, Inc., Reading, Mass. 1972).

2. For a recent review of the experimental situation see E. H. Thorndike, V International Conference on Experimental Meson Spectroscopy, 1977 E. Von Goeler and R. Weinstein Eds., p.345. For a comparison of theory and experiment see R. L. Thews, Phys. Rev. D14, 3021 (1976); P. J. O'Donnel, Can. J. Phys. 55, 1301 (1977); A. N. Kamal, Phys. Rev. D18, 3512 (1978); B. J. Edwards and A. N. Kamel, SLAC-PUB-2303 (1979).

3. B. Gobbi et al, Phys. Rev. Lett. 33, 1450 (1974); B. Gobbi et al, Phys. Rev. Lett. 37, 1439 (1976).

4. A thorough description of the first measurement of $\Gamma(\rho^- \to \pi^- \gamma)$ can be found in L. Strawczynski, PhD Thesis, University of Rochester report UR-475 (1974). This reference also presents a very useful discussion of the theory relating to this measurement.

5. See, for example, A. W. Hendry and D. B. Lichtenberg, Rep. Prog. Phys., 41, 1707 (1978).

6. M. Gell-Mann, Phys. Lett. 8, 214 (1964).

7. G. Zweig, CERN Rep. 8419/TH (1964); G. Zweig, Symmetries in Elementary Particle Physics, ed A. Zichichi, (Academic Press, New York) p.192 (1965).

8. J. Aubert et al, Phys. Rev. Lett. 33, 1404 (1974); J. Augustin et al, Phys. Rev. Lett. 33, 1406 (1974).

9. C. Becchi and G. Morpurgo, Phys Rev. 140B, 687 (1965); Y. Anisovitch et al, Phys. Lett. 16, 194 (1965); W. Thirring, Phys Lett. 16, 335 (1965); L. Soloviev, Phys. Lett. 16, 345 (1965). Earlier theoretical investigations of these decays in terms of SU(3) symmetry arguments were made by S. Okubo, Phys Lett. 4, 14 (1963); S. L. Glashow, Phys. Rev. Lett. 11, 48 (1963); K. Tanaka, Phys. Rev. 133, B1509 (1964). Applications of the quark model to hadron decay processes are summarized by R. VanRoyen and V. F. Weisskopf, Nuovo Cimento A 50, 617 (1967).

10. See, for example, C. Becchi and G. Morpurgo in Reference 9.

11. There is some disagreement regarding the validity of the long-wavelength approximation and the form used for the phase space factor. For a discussion of these questions, see P. J. O'Donnel in Reference 2.

12. See, for example, P. A. M. Dirac, The Principles of Quantum Mechanics, p. 178 (Oxford University Press, London) Fourth Edition (1958).

13. The mixing angle obtained from the quadratic mass formula differs only slightly from the "ideal" angle. See, for example, R. F. Dashen and D. Sharp, Phys. Rev. 133B, 1585 (1964).

14. J. Keyne et al, Phys. Rev. D14, (1976).

15. Coherent processes are discussed in detail by H. H. Bingham, in Proc. Topical Seminar on Interactions of Elementary Particles with Nuclei, Trieste, 1970 p. 37 (INFN, Trieste, 1971). See also T. Ferbel, Lecture presented at the First Workshop on Ultra-Relativistic Nuclear Collisions, LBL (1979), University of Rochester Report UR-704.

16. H. Primakoff, Phys. Rev. 81, 899 (1951).

17. Early measurements of the π^0 lifetime are described by G. Belletini et al, Nuovo Cimento 40A, 1139 (1965); G. Belletini et al, Nuovo Cimento 66A, 243 (1970); V. I. Kryskin et al, Soviet Physics JETP, 30, 1037 (1970). The most recent measurement was made by A. Browman et al, Phys. Rev. Lett. 33, 1400 (1974).

18. A. Halprin, C. M. Andersen, and H. Primakoff, Phys. Rev. 152, 1295 (1966); Y. Nagashima and J. Rosen, University of Rochester Report No. UR-875-295, 1969 (unpublished); N. Jurisic and L. Stodolsky, Phys. Rev. D3, 724 (1971); M. Gourdin, Nucl. Phys. B32, 415 (1971); G. Berlad et al, Ann. of Phys. 75, 461 (1973).

19. See, for example, G. Berlad et al in Reference 18, or L. Strawczynski in Reference 4.

20. D. R. O. Morrison, Phys. Lett. 22, 528 (1966); C. B. Chiu, Annual Review of Nuclear Science 22, p. 255 (1972), E. Segre, ed. (Annual Reviews Inc, Palo Alto, California).

21. L. Stodolsky, Phys. Rev. 144, 1145 (1966).

22. A concise source of information on the M-1 beamline is provided in the M-1 Users' Guide, S. Ecklund, Fermilab Report TM-743.2833, May 1977.

23. TRANSPORT Users' Manual, K. L. Brown et al., Fermilab Report NAL-91, March 1974.

24. These counters were designed by T.F. Kycia. A description of their operation may be found in an appendix of Reference 22.

25. This counter, designed by S. M. Pruss, is similar to a prototype counter described in D. D. Yovanovitch et al, ANL Report ANL/HEP-7104 (1972).

26. This circuit, designed by B. Wormington, is described in T. Joyce, Ph. D. Thesis, University of Minnesota (unpublished).

27. For a more detailed description of the operation of these units refer to the LRS Model 2770A Technical Information Manual, Lecroy Research Corp., Spring Valley, New York.

28. For a description of this pulser circuit, see T. Joyce in Reference 26.

29. Many papers have been published on the development of liquid argon calorimeters. The following are particularly applicable to the type of detector which we have built: W. J. Willis and V. Radeka, Nucl. Inst. and Meth. 120, 221 (1974). G. Knies and D. Neuffer, Nucl. Inst. and Meth. 120, 1 (1974). D. Hitlin et al., SLAC-PUB-1761 (May 1976).

30. J. Engler et al., Nucl. Inst. and Meth. 120, 157 (1974).

31. W. Hofmann et al., Nucl. Inst. and Meth. 135, 151 (1976).

32. T. F. Droege, F Lobkowicz, and Y. Fukushima, Fermilab Report TM-746 2500.000, (October 1977).

33. C. R. Kerns, Fermilab Report TM-819 2510.000, (October 1978).

34. A. E. Brenner, T. F. Droege, and R. G. Martin, Fermilab Report TM-537 2340.000 (December 1974).

35. For a more complete description of calibration and alignment of the drift chambers, see D. Berg, Ph. D. Thesis, University of Rochester, 1980 (unpublished).

36. Particle Data Tables, Phys. Letts. 75B, No. 1 (1978).

37. A. S. Carroll et al, Phys. Rev. Lett. 33, 932 (1974).

38. Yung-Su Tsai, Rev. of Mod. Phys. 46, 815 (1974).

39. J. C. Allaby et al, Sov. Journal of Nucl. Phys. 12, 295 (1971).

40. G. Fischer et al, Nucl. Phys. B16, 93 (1970).

41. P. Feller et al, Nucl. Phys. B104, 219 (1976).

42. H. Scott, Ph. D. Thesis, University of Rochester Report UR-529 (1975) (unpublished).

43. J. Biel, Ph. D. Thesis, University of Rochester Report UR-614; J. Biel et al, Phys. Rev. D18, 3079 (1978).

44. J. Biel et al, Phys. Rev. D20, 33 (1979).

45. L. Stodolsky and J. J. Sakurai, Phys. Rev. Letts. 11, 90 (1963).

46. R. T. Deck, Phys. Rev. Lett. 13, 169 (1964).

47. M. Roos, Nucl. Phys. B2, 615 (1967); J. Pisut and M. Roos, Nucl. Phys. B6, 325 (1968); M. Roos and J. Pisut, Nucl. Phys. B10, 563 (1969).

48. J. D. Jackson, Nuovo Cimento 34, 1644 (1964).

49. For a derivation of the finite-width correction, see T. Ohshima, "Coulomb Cross Section and Resonance Width", University of Rochester Internal Report.

50. K. S. Kölbig and B. Margolis, Nucl. Phys. B6, 85 (1968); G. Fäldt et al, Nucl. Phys. B 41, 125 (1972); G. Fäldt, Nucl. Phys. B43, 591 (1972); C. Bemporad et al, Nucl. Phys. B51, 1 (1973). See also B. Gobbi et al in Reference 3, and L. Strawczynski in Reference 4.

51. We have used the values, α=0.015 at 156 GeV/c and α=0.10 at 260 GeV/c, given by J. Burq et al, CERN EP Internal Report 78-07 (1978). The π-nucleon cross section, σ=24.5 mb, was obtained from the Particle Data Tables (Reference 36).

52. B. Hahn, D. G. Ravenhall and R. Hofstadter, Phys. Rev. 101, 1131 (1956).

53. D. Berg et al, Phys. Rev. Lett. 44, 706 (1980).

54. As mentioned in Chapter I, C_s is expected to scale as $1/p_{inc}$. D. J. Crennel et al, Phys. Rev. Lett. 27, 1674 (1971), report C_s=13.7±2.2 mb/GeV^4 at 6 GeV/c; J. Bartsch et al, Nucl. Phys. B46, 46 (1972), report C_s=6.9±1.5 mb/GeV^4 at 16 GeV/c; B. Gobbi et al, (Reference 3) report C_s=4.0±1.0 mb/GeV^4 at 22.7 GeV/c.

55. A. N. Kamal and G. L. Kane, Phys Rev. Lett. 43, 551 (1979).

56. T. Ohshima, University of Rochester Report, UR-733 (1980); B. J. Edwards and A. N. Kamal, in Reference 2; D. A. Geffen and Warren Wilson, Phys. Rev. Lett. 44, 370 (1980).

57. Much work has been done on the developement on drift chambers. General properties of these detectors are described in, for example, A. Breskin et al, Nucl. Inst. and Meth. 119, 9 (1974).

58. This gas mixture was recommended to us by M. Atac of Fermilab.

59. B. Jean-Marie, V. Lepeltier, and D. L'hote, Nucl. Inst. and Meth. 159, 213 (1979).

APPENDIX A

CONSTRUCTION AND OPERATION OF DRIFT CHAMBERS

In this appendix we describe the methods employed in constructing and operating the drift chambers used in this experiment. The system was composed of a total of 24 chambers, all constructed in a similar manner.

Figure 50.a illustrates the assembly of a pair of drift chambers from the D1 or D2 units (see Fig. 4). Each high-voltage or sense plane was supported on a frame that was machined from a single piece of aluminum. G-10 circuit-board material was fixed to these frames. Stainless steel pins which fitted through accurately placed holes in the aluminum frames were used to align the planes with respect to each other. Two frames at a time were pinned through these holes to a rotating support structure over which wires were wound mechanically at precisely spaced intervals. When the winding was completed, the whole frame was moved relative to the wires until certain wires lined up with a set of accurately placed scribe marks. The wires were then glued to the planes using APCO R313 epoxy and,

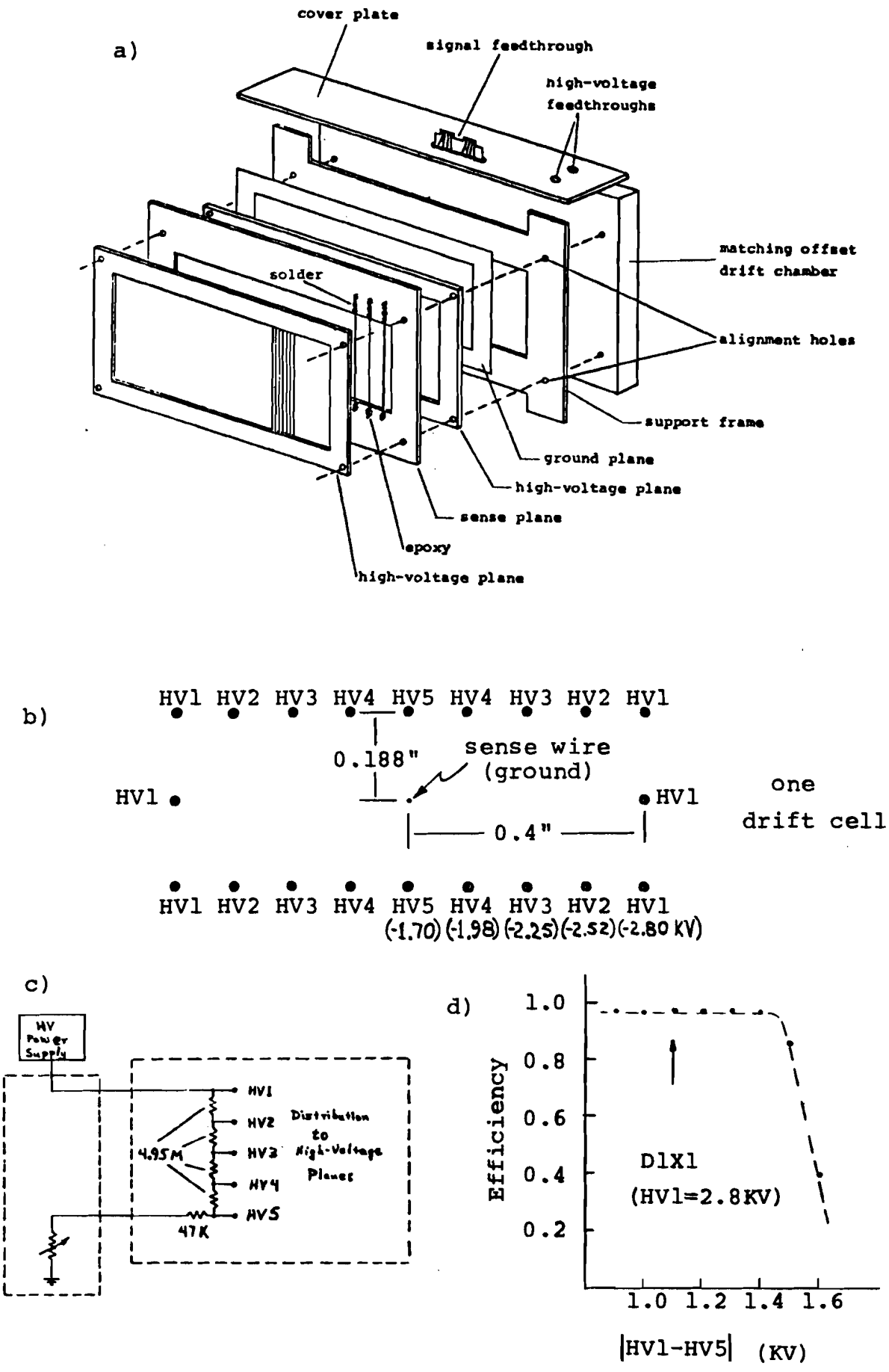
a)
cover plate
signal feedthrough
high-voltage feedthroughs
matching offset drift chamber
solder
alignment holes
support frame
ground plane
high-voltage plane
sense plane
epoxy
high-voltage plane
b)
HV1 HV2 HV3 HV4 HV5 HV4 HV3 HV2 HV1
0.188"
sense wire (ground)
HV1
HV1
0.4"
one drift cell
HV1 HV2 HV3 HV4 HV5 HV4 HV3 HV2 HV1
(-1.70) (-1.98) (-2.25) (-2.52) (-2.80 KV)
c)
HV Power Supply
HV1
HV2
HV3
HV4
HV5
4.95M
47K
Distribution to High-Voltage Planes
d)
Efficiency
1.0
0.8
0.6
0.4
0.2
D1X1
(HV1=2.8KV)
1.0 1.2 1.4 1.6
|HV1-HV5| (KV)

Figure 50

after this epoxy dried, the wires were soldered to copper pads on the G-10 circuit boards. A survey made later using an optical table showed that the sense wires were positioned relative to each other with an accuracy of about ±0.0005 in.

The sense wires were composed of gold-plated tungsten, 0.0008 in. diameter, and the high-voltage wires of a beryllium-copper alloy, 0.004 in. diameter. The wires were tensioned by means of a pulley and weight system as they were wound onto the support structure, and the frames were pre-stressed before winding to compensate for the force from the wires. After the wires were glued and soldered to the frames, and the pre-stressing removed, sample planes were checked for proper wire tension. The tension on the sense wires was found to be ~45 g and on the high voltage wires ~150 g.

The dimensions of a single drift cell are shown in Figure 50.b; typical operating voltages are also indicated next to the field-shaping wires in this sketch.[57] All cells in the system had the same dimensions, but those in D3 and D4 had half as many field-shaping wires on the high-voltage planes (the wires labeled HV2 and HV4 were not present).

The high-voltage supply circuit for one drift chamber is shown in Fig. 50.c. Both planes in a doublet were driven by the same power supply; consequently the voltage labeled HV1 was required to be the same for both planes. The lower

voltage, labeled HV5, could be varied for each plane by means of a resistor divider network.

The high-voltage cable supplying the HV5 voltage had a sizeable capacitance, and the stored energy, when rapidly released in the form of a spark, could have broken sense wires. The 47 KΩ resistor in the divider chain greatly increased the RC time constant and thereby served to protect against sparking to the sense wires in the event of an electrostatic breakdown.

A ground plane, made of 0.002 in. diameter beryllium-copper wires that were spaced 0.2 in. apart, was placed between each chamber in the D1 and D2 units. These planes served to isolate the chambers electrostatically and to provide collection points for ionization produced between the chambers. Ground planes were not used in D3 and D4 because all the chambers in these systems were totally independent of each other.

The doublet system illustrated in Fig. 50.a was attached to a cover plate which contained feedthroughs for the signal and high-voltage cables. Any doublet in D1 or D2 could be removed from the gas container without disturbing the other two doublets. Doublets were aligned relative to each other within the box by means of stainless steel pins located at the bottom of the box. To complete the electrostatic shielding of the units, thin aluminum-coated

mylar windows were placed on the sides of the box intercepted by the beam.

The assembled boxes were placed on tables that were leveled and centered relative to the beamline. Pins on the bottom of the boxes matched holes in the table for purposes of precise repositioning. The chambers did not have to be moved during the course of the experiment.

Each of the D3 and D4 chambers was enclosed with aluminum-coated mylar windows. Doublets were aligned with respect to each other through pins that rested in common V-blocks which were attached to support stands.

Most of the chambers were tested with an electron source before they were placed in the beamline. In addition to checking the efficiency and stability of the chambers, we also studied the properties of different gas mixtures. We decided to employ an equal mixture of argon and ethane gas because of its easy availability, high efficiency, and uniform drift velocity.[58] The gas in all the chambers was maintained at a pressure slightly above one atmosphere by means of oil bubblers at the exhaust ends. The entire system had a volume of about fifty cubic feet, and gas flowed through the chambers at a rate of about two cubic feet per hour.

A typical efficiency plateau for detecting beam particles is shown in Fig. 50.d. For these data, the HV1 voltage was held fixed at -2.8 KV, while the HV5 setting was varied. The drift velocity for our argon-ethane gas mixture saturates at field gradients of about 0.8 KV/cm,[59] which is well below where these chambers were operated.